Gesellschaft für Anlagen- und Reaktorsicherheit (GRS) mbH

Thermo-Hydro-Mechanical and Geochemical Behaviour of the Callovo-Oxfordian Argillite and the Opalinus Clay

Final Report

GRS - 202

Gesellschaft für Anlagen- und Reaktorsicherheit (GRS) mbH

Thermo-Hydro-Mechanical and Geochemical Behaviour of the Callovo-Oxfordian Argillite and the Opalinus Clay

Final Report

Chung-Liang Zhang
Tilmann Rothfuchs
Helge Moog
Jürgen Dittrich
Jürgen Müller

June 2004

Remark:

This report was prepared under contract No. 02 E 9541 with the Bundesministerium für Wirtschaft und Arbeit (BMWA).

The work was conducted by the Gesellschaft für Anlagen- und Reaktorsicherheit (GRS) mbH.

The authors are responsible for the content of this report.

GRS - 202
ISBN 3-931995-69-0

Deskriptoren:
Deponie, Endlagerung, Felsformation, Frankreich, Internationale Zusammenarbeit, Langzeitsicherheit, Labor, Modell, Nuklidtransport

Foreword

Since 2000, the Meuse/Haute-Marne Underground Research Laboratory (MHM-URL) is being built at Bure in eastern France to study the suitability of the Callovo-Oxfordian argillaceous formation to host a repository for high-level and long-lived radioactive waste. ANDRA envisages a research programme, in which a set of full-scale *in situ* experiments will be conducted in the underground laboratory.

GRS intends to participate in the Bure programme and to co-operate with ANDRA on basis of a co-operation agreement. GRS has proposed to contribute to ANDRA's research programme by participating in *in situ* experiments as well as by performing laboratory investigations and numerical modelling. In preparation of the Bure activities a pre-project was conducted by GRS under contract number 02E9541 with BMWA, between July 2001 and December 2003. The objectives of the pre-project were:

- Development and testing of laboratory experimental methods to investigate the coupled thermo-hydro-mechanical-chemical (THMC) behaviour of the argillite,
- To select and test a numerical code suited for the analysis of coupled THM processes in clays.

Laboratory experiments were carried out on samples of the Callovo-Oxfordian argillite at the MHM-URL Bure and the Opalinus clay at the Mont Terri URL. The objective was to study the long-term creep behaviour, swelling and shrinkage, coupled HM and THM behaviour, diffusion of radionuclides, and extraction of pore water.

A number of THM modelling exercises were performed by using the code CODE-BRIGHT, including scoping calculations of coupled THM phenomena observed in clays under laboratory and *in situ* conditions.

The most important results of laboratory investigations and numerical calculations achieved in the pre-project are summarized in this report.

Table of Contents

1 Introduction 1

1.1 Research Programme of the Bure Underground Laboratory 1

1.2 GRS Proposal for Contribution to the Bure Programme 2

1.3 Pre-Project for Participation in the Bure Programme 4

1.3.1 Objectives 4

1.3.2 Experimental Programme 4

1.3.3 Modelling Programme 5

2 Geotechnical Experiments 7

2.1 Sample Characterisation 7

2.1.1 Samples 7

2.1.2 Measurements of Petrophysical Properties 9

2.2 Long-Term Creep Experiments 14

2.2.1 Testing Method 14

2.2.2 Results 18

2.2.3 Conclusions and Remarks 24

2.3 Swelling Experiments 27

2.3.1 Theoretical Considerations 27

2.3.2 Swelling Pressure in Volume-Constraint Conditions 30

2.3.3 Uniaxial Swelling Pressure 32

2.3.4 Uniaxial Swelling, Shrinkage and Creep 35

2.4 Thermo-Hydro-Mechanical Experiments 37

2.4.1 Testing Devices 37

2.4.1.1 Oedometer 37

2.4.1.2 Triaxial Apparatus 39

2.4.2 Testing Procedure 41

2.4.3 Results of Hydro-Mechanical Tests 42

2.4.4 Results of Thermo-Hydro-Mechanical Tests 49

2.4.5 Discussions and Conclusions 55

3 Geochemical Experiments 57
3.1 Diffusion of Cs^+, I^-, and SeO_4^{2-} in the Callovo-Oxfordian Argillite 57
3.1.1 Introduction 57
3.1.2 Materials and Methods 58
3.1.3 Data Processing 60
3.1.4 Results 61
3.2 Leaching of the Callovo-Oxfordian Argillite 62
3.2.1 Introduction 62
3.2.2 Materials and Methods 63
3.2.3 Results 64

4 Numerical Modelling 69
4.1 Theoretical Framework 69
4.1.1 Balance Equations 69
4.1.2 Equilibrium Restrictions 71
4.1.3 Constitutive Equations 71
4.1.3.1 Thermal Equations 71
4.1.3.2 Hydraulic Equations 72
4.1.3.3 Mechanical Equations 74
4.2 Material Parameters 78
4.2.1 Thermal Parameters 79
4.2.2 Hydraulic Parameters 79
4.2.3 Mechanical Parameters 83
4.3 Modelling of Normal Laboratory Experiments 87
4.3.1 Swelling Behaviour of Bentonite 87
4.3.1.1 Swelling Pressure 88
4.3.1.2 Swelling Strain 90
4.3.2 Consolidation and Collapse of Bentonite 91
4.3.3 Resaturation of Bentonite 94
4.3.4 Desaturation of Opalinus Clay 96
4.3.5 Response of Bentonite to Heating 97
4.3.5.1 Response of Unsaturated Bentonite to Heating 98

4.3.5.2 Response of Saturated Bentonite to Heating 100
4.4 Predictions of Large-Scale Laboratory Experiments 103
4.4.1 Ventilation of a Borehole in Clay 103
4.4.2 Response of Rock-Buffer-System to Heating 108
4.5 Calculations of Perturbations induced by Drift Excavation and Ventilation *in situ* 118

5 Summary 129
5.1 Laboratory Experiments 129
5.2 Numerical Modelling 132
5.3 Future Investigations 133

6 Acknowledgements 135

7 References 137

8 List of Figures 143

9 List of Tables 149

1 Introduction

1.1 Research Programme of the Bure Underground Laboratory

Since 2000, the Meuse/Haute-Marne Underground Research Laboratory (MHM-URL) is being built at Bure in eastern France /AND 00/03a/b/ to study the suitability of the Callovo-Oxfordian argillaceous formation to host a repository for high-level and long-lived radioactive waste (HLW). Figure 1.1 shows the general view of the underground laboratory. The French Agence Nationale Pour la Gestion de Déchets Radioactifs (ANDRA) has envisaged a research programme, in which a set of full-scale *in situ* experiments (see Table 1.1) will be conducted in the underground laboratory. Details about the research programme are to be found in /AND 00/03a,b/, /SU 03/. The experiments were planned for the time until the end of 2005. In 2006, based on the results to be obtained from these experiments, ANDRA has to provide to the French government technical and scientific reports describing the furtherance state of phenomenological modelling and performance assessment of the Meuse/Haute-Marne site.

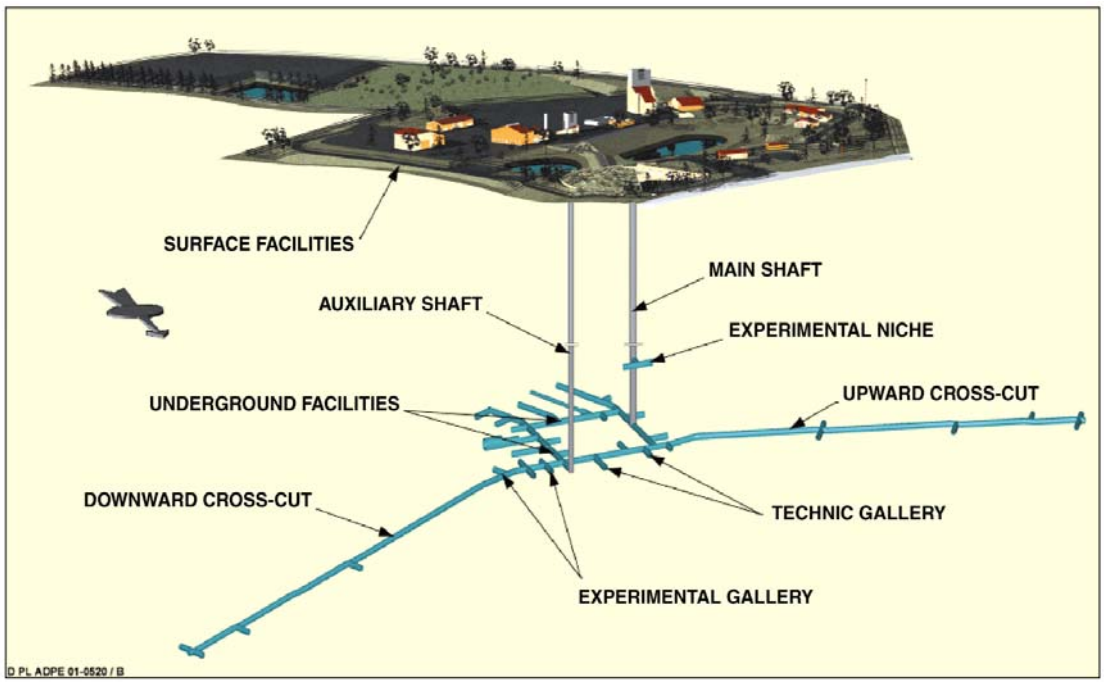

Figure 1.1 General view of the MHM - Underground Research Laboratory at Bure in France /ANDRA 03/

Table 1.1 Experiments to be conducted in the MHM - Underground Research Laboratory at Bure /AND 00/03a,b/, /SU 03/

Experiment	Purpose
SUP	Scientific survey of shaft sinking (geological survey, monitoring of geotechnical behaviour, sampling)
SUG	Scientific survey of the excavation of all the drifts (geological survey, monitoring of geotechnical behaviour, sampling)
REP	Monitoring of the hydromechanical response of the argillite to the sinking of the main access shaft of the underground laboratory
GIS	*In situ* geomechanical characterisation: *in situ* stress, deformability of the argillite in the short and medium term
KEY	Feasibility study of EDZ cut-off
TER	Monitoring of the response of the argillite to the thermal loading in terms of hydraulic, mechanical and chemical disturbances
PEP	*In situ* measurements of permeability and pore pressure in the Callovo-Oxfordian formation
PAC	Water samplings in the Callovo-Oxfordian formation for chemical and isotopic analyses and *in situ* measurement of certain non-conservative parameters
DIR	Characterisation of diffusion and chemical retention of the Callovo-Oxfordian formation by tracing tests

1.2 GRS Proposal for Contribution to the Bure Programme

In recent years, research on clay formations to host a repository for radioactive waste has been initiated in Germany. Site-independent basic research is supported by the German Federal Ministry of Economics and Labour (BMWA). Within this frame R + D concerning clay formations, the research work is carriered out by direct participation in international research projects. GRS intends to participate in the Bure programme and to co-operate with ANDRA on basis of a co-operation agreement. GRS proposed to contribute to the experiments in the underground laboratory at Bure by participating in *in situ* experiments as well as by performing laboratory investigations and numerical

modelling. The GRS proposal was discussed with ANDRA in September 2001 /GRS 01/. It consists of the following laboratory and *in situ* tasks:

- Combined theoretical and laboratory investigations on the coupled thermo-hydro-mechanical (THM) behaviour of the Callovo-Oxfordian argillite,
- Determination of apparent diffusion coefficients for various nuclides,
- Determination of the solution in equilibrium with the argillite,
- Ventilation tests in the laboratory and *in situ*,
- *In situ* measurements of pore pressure and permeability,
- Geoelectric investigations of the excavation disturbed zone (EDZ),
- Gas release measurements.

GRS is already involved in two international projects associated with the Bure research programme:

- MODEX-REP project – Elaboration of hydro-mechanical coupled models by interpretation of the disturbance observed during the sinking of the main shaft of the underground laboratory at Bure /MOD 03/. In the framework of the project GRS performed laboratory investigations on the hydro-mechanical behaviour of the Callovo-Oxfordian argillite, including determination of petrophysical properties, short-term and long-term mechanical behaviour and permeability under relevant *in situ* conditions. The experimental results are presented in /ZHA 02a/ and published in the proceedings of the International Clay Meeting in Reims in 2002 /ZHA 02b/.
- TER-MOCK-UP project (also called HE-D Experiment) – Study of the THM behaviour of the Opalinus clay at the Mont Terri underground laboratory /WIL 03/. A heater experiment is conducted in preparation of the full-scale TER experiment to be conducted in the MHM – URL at Bure. The GRS tasks in this project are: a) laboratory tests on normal and large samples taken from the HE-D heater borehole for determination of the THM behaviour of the Opalinus clay, b) numerical modelling of the HE-D experiment, and c) *in situ* measurements of pore water pressure by using the GRS mini-packer system and gas migration by using Quadruple packer systems before, during and after heating phase.

1.3 Pre-Project for Participation in the Bure Programme

For preparation of the participation in the Bure programme, the Bure pre-project described in this report was started by GRS, under contract number 02E9541 with BMWA, in July 2001.

1.3.1 Objectives

The objectives of the Bure pre-project were:

- Development and testing of laboratory experimental methods to investigate the THM (C) behaviour of clays,
- To select and test a suitable numerical code for the analysis of coupled THM processes in clays,
- To propose a research programme on the basis of the results of the pre-project which contributes in an effective way to the *in situ* experiments envisaged at the MHM-URL Bure.

1.3.2 Experimental Programme

Laboratory investigations on the THMC behaviour of clays need special testing methods. Therefore, one of the main purposes of the pre-project was to develop testing methods and to conduct preliminary experiments. Within the laboratory programme, the following important properties of the Callovo-Oxfordian argillite at the MHM-URL Bure and the Opalinus clay at the Mont Terri URL were experimentally investigated:

- Long-term creep behaviour,
- Swelling and shrinkage,
- Coupled thermo-hydro-mechanical behaviour,
- Diffusion of radionuclides,
- Extraction of pore water.

1.3.3 Modelling Programme

Within the framework of the pre-project, scoping calculations were planned to gain experiences with numerical modelling of coupled THM processes in clays. The computer programme CODE-BRIGHT developed by the Geotechnical Engineering Department of the Technical University of Catalonia in Barcelona /UPC 02/ has been selected for this purpose. CODE-BRIGHT is one of the most suitable THM codes which has been validated by its application to various geological problems, especially to analyse THM experiments in Underground Research Laboratories in clay formations /ALO 98/00/02/, /GEN 98/, /HUE 00/, /MOD 03/, /VOL 96/00/. In the modelling programme, the following work was done:

- Study of the theories applied in CODE-BRIGHT for the description of coupled THM phenomena in geological media,
- Collection of material parameters associated with the constitutive models implemented in the code for different clays,
- Numerical modelling of coupled THM processes in clays under laboratory and *in situ* conditions.

2 Geotechnical Experiments

2.1 Sample Characterisation

2.1.1 Samples

Callovo-Oxfordian argillaceous samples

The Callovo-Oxfordian argillaceous formation at the MHM-URL Bure is located at a depth of approximately 400 m and has a thickness of 130 m. On average the argillite contains 40 % to 45 % clay minerals, 20 % to 30 % carbonates and 20 % to 30 % quartz and feldspar /MOD 03/.

For the laboratory experiments in the framework of the MODEX-REP project, seven core samples were taken at different depths between 434 and 506 m of the borehole EST205 and tested /ZHA 02a/. In addition to these, three more samples were provided by ANDRA for the laboratory programme in the Bure pre-project. These additional samples, named as MSE00837, EST01115 and EST0568, are shown in Figure 2.1. Two of them were drilled in 1995 and another one in 2000. After unpacking of each sample, a few bedding planes perpendicular to the axis of the sample can be visually recognised.

Opalinus clay samples

Because the number of samples from the Callovo-Oxfordian argillite was limited, some additional samples were taken from the Opalinus clay at Mont Terri underground laboratory and used in the testing programme as well. The Opalinus clay has similar properties as the Callovo-Oxfordian argillite. The mineralogical composition of the Opalinus clay is as follows /BOC 02/: clay minerals (kaolinite: 20 – 37 %, illite: 15 – 25 %, mixed layers: 5 – 20 %, chlorite: 4 – 18 %); quartz: 10 – 27 %; calcite: 4 – 29 %; siderite, dolomite and ankerite: 0 – 7.5 %; organic carbon: 0.1 – 0.4 %; accessories: < 3 %. Two samples were taken from the borehole BVE1 drilled parallel to the bedding of the formation close to the ventilation test field (VE), whereas two other samples were taken from the borehole BHE26 drilled ~ 60° inclined to the bedding in the HE-B heater test field. Figure 2.2 shows the samples. A few bedding planes can be visually recognised.

MSE00837
diameter: 84 mm
depth: 504.10-504.49 m
sampling date: 20.01.1995

EST01115
diameter: 84 mm
depth: 504.10-504.49 m
sampling date: 17.12.1995

EST05684
diameter: 100 mm
depth: 486.12-486.44 m
sampling date: 17.02.2000

Figure 2.1 Samples from the Callovo-Oxfordian argillite at the MHM-URL Bure

BVE1: diameter = 72 mm
VE ventilation test field

BHE26: diameter = 100 mm
HE-B heater test field

Figure 2.2 Samples from the Opalinus clay at the Mont Terri URL

Both the Callovo-Oxfordian argillite and the Opalinus clay are indurated sedimentary rocks, differing from less consolidated plastic clays such as the Boom clay at the HADES URL at Mol in Belgium.

From the core samples, cylindrical specimens with different sizes for different tests were carefully prepared by cutting the cores and polishing their end faces. Most of the specimens were directly placed in the respective testing apparatus. Remaining pieces were stored in a container for later use. The storage conditions were room temperature of 20 ± 2 °C and constant relative air humidity of 94 % as prevailing on the samples of the Callovo-Oxfordian argillite at 20 °C /ZHA 02a/.

2.1.2 Measurements of Petrophysical Properties

Measurements of grain density, dry density, bulk density, porosity, water content and degree of water saturation were made according to ISRM suggested testing methods /ISR 81/, see also /ZHA 02a/. The above mentioned physical properties are defined as:

- Grain density

$$\rho_s = \frac{M_s}{V_s} \tag{2.1}$$

with M_s = mass of solids, V_s = volume of solids.

- Bulk density

$$\rho_b = \frac{M}{V} = \frac{M_s + M_w}{V} \tag{2.2}$$

with M = mass of bulk sample, V = volume of bulk sample, M_s = mass of solids, M_w = mass of water.

- Dry density

$$\rho_d = \frac{M_s}{V} \tag{2.3}$$

with M_s = mass of solids, V = volume of bulk sample.

- Porosity

$$\phi = \frac{V_v}{V} 100 = \left(1 - \frac{\rho_d}{\rho_s}\right) \cdot 100 \ (\%) \tag{2.4}$$

with V_v = volume of voids, V = volume of bulk sample, ρ_d = dry density, ρ_s = grain density.

- Water content

$$w = \frac{M_w}{M_s} 100 \ (\%) \tag{2.5}$$

with M_w = mass of water, M_s = mass of solids.

- Relationship between bulk density, dry density and water content

$$\rho_d = \frac{\rho_b}{1 + w/100} \tag{2.6}$$

- Degree of saturation

$$S = \frac{V_w}{V_v} 100 \ (\%) \tag{2.7}$$

with V_w = volume of pore water, V_v = volume of voids.

- Relationship between degree of saturation and the other physical characters

$$S = \frac{w}{\rho_w} \frac{1}{\left(1/\rho_d - 1/\rho_s\right)} = \frac{\rho_d w}{\rho_w \phi} 100 \ (\%) \tag{2.8}$$

with ρ_w = density of pore water.

- Water content of fully-saturated sample (S = 100 %)

$$w_{sat} = 100 \cdot \rho_w \cdot \left(\frac{1}{\rho_d} - \frac{1}{\rho_s}\right) 100 \ (\%) \tag{2.9}$$

Before starting each test, the bulk density of the specimen with natural water content was determined by measuring its volume and weight. The water content was measured on the remaining pieces which were dried in an oven at a temperature of 105°C over 3 days. On basis of the measured bulk density and water content, the dry density can be

established according to equation (2.6). The grain density was measured on the powder produced during the preparation of the specimens by using Beckmann's air Pycnometer (Model 930) with helium gas. The porosity was calculated according to equation (2.4).

The characters of the specimens and the test plan are summarised in Table 2.1a for the Callovo-Oxfordian argillite at the MHM-URL Bure and in Table 2.1b for the Opalinus clay at the Mont Terri URL. During sampling, storage and preparation, the samples lost some water by evaporation. Some of the specimens were dried in room air for special purposes. Therefore, the values of water content, associated bulk density and degree of water saturation represent only the state of the material right before testing, but not the original state *in situ*. In the calculation of the degree of water saturation, the application of the mean grain density of $\rho_s = 2.7$ g/cm^3 for the Callovo-Oxfordian argillite leads to degrees of water saturation over 100 % for some specimens. This indicates that the specimens were nearly or fully saturated.

Table 2.1a Characteristic data of samples from the Callovo-Oxfordian argillite at the MHM-URL Bure

Specimen	Diameter D (mm)	Length L (mm)	Depth (m)	Grain density ρ_s (g/cm^3)	Dry density ρ_d (g/cm^3)	Bulk density ρ_b (g/cm^3)	Water content w (%)	Porosity ϕ (%)	Degree of saturation S (%)	Test plan
EST05481-01-II	100	200	434.52-434.84	2.70	2.30	2.41	4.99	15.0	76.5	creep test
EST05671-01-II	100	180	484.05-487.37	2.70	2.27	2.44	7.38	15.8	106.0	creep test
EST05671-02-=	45	90	484.05-487.37	2.70	2.27	2.44	7.38	15.8	106.0	creep test
EST05671-03-=	45	90	484.05-487.37	2.70	2.27	2.44	7.38	15.8	106.0	creep test
EST05582-02-II	45	90	463.17-463.49	2.70	2.21	2.40	8.73	18.2	106.0	creep test
EST05582-03-II	45	90	463.17-463.49	2.70	2.21	2.40	8.73	18.2	106.0	creep test
EST05630-02-=	45	90	474.00-474-32	2.70	2.18	2.38	8.93	19.2	101.0	creep test
EST05684-01-II	100	200/136.5	486.12-486.44	2.70	2.26	2.41	8.58	16.6	116.0	creep test
MSE00837-01-II	82.5	163.2	589.00-589.30			2.42				creep test
EST05630-04-=	49.15	22.15	474.00-474-32	2.70	2.18	2.27	4.1	19.2	46.6	swelling test
EST05547-07-II	40	80	454.38-454.70	2.70	2.22	2.39	7.1	17.8	88.6	swelling test
EST05490-01-=	50	85.1	437.30-437.62	2.70	2.25	2.54	7.50	16.9	99.9	THM test
EST05684-02-=	50	85.4	486.12-486.44	2.70	2.26	2.45	8.58	16.6	116.0	THM test

Table 2.1b Characteristic data of samples from the Opalinus clay at the Mont Terri URL

Specimen	Diameter D (mm)	Length L (mm)	Location	Grain density ρ_s (g/cm^3)	Dry density ρ_d (g/cm^3)	Bulk density ρ_b (g/cm^3)	Water content w (%)	Porosity ϕ (%)	Degree of saturation S (%)	Test
BVE1-01	71.8	140	VE test field	2.75	2.25	2.41	5.8	18.0	72.5	creep test
BVE1-02	71.8	140	VE test field	2.72	2.25	2.40	3.4	17.2	44.5	creep test
BVE1-03	50	100	VE test field	2.75	2.28	2.42	6.12	16.9	82.4	THM test
BHE26-01	100	200	HE-B test field	2.73	2.27	2.41	5,6	16.8	75.7	creep test
BHE26-02	100	200	HE-B test field	2.73	2.27	2.43	3.2	16.8	43.2	creep test

2.2 Long-Term Creep Experiments

In the framework of the MODEX-REP project, a number of uniaxial creep tests was performed on Callovo-Oxfordian argillaceous specimens, wherein the long-term mechanical behaviour of the argillite was studied by taking into account various factors such as load level, anisotropy and scale effect. The results are reported in /ZHA 02a/b/. Most of the tests have been continued up to now and lasted over an exceptionally long duration of more than 2.5 years. Additional creep tests on two Callovo-Oxfordian specimens and four Opalinus specimens were carried out to investigate the creep behaviour under very low loads.

2.2.1 Testing Method

The tests were conducted in the GRS creep rigs, one of which was developed for simultaneous creep tests on five specimens at ambient temperature. Four other creep rigs allow two specimens being tested in separated chambers at elevated temperature up to 200°C. Figure 2.3 shows both types of creep rigs.

All specimens were sealed in rubber jackets or in alumina-sheeted plastic foils and steel platens to prevent water loss during the tests. Axial load was applied to the specimens instantaneously and then maintained constant. This condition is controlled by means of an oil balance with an accuracy higher than ± 0.5 % of readings. Multi-step loads ranged from 0.6 to 18 MPa. Specimen deformation was measured by displacement transducers (LVDT) with an accuracy better than ± 0.2 % of readings. The testing temperature maintained relatively constant between 22.6 °C and 23.8 °C, except for a few peak changes, as shown in Figure 2.4. The testing temperatures for the specimens placed in the chambers fluctuated within ± 0.1 °C, while the temperature in the room fluctuated within ± 1.0 °C.

According to the loading conditions, the creep tests were divided into different groups, each of them consisting of two or five specimens loaded in the same rig. Four groups I, II, III and IV started on 11. April 2001 during the MODEX-REP project and three additional groups V, VI and VII started later. The tests of groups I and III including four Callovo-Oxfordian specimens are reported in /ZHA 02a/. The others are presented below. The loading conditions and the creep durations of the tests are summarised in Table 2.2. The tests of groups II and IV including seven Callovo-Oxfordian specimens

under loads from 2 to 18 MPa lasted for more than 2.5 years with each creep phase between 1 and 18 months. The creep tests of group V were conducted on two Callovo-Oxfordian specimens under very low loads of 0.7 and 1.0 MPa for 8 months. The creep tests of groups VI and VII on four Opalinus specimens focused on investigating the influence of the water content on the creep behaviour. Most of the tests are still continuing.

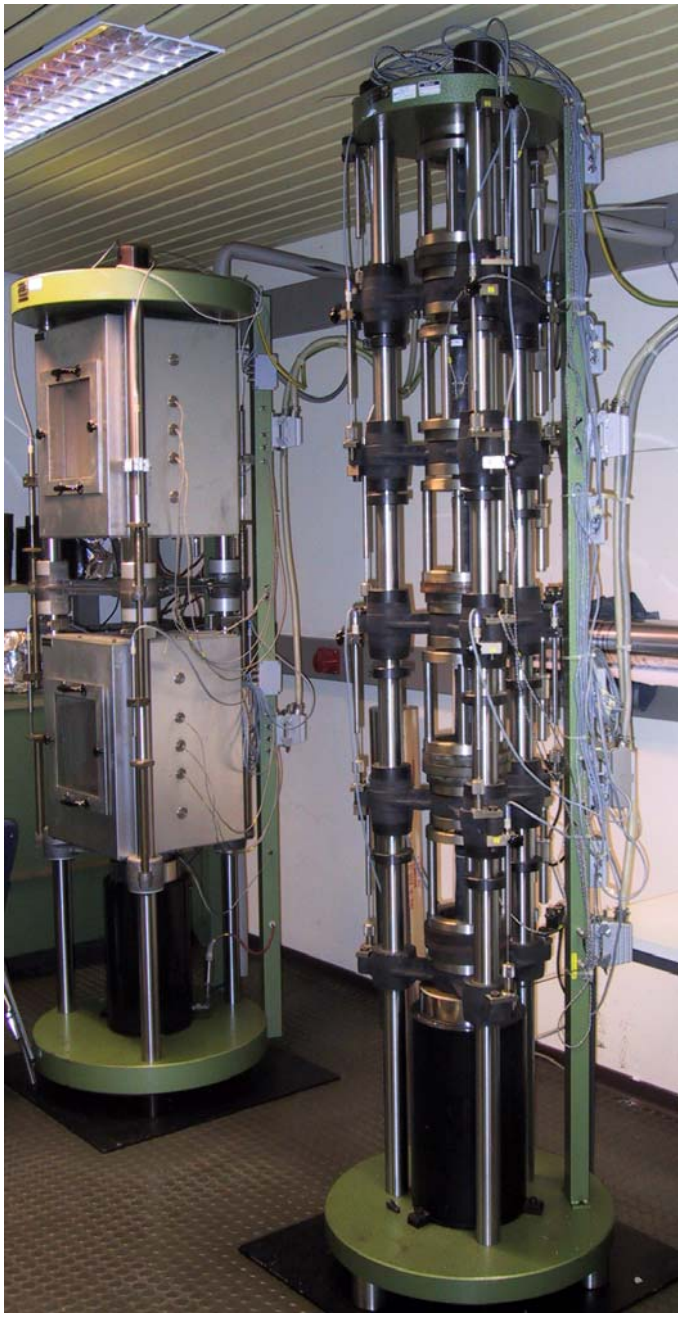

Figure 2.3 Uniaxial creep rigs at the GRS geotechnical laboratory

Table 2.2 Overview of uniaxial creep tests conducted on the Callovo-Oxfordian argillite and the Opalinus clay

Test group	Specimen	Depth (m)	Size D/L (mm)	Bulk density (g/cm^3)	Water content (%)
Callovo-Oxfordian argillaceous specimens					
II	EST05481-01-II	434.6	100/200	2.46	5.0
	EST05671-01-II	484.2	100/180	2.45	7.4
IV	EST05582-03-II	463.2	45/90	2.40	8.7
	EST05630-02-=	474.1	45/90	2.38	8.9
	EST05671-02-=	484.1	45/90	2.44	7.4
	EST05582-02-II	463.2	45/90	2.41	8.7
	EST05671-03-=	484.1	45/90	2.44	7.4
V	EST05684-01-II	486.3	100/137	2.41	8.6
	MSE00837-01-II	589.1	83/163	2.42	
Opalinus clay specimens					
VI	BVE1-01-=	VE test field	72/140	2.41	5.8
	BVE1-02-=	VE test field	72/140	2.40	3.4
VII	BHE26-01-/~60°	HE test field	100/200	2.41	6.6
	BHE26-02-/~60°	HE test filed	100/200	2.43	3.2

Table 2.2 continued: Loading conditions with axial load σ_1 in MPa and creep duration Δt in days for each creep step

Specimen	Load	1. step	2. step	3. step	4. step	5. step	6. step	7. step	8. step	Remarks
	to bedding	$\sigma_1/\Delta t$	$\sigma_1/\Delta t$	$\sigma_1/\Delta t$	$\sigma_1/\Delta t$	$\sigma_1/\Delta t$	$\sigma_1/\Delta t$	$\sigma_1/\Delta t$	$\sigma_1/\Delta t$	
Callovo-Oxfordian argillaceous specimens										
EST05481-01-II	perpendicular	3.0/21	6.0/54	9.9/96	11.9/76	9.9/74	11.9/46	13.9/553		continue
EST05671-01-II	perpendicular	3.0/21	6.0/54	9.9/96	11.9/76	9.9/74	11.9/46	13.9/553		continue
EST05582-03-II	perpendicular	5.0/21	8.0/54	12.0/96	15.0/198	18.0/553				continue
EST05671-02-=	parallel	5.0/21	8.0/54	12.0/96	15.0/198	18.0/553				continue
EST05671-03-=	parallel	5.0/21	8.0/54	12.0/96	15.0/198	18.0/553				continue
EST05582-02-II	perpendicular	5.0/21	8.0/54	12.0/96	15.0/76	15.0/122 drying	18.0/261 isolated	18.0/152 wetting	18.0/140 isolated	continue
EST05630-02-=	parallel	5.0/21	8.0/54	12.0/96	15.0/76	15.0/122 drying	18.0/261 isolated	18.0/152 wetting	18.0/140 isolated	continue
EST05684-01-II	perpendicular	0.7/238								continue
MSE00837-01-II	perpendicular	1.0/238								continue
Opalinus clay specimens										
BVE1-01-=	parallel	0.6/1.0								ruptured at 5MPa
BVE1-02-=	parallel	0.6/1.0	5.2/28							end
BHE26-01-/~60°	60° inclined	0.7/28								ruptured at 5MPa
BHE26-02-/~60°	60° inclined	0.7/28	5.0/80							end

2.2.2 Results

The results of the early test phases of the first 400 days which were already obtained on the Callovo-Oxfordian specimens of groups II and IV are presented in /ZHA 02a/b/. In this report, results of the late test phases are presented for each group.

Group II

The two Callovo-Oxfordian specimens EST05481-01-II and EST05671-01-II with D/L = 100 mm / 200 mm are loaded in the direction perpendicular to the bedding plane in seven creep steps as shown in Figure 2.4 presenting the temperature and load conditions and in Figure 2.5 presenting the axial strain versus time. It is to be noted that the specimen EST05671-01-II was taken from the rheological zone B' with relative low carbonate content, while the specimen EST05481-01-II originated from the stiff zone A' with high carbonate content /AND 00/, /MOD 03/. On the other hand, the water content of w = 7.4 % in the specimen EST05671-01-II is higher than w = 5.0 % in the specimen EST05481-01-II. From Figure 2.5 it is obvious that the specimen EST05671-01-II was creeping faster than the specimen EST05481-01-II at each constant load. The creep step at 13.9 MPa lasted for more than 18 months, but was unfortunately interrupted for 15 days due to a failure of the testing system. Reloading to the previous level again did not result in the same strain state as measured before until about three months. Whereas the specimen EST05671-01-II was creeping continuously with time, the creep strain of the specimen EST05481-01-II was almost unmeasurable over the last 7 months. The low creep ability of the specimen EST05481-01-II might be due to both low water content and high carbonate content, which lead to a high stiffness.

To examine whether there exists steady state of creep in the argillite, the creep rates were determined from the strain increments in different time intervals of 10 to 20 days. Figure 2.6 presents the creep rates as a function of axial strain for the last period of 300 days at 13.9 MPa. The creep rate of the specimen EST05481-01-II varies over a large range between $3 \cdot 10^{-12}$ s^{-1} and $3 \cdot 10^{-11}$ s^{-1}. From this, steady state creep cannot be clearly recognised. In contrast to this, the creep rate of the specimen EST05671-01-II tends to be constant at $5.7 \cdot 10^{-11}$ s^{-1} with a relatively small scatter of $\pm 1.5 \cdot 10^{-11}$ s^{-1}, indicating steady state creep. The average creep rate of the specimen EST05671-01-II with relatively low carbonate content and high water content is about 6 times higher than that of the specimen EST05481-01-II.

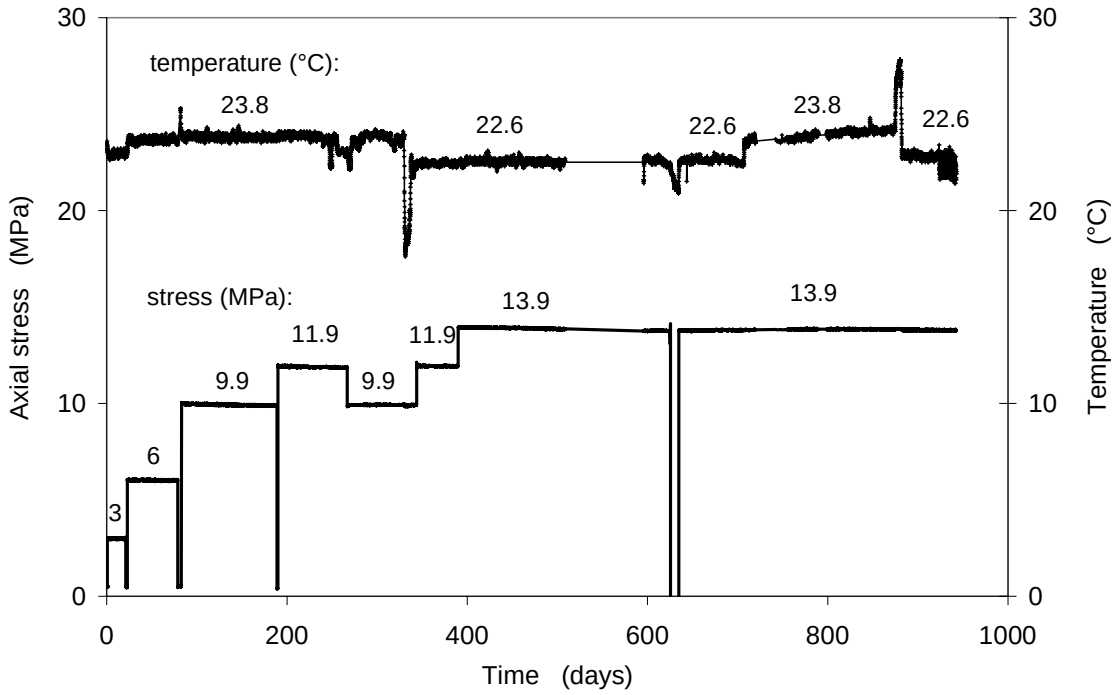

Figure 2.4 Creep testing conditions for Callovo-Oxfordian specimens EST05481-01 and EST05671-01

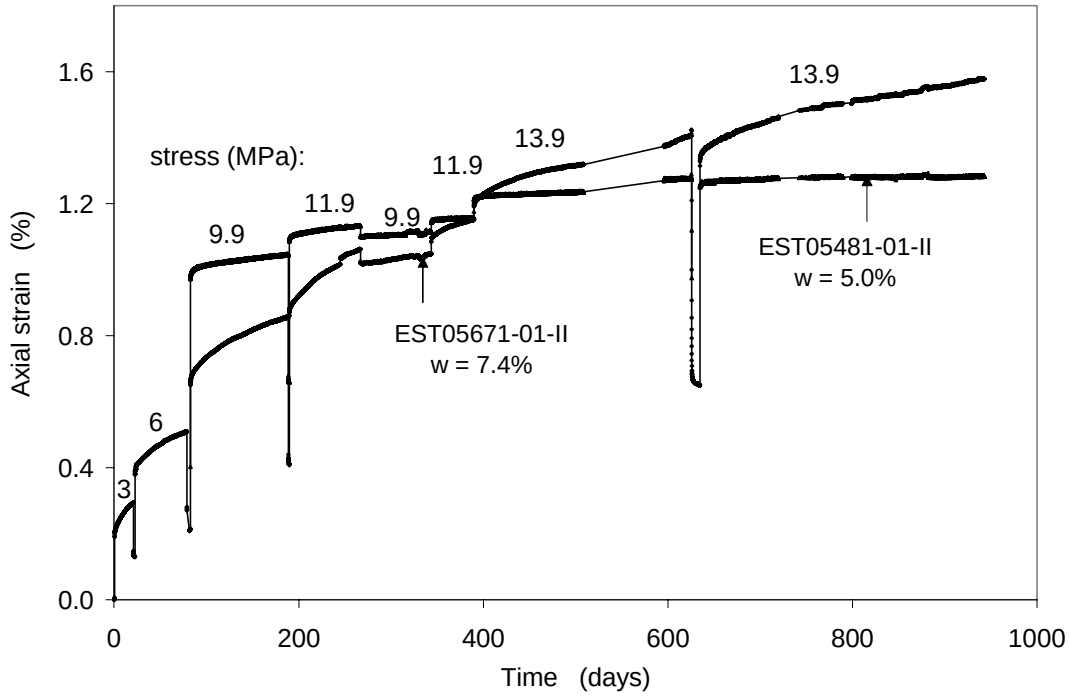

Figure 2.5 Creep curves of Callovo-Oxfordian specimens EST05481-01 and EST05671-01

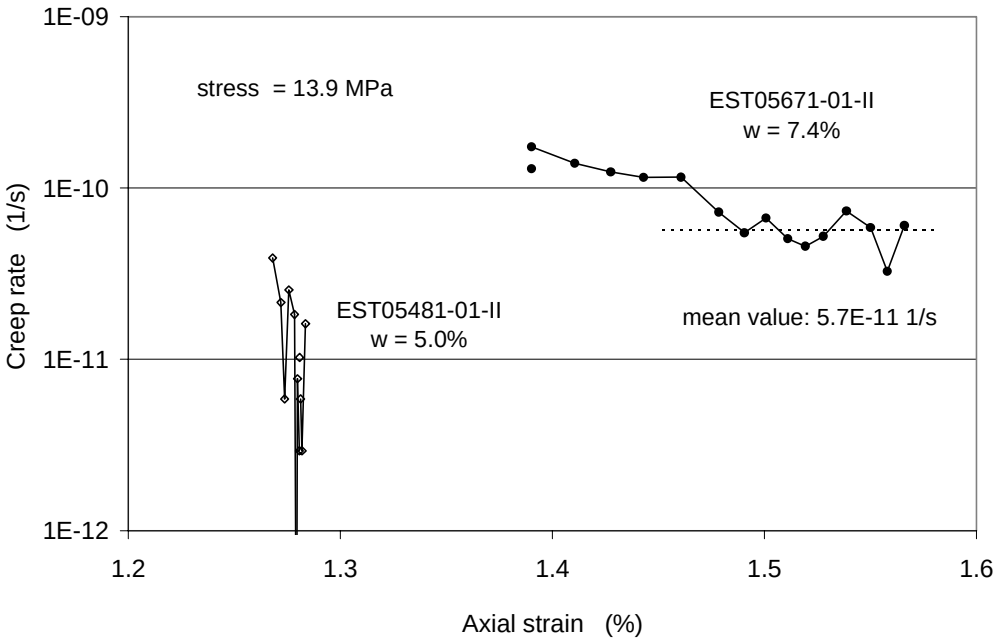

Figure 2.6 Creep rates as a function of strain for Callovo-Oxfordian specimens EST05481-01 and EST05671-01

Group IV

Five Callovo-Oxfordian specimens with D/L = 45 mm / 90 mm were tested simultaneously at room temperature in four creep steps. Two specimens EST05582-02-II and EST05582-03-II were loaded in the direction perpendicular to the bedding, while the other three specimens EST05630-02-=, EST05671-02-=, and EST05671-03-= were loaded parallel to the bedding. Figure 2.7 shows the temperature with fluctuation of ΔT = ± 1°C and loads with thermally-induced scattering of ± 0.2 MPa.

The creep curves of the five specimens are illustrated in Figure 2.8. It can be seen that the creep curves evolve very parallel and the total strains perpendicular to the bedding are larger than parallel to the bedding. This suggests that the pure creep behaviour of the argillite is not significantly dependent on the loading directions. Two specimens EST05582-02-II and EST05630-02-= were dried and wetted at 15 and 18 MPa to examine shrinkage and swelling, presented in chapter 2.3.4. The creep rates determined on the other three specimens for the last 300 days at 18 MPa are plotted in Figure 2.9. Generally, the creep rates decrease from 10^{-10} s^{-1} to $5 \cdot 10^{-12}$ s^{-1} with creep strain. Steady state creep can thus not be recognised.

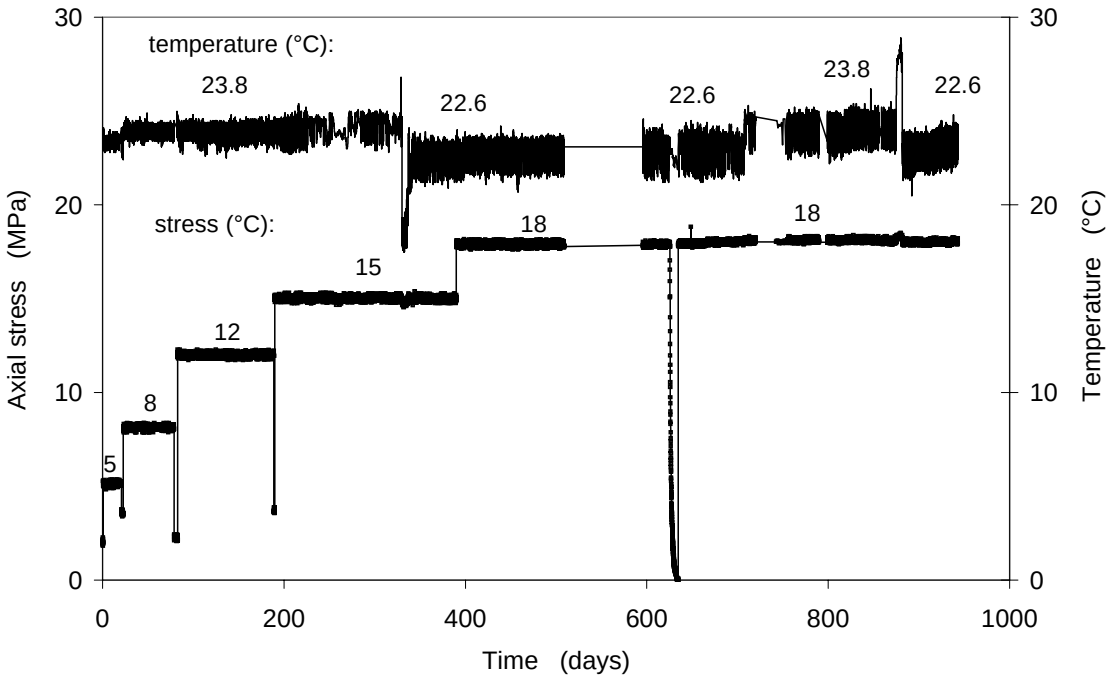

Figure 2.7 Testing conditions for Callovo-Oxfordian specimens EST05630-02, EST05582-02/-03 and EST05671-02/-03

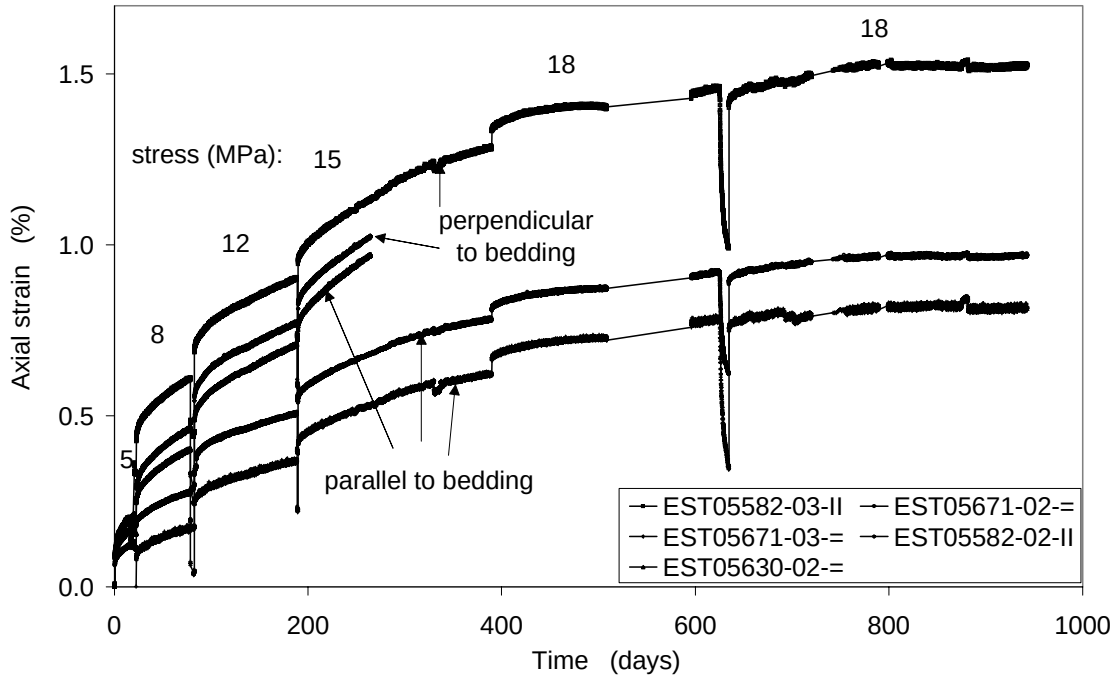

Figure 2.8 Creep curves of Callovo-Oxfordian specimens EST05630-02, EST05582-02/-03 and EST05671-02/-03

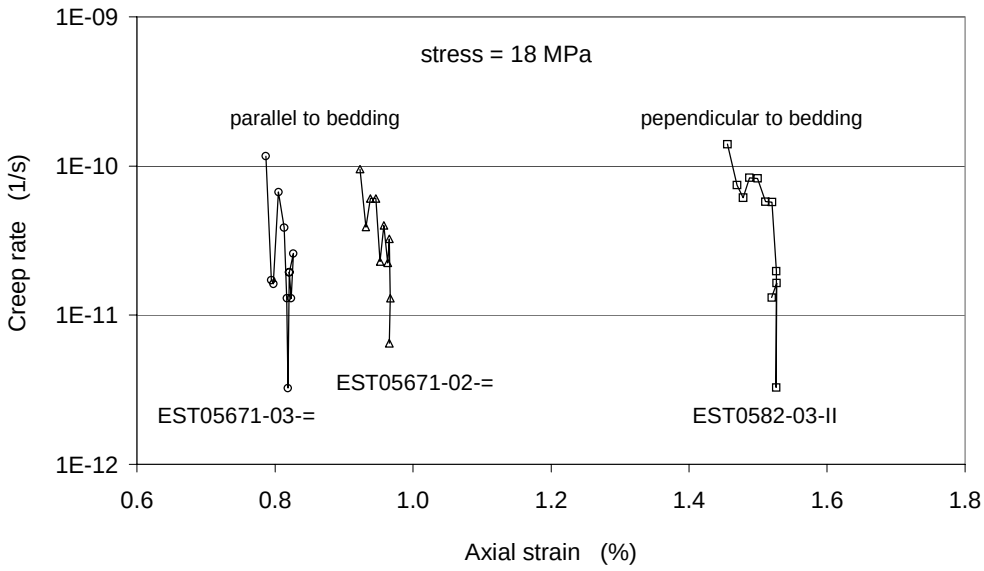

Figure 2.9 Creep rates as a function of strain for Callovo-Oxfordian specimens EST05582-03 and EST05671-02 / -03

Group V

Up to now, most of the creep tests on the Callovo-Oxfordian argillite were made under loads higher than 2 MPa /LEB 00/, /GAS 02/, /SU 99/, /ZHA 02a/b/. From the observations of creep strains under low deviatoric stresses of 2 – 3 MPa, it was concluded that there is no lower stress threshold for the onset of creep. In order to confirm this conclusion, two further uniaxial creep tests on the Callovo-Oxfordian specimens EST05684-01-II and MSE00837-01-II were carried out under much lower loads of 0.73 and 1.0 MPa. Figure 2.10 shows the test results. It is very obvious that both specimens which are almost saturated deformed steadily with time. The creep curves are also quite linear, except for a few sudden changes mainly due to temperature changes. Creep rates determined for the time interval of 55 to 238 days are illustrated as a function of creep strain in Figure 2.11. The creep rate of each specimen fluctuates slightly over the creep strain intervals of 0.06 to 0.1 %. This strongly suggests that steady state creep seemed to be reached even under the low stresses. The mean creep rate of $6.7 \cdot 10^{-11}$ s^{-1} obtained at 0.73 MPa for specimen EST05684-01-II is somewhat higher than $4.5 \cdot 10^{-11}$ s^{-1} obtained at 1.0 MPa for specimen MSE00837-01-II. This might be due to different petrophysical and mineralogical properties of the specimens.

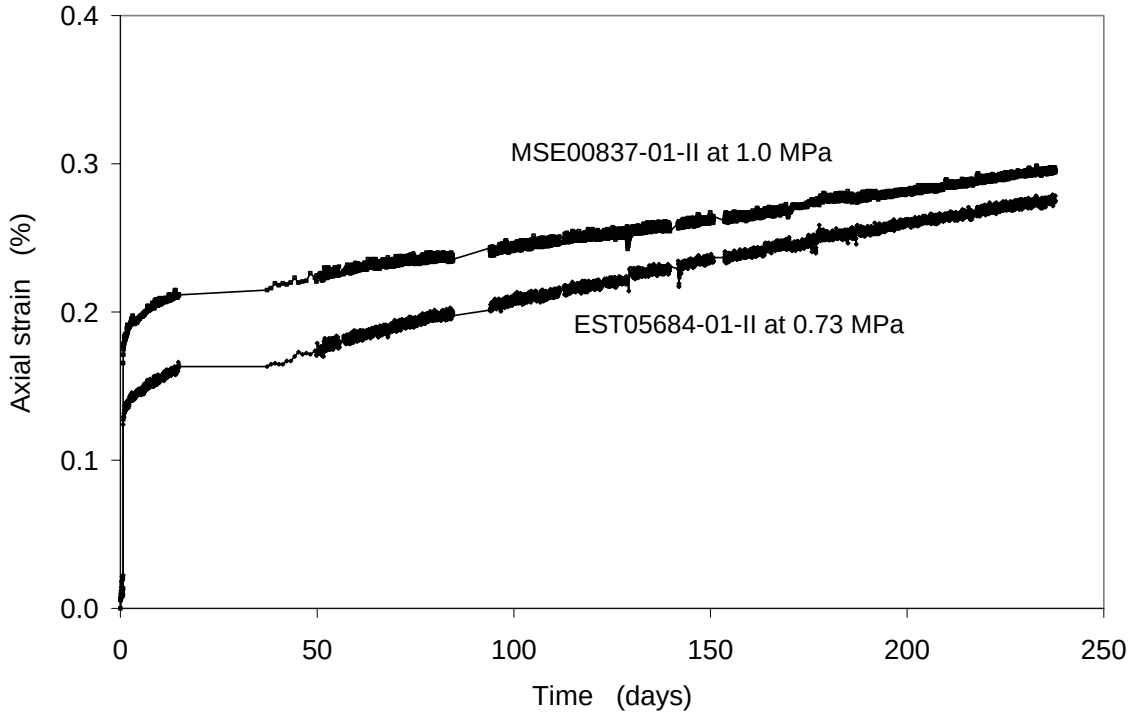

Figure 2.10 Creep curves of Callovo-Oxfordian specimens EST05684-01 and MSE00837-01

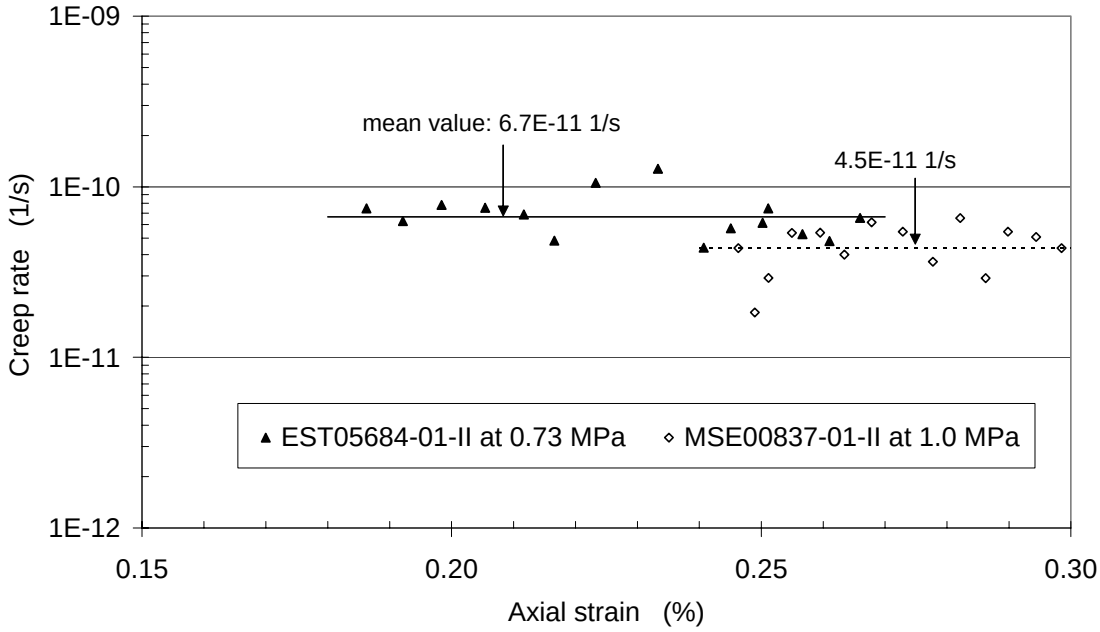

Figure 2.11 Creep rates as a function of strain for Callovo-Oxfordian specimens EST05684-01 and MSE00837-01

Group VI and VII

In order to examine the influence of the water content on the creep behaviour of the indurated clays, four tests in the two groups VI and VII were conducted on the Opalinus specimens BVE1-01-= / -02-= drilled parallel to the bedding and BHE26-01-/~60° / -02-/~60° drilled ~ 60° inclined to the bedding. Before starting the tests, one of both specimens in each group was exposed to the room air and dried to a water content of w = 3.42 % for BVE1-02-= and w = 3.2 % for BHE26-02-/~60°, respectively, while the others were kept at water contents of w = 5.80 % for BVE1-01-= and w = 5.60 % for BHE26-01-/~60°. The specimens were uniaxially loaded in two steps of 0.6 – 0.7 MPa and 5.0 – 5.2 MPa. Figure 2.12 and 2.13 compare creep curves of the specimens with different water contents under the same load conditions in each group.

Comparing both figures, very similar phenomena can be found:

- all the specimens were creeping under very low stresses of 0.6 to 0.7 MPa, independent on the water content in the test range;
- the specimens with the high water contents of 5.6 – 5.8 % ruptured as the axial load rose up to 5.0 – 5.2 MPa;
- the creep curves at 0.7, 5.0 and 5.2 MPa seem to be linear after short transient creep, independent of the water content.

The creep rupture stress of about 5 MPa is equivalent to the lower limit of the uniaxial compressive strength of 10 ± 6 MPa measured on Opalinus specimens /RA 01/. From these limited tests, a significant dependence of the pure creep behaviour on water content can not be concluded, yet.

2.2.3 Conclusions and Remarks

From the long-term creep experiments on the Callovo-Oxfordian argillite and the Opalinus clay, the following conclusions can be drawn:

- the Callovo-Oxfordian argillite and the Opalinus clay exhibit pronounced creep strains under very low uniaxial loads of 0.6 to 1.0 MPa, confirming that there exists no stress threshold for the onset of creep in the indurated clays;

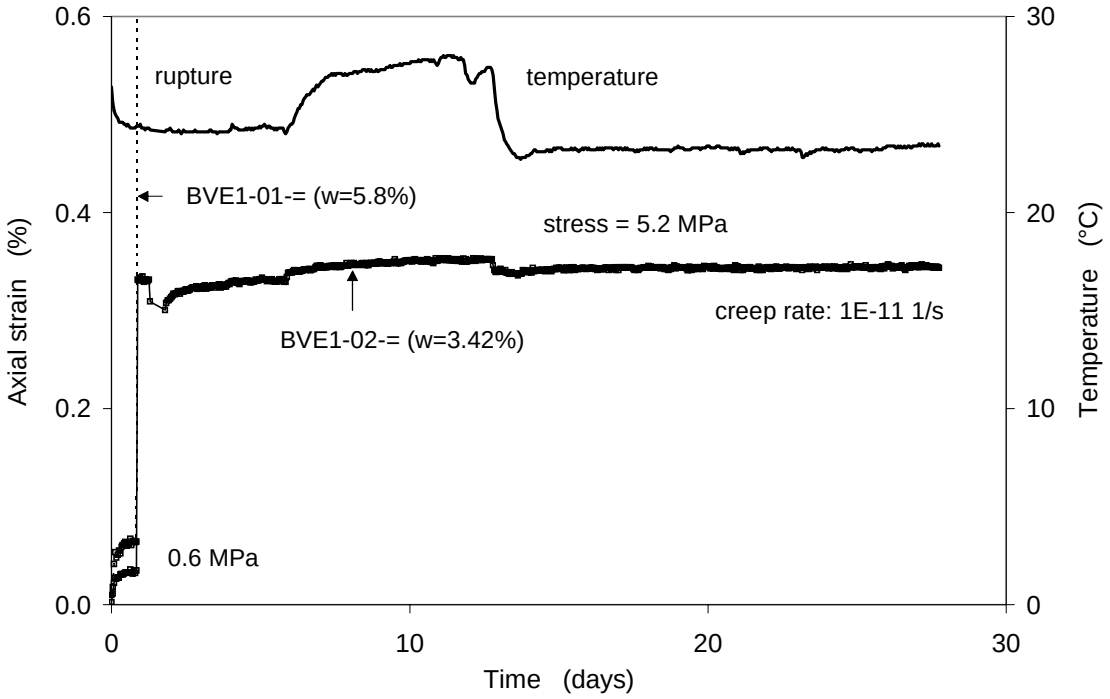

Figure 2.12 Creep curves of Opalinus specimens BVE1-01/-02 taken from the VE ventilation test field in the Mont Terri URL

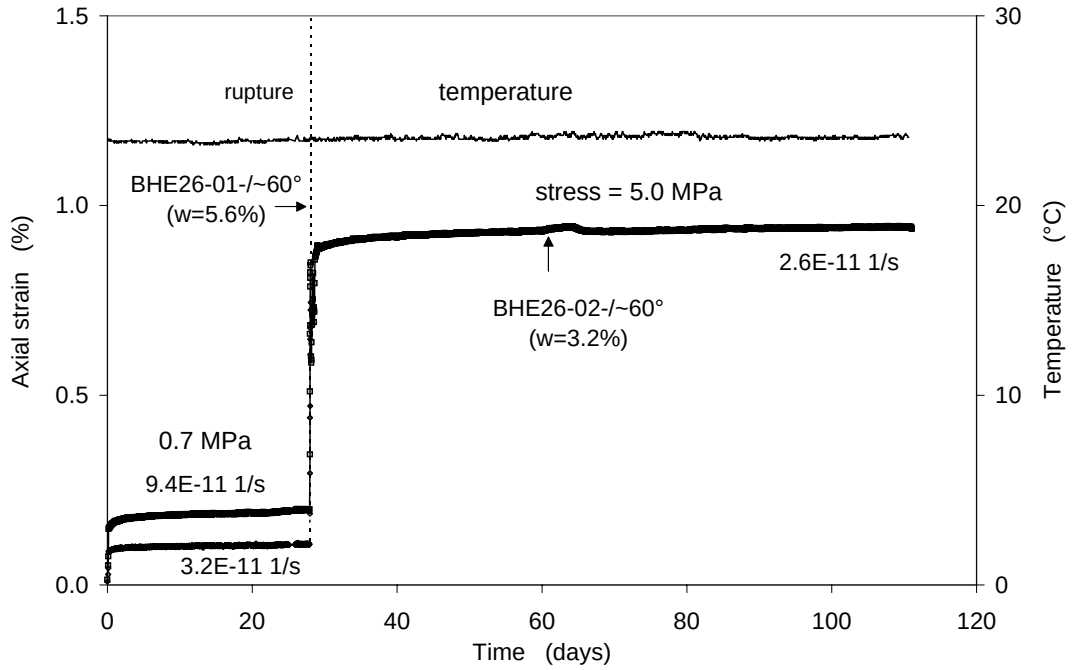

Figure 2.13 Creep curves of Opalinus specimens HEB26-01/-02 taken from the HEB heating test field in the Mont Terri URL

- no cease of creep was observed even over more than 18 months under different load levels;
- steady state creep were observed on some specimens after a transient creep phase over weeks to months at low stresses of up to 5 MPa and over months to years at higher stresses;
- creep ruptures were observed on the Opalinus specimens with relatively high water contents at about 5 MPa uniaxial load but not on the air dried ones, indicating that the strength of the clay increases with decreasing water content;
- high carbonate content and low water content slow down the creep;
- pure creep strain and creep rate parallel and perpendicular to the bedding are almost the same, suggesting that the anisotropy effect is negligible on the long-term behaviour.

It is to be noted that there still exists today a large degree of uncertainty on the extrapolation of creep values measured on specimens over several months to periods of ten to thousand years. The extrapolation must be based on a better understanding of the micro-mechanisms governing the long-term mechanical behaviour of indurated clays. According to the current state of knowledge /AND 03a/, different mechanisms may lie behind the creep, for example:

- rebalancing of hydraulic pressures because of the very low permeability of the indurated clays;
- deformation of the mineral skeleton by sliding clay flakes;
- subcritical propagation of fissures and the possible creation of new fissures;
- stress-induced solution transfer (pressure solution) because the indurated clays contain a relatively high amount of carbonates /VAL 02/.

Additionally, it is to be pointed out that interparticle water-films may play a dominating role in deformation of indurated clays, regarding some theoretical considerations (see chapter 2.3.1).

To predict the very long-term mechanical behaviour of the indurated clays as host for the disposal of high-level and long-lived radioactive wastes, physically-based constitutive laws are needed. Therefore, future research work shall focus on

investigations of physical mechanisms governing the long-term behaviour of indurated clays and the corresponding development of predictive models.

2.3 Swelling Experiments

2.3.1 Theoretical Considerations

Swelling in clays is the physico-chemical process by which water is drawn into the material and interacts with particle surfaces. The clay-water interactions cause adsorption of water on the internal and external surfaces of clay minerals, forming electrostatic double-layers. In natural plastic and indurated clays, there exist also other mineral particles and diagenetic bonds. Most of water may be adsorbed on clay particle surfaces and so strongly bound that it may not be able to participate in advective transport under normally-encountered pressure gradients. There may also be small amounts of free water in relatively large pore spaces. Figure 2.14 illustrates schematically the conceptual inner structure of a indurated clay.

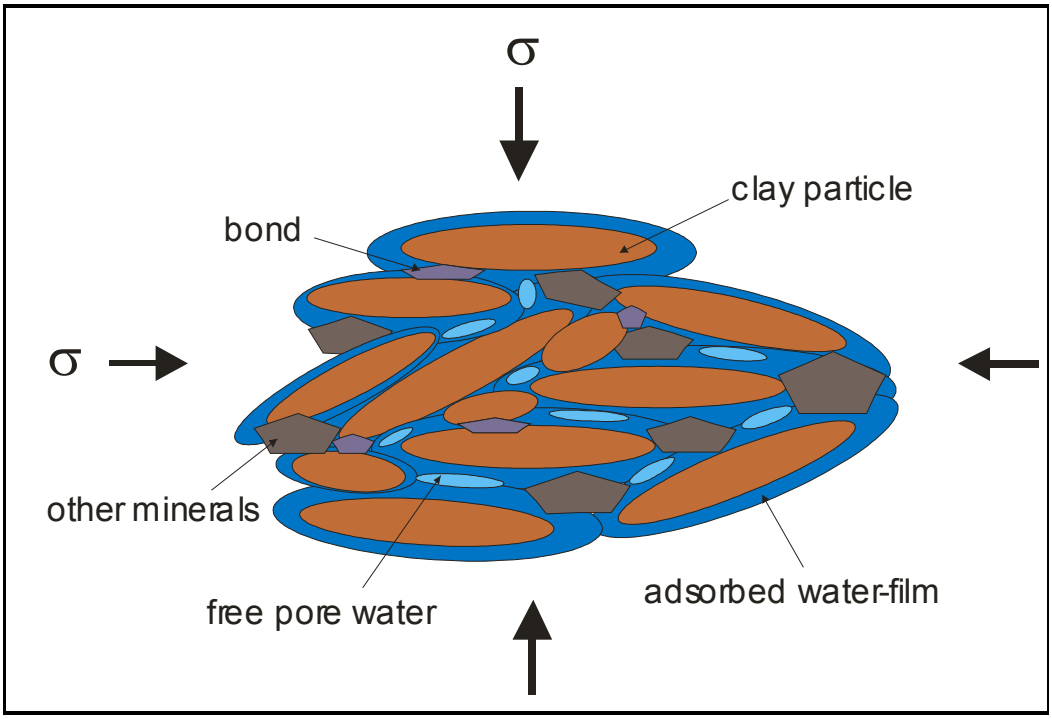

Figure 2.14 Schematic inner structure of a indurated clay

In the narrow spaces between clay particles the double-layers are usually overlapping. This generates local over pressures which develop in the water-films. Often, the over pressure is also called the disjoining pressure. The magnitude of the disjoining pressure increases with decreasing water-film thickness. The average disjoining pressure is equivalent to the swelling pressure.

Isotropic total stress in clays might be taken to be the sum of the interparticle stress σ_i acting in the solid skeleton and the water-film pressure p_{fm} consisting of the disjoining pressure Π_D and the pressure p_w of free pore water

$$\sigma = \sigma_{eff} + p_w = (\sigma_i + \Pi_D) + p_w \tag{2.10}$$

where the conventional (Terzaghi) effective stress is defined as the sum of the interparticle stress and the disjoining pressure, and osmotic effects are not considered. If the pores occupied by free water are interconnected and open to external water, the free pore water pressure is then equivalent to the external water pressure.

Saturated clays may behave as perfect colloids and then the interparticle stress σ_i is zero. For such materials, Horseman et al. /HOR 96/ proposed that the isotropic effective stress σ_{eff} is only equal to the disjoining pressure Π_D of the interpaticle water-films, or equal to the swelling pressure

$$\sigma_{eff} = \Pi_D \tag{2.11}$$

The isotropic total stress σ can then be expressed by

$$\sigma = \sigma_{eff} + p_w = \Pi_D + p_w \tag{2.12}$$

When the external water pressure in equilibrium with the free pore water is zero (p_w = 0), the externally-applied total stress is equal to the average disjoining pressure

$$\sigma = \sigma_{eff} = \Pi_D \tag{2.13}$$

This stress concept implies that the interparticle water-films in indurated clays are stress-supporting and carry the lithostatic stress.

Additionally, Horseman et al. /HOR 96/, /ROD 99/ also suggested that (a) there should be a threshold entry pressure for advective transport of water into the water-film with no flow possible until the external water pressure is raised by an amount of $\Delta p_w = \Pi_D$, and (b) gas will enter an initially water-saturated clay when its pressure is sufficient to overcome the sum of the capillary pressure at the entrance of the flow path and the pore water pressure in the water-film ($p_{fm} = \Pi_D + p_w$) .

It is to be noted that the disjoining pressure acting in interparticle water-films may change thermodynamically. When the clay is de-saturated to a threshold degree of water saturation, solid particles will take direct contacts with each other and carry effectively the external total stress. For this case, Horseman's stress concept (Eqs. 2.11 - 2.13) is not adequate. Equation (2.10) may be applicable for unsaturated clays when the water saturation is below the aforementioned threshold.

From the above discussions, Horseman's stress concept may play a key role for understanding of THM processes in clays. In order to provide experimental evidences for the stress concept and to examine the stress-supporting capability of interparticle water-films in indurated clays, some specific swelling experiments were considered and performed on the Callovo-Oxfordian argillite at the GRS geotechnical laboratory:

- *Traditional swelling pressure test* on a volume-constraint specimen immersed in water at zero external water pressure, $p_w = 0$;
- *Uniaxial swelling pressure test*, in which the uniaxial swelling pressure is measured on a specimen under axially-fixed and laterally-unconstraint conditions by changing water content or thickness of interparticle water-films;
- *Uniaxial swelling strain test*, in which the axial swelling strain is measured on the specimen under axially-loaded and laterally-unconstraint conditions by changing water content or thickness of interparticle water-films.

The mechanical conditions of the last two tests are like those of uniaxial relaxation and creep tests, respectively. In the uniaxial swelling pressure and strain tests, the water content is changed not by immersing the specimens to water but by pumping water vapour or dry air through them.

2.3.2 Swelling Pressure in Volume-Constraint Conditions

A traditional swelling cell developed by GRS /HER 02/ (Figure 2.15) was used to measure the swelling pressure of the Callovo-Oxfordian argillite in a constrained volume. A disk specimen (EST05630-04-=) with a water content of 4.1 % was placed in the cell of 49.2 mm inner diameter and 22.2 mm height. The initial dry density of 2.18 g/cm^3 was measured and the porosity of 19.2 % was calculated. The axis of the specimen is parallel to the bedding. First, the specimen was axially loaded in the cell up to 10 MPa. Because the load is lower than the overburden pressure at the sampling depth of 455 m (about 11 MPa), the structure of the specimen could only be modified in the elastic domain. After unloading, the specimen was fixed by the screw cap. At fixed volume the specimen was then subjected to an external water pressure of 10 MPa by pumping clay water especially prepared by mixing distilled water with the clay powder. The application of the high injection pressure was to ensure the water to enter into the specimen and to resaturate it in short time. The saturation phase lasted for about 7 days. To determine the pure swelling pressure remaining in the specimen, the water pressure was dropped down to zero for more than 450 days. During the test, the axial total stress was measured by a load transducer installed between the load piston and the top plate.

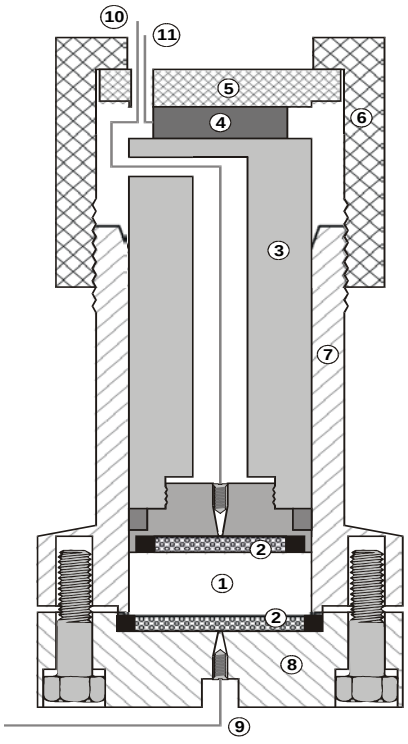

1. specimen
2. sinter filter
3. load piston
4. pressure transducer
5. top plate
6. screw cap
7. pressure tube
8. bottom plate
9. inlet
10. outlet
11. cable

Figure 2.15 GRS swelling cell /HER 02/

According to equation (2.13), the swelling pressure or the average disjoining pressure can then be determined.

Figure 2.16 shows the measurements of the injection pressure and the axial total stress. During the injection phase at the pressure of 10 MPa, an axial total stress of 9.6 MPa was registered. No water flux out of the specimen was observed. The difference between the measured total stress and the injection pressure is probably produced by friction between the cell and the load piston and the specimen as well. As the injection pressure was reduced down to zero, the total stress fell to about 2.4 MPa. After about 100 days, the total stress remained constant at 2.0 MPa over more than 1 year. Assuming that the friction resistance of 0.4 MPa remained during the whole period of the test, the swelling pressure can be estimated to 2.0 – 0.4 = 1.6 MPa. This value is comparable with the results obtained on the Opalinus specimens with pure water and different solutions, i.e. the swelling pressure of less than 2 MPa as reported by /THU 99/. However, the measured swelling pressure is much lower than the expected one, i.e. the lithostatic stress of about 11 MPa. Reasons for the low swelling pressures measured might be that:

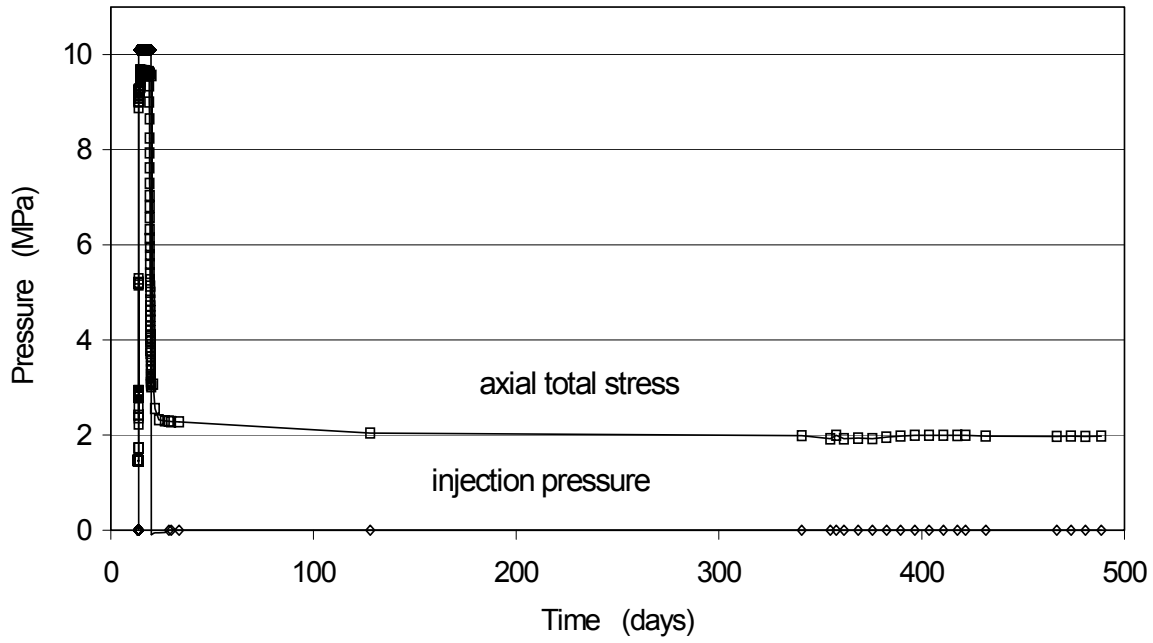

Figure 2.16 Swelling pressure of Callovo-Oxfordian specimen EST05630-04 measured in GRS swelling cell

- the compact argillite is practically impermeable for water to move in, so that the specimen could not be fully resaturated during the short injection time at the pressure of 10 MPa;
- because the clay water was used, the physico-chemical reactions with clay minerals in the specimen might be not strong enough to generate high disjoining pressure in the water-films;
- even if strong clay-water reactions occurred, clay minerals close to the entering water might be expanded so highly that the local pore spaces are more or less closed, making more water entering into the specimen impossible.

2.3.3 Uniaxial Swelling Pressure

Traditionally, swelling pressure of a clay material is investigated on a volume-constraint specimen immersed in water, just like the test presented in chapter 2.3.2. The uniaxial relaxation tests made on the Callovo-Oxfordian specimens show that the periodic fluctuation of temperature has a significant influence on the uniaxial stress on the specimen under axially-fixed and laterally-unconstraint conditions /ZHA 02/a/b/. This finding initiated an ideal to investigate influence of relative humidity change (or matric suction change) on the stress under the same conditions. In fact, change in matric suction leads to change in water content as well as thickness of interparticle water-films and hence change in the disjoining pressure or in the swelling pressure. The principle of the so-called uniaxial swelling pressure test is shown in Figure 2.17. A cylindrical specimen is placed in a cell and axially loaded to a desired level. After the loading, the axial strain is fixed. The specimen is re- and desaturated by circulating water vapour or dry air on its circumferential surface through the cell under laterally-unconstraint conditions. Due to hydration, clay minerals in the specimen may laterally expand and a swelling pressure may develop against the constraint axial boundary. And in contrast, the swelling pressure will be decreased by desaturation which causes a release of the adsorbed water. The test principle can also be applied for the determination of triaxial swelling stresses $(\sigma_1, \sigma_2, \sigma_3)$ under fixed boundary conditions.

The Callovo-Oxfordian specimen EST05547-07-II of 40 mm diameter and 80 mm length was tested in this regard. It had an initial water content of 7.1 % and a porosity of 17.8 %. Axial load was applied up to σ_1 = 15 MPa perpendicular to the bedding and resulted in an axial strain of 0.63 %. By fixing the axial strain, the axial stress dropped

down to about 13 MPa. Water vapour or dry air was pumped into the cell for re- and desaturation of the specimen. During the test, axial total stress or axial swelling pressure due to p_w = 0, temperature and relative humidity of air in the cell were measured, while the radial strain was unfortunately not recorded. Figure 2.18 shows the test procedure and the measurements.

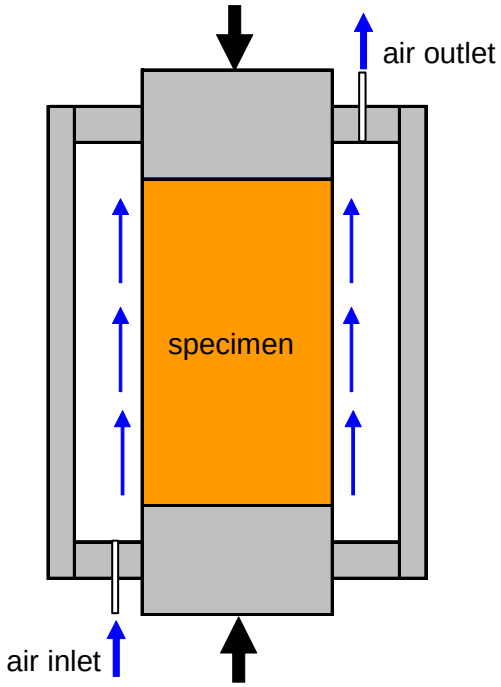

Figure 2.17 Schematic assembly of uniaxial swelling test

In the first phase (step I), water vapour was pumped into the cell to ensure full-saturation of the specimen. The axial stress varied with fluctuation in relative humidity of the air surrounding the specimen. When the air relative humidity was stabilized at 100 % over the last 2 days, the axial stress maintained constant at about 12 MPa.

In the second phase (II + III), dry air was pumped into the cell. The sudden reduction of the air relative humidity from 100 % to 29 % led to a rapid decrease in the axial stress from 12 to 3.7 MPa. From the sharp reduction it can be expected that the stress would fall down to zero when drying continued. Due to apparatus reasons, the dry air circulation was stopped. An equilibrium in humidity between the specimen and the cell air was then quickly achieved at about 75 %. During the equilibration, the stress increased to about 4.5 MPa and maintained constant.

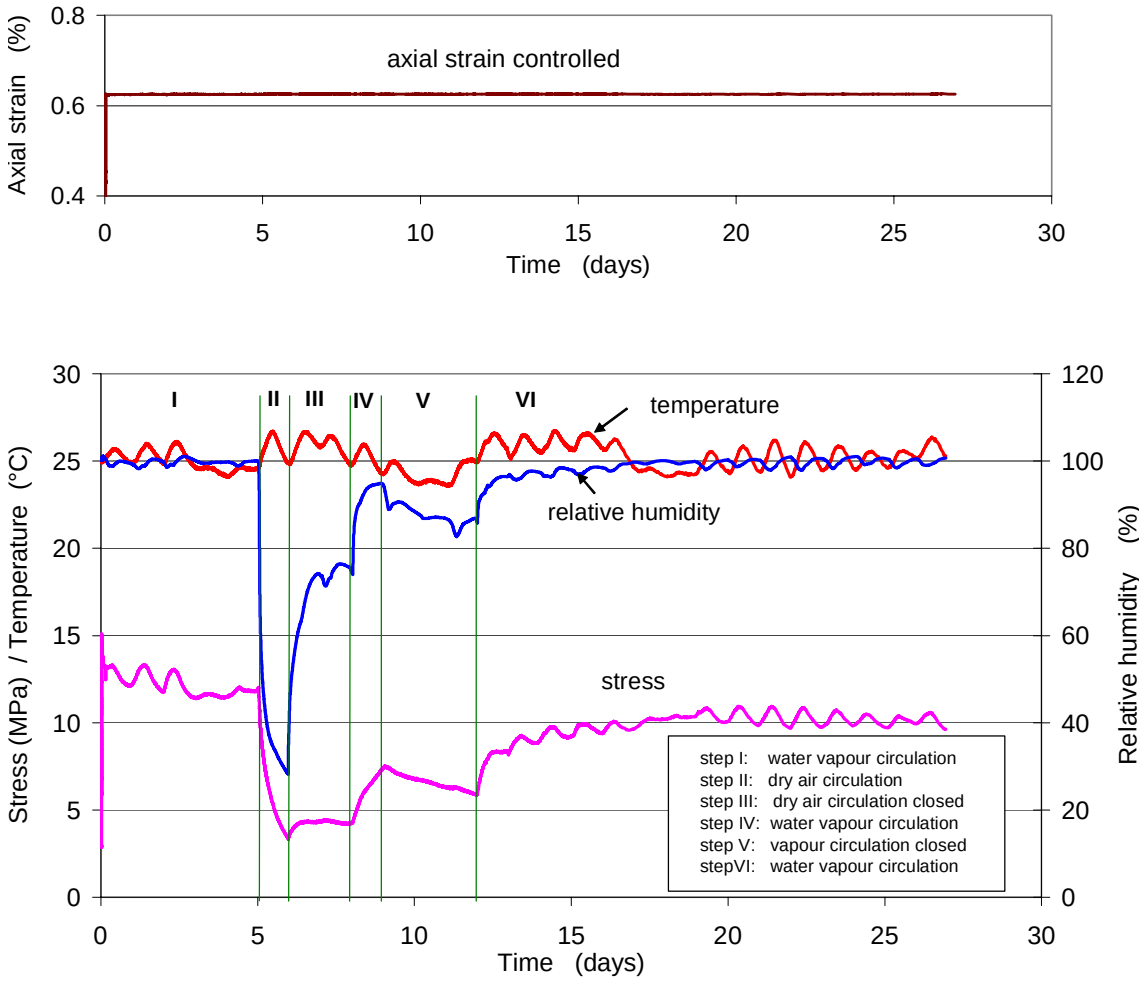

Figure 2.18 Measurements of temperature, relative humidity and axial stress during the uniaxial swelling pressure test EST05547-07

In the third phase (IV + V), water vapour was again pumped into the cell, resulting in an increase in relative humidity from 75 % to 93 %. Correspondingly, the axial stress raised from 4.5 to 7.3 MPa. After stopping the vapour circulation, a gradual reduction in relative humidity occurred. In correspondence to this, the stress decreased to 6.3 MPa as the relative humidity reached about 85 %.

In the final phase (VI), more vapour was pumped into the cell and circulated for 15 days, rising the relative humidity to 100 %. The increase in humidity resulted in an increase of the axial stress to 10 MPa, which maintained constant over the last 10 days. In correspondence to the periodic fluctuation of the temperature $\Delta T = \pm 1°C$, the relative humidity varied in the range of ± 1 %, generating a stress variation within ± 0.5 MPa.

Generally, the test shows very interesting phenomena:

- Uniaxial swelling pressure builds up in the argillaceous specimen under axially-fixed and laterally-unconstraint conditions due to the existence of interparticle water-films in it. Its magnitude is determined by the degree of water saturation and reaches the maximum when the material is fully saturated. When the water saturation is lower than a threshold degree of water saturation the swelling pressure disappears.
- The high swelling pressures of 10 to 12 MPa observed in nearly or fully saturated conditions are practically equal to the lithostatic stress at the sampling depth of 455 m (about 11 MPa).

These experimental observations clearly support Horseman's stress concept, i.e. the disjoining pressure in interparticle water films or the swelling pressure serves as effective stress in compact clays, equal to the lithostatic stress.

2.3.4 Uniaxial Swelling, Shrinkage and Creep

The build-up of uniaxial swelling pressure in the Callovo-Oxfordian argillite implies that uniaxial swelling strain can also occur in the argillite under uniaxial stresses. This aspect was examined on two Callovo-Oxfordian specimens. Figure 2.19 shows the results.

Specimens EST05582-02-II and EST05630-02-= were enclosed in jackets and axially loaded to 15 MPa. Under the constant load and environmental conditions (relative humidity, temperature), the axial compressive creep strain increased steadily with time. Exposing the specimens to the room air with low relative humidity of 15 % to 34 % resulted in desaturation. This led to a large uniaxial shrinkage or compaction of about 0.3 %, independent of the loading direction (EST05582-02-II perpendicular to the bedding and EST05630-02-= parallel to the bedding). The shrinkage is clearly caused by release of the adsorbed water-films. Under the external load, the desaturated pore spaces collapsed, creating new contacts between particles. The particle contacts might be solid to solid or through remaining water-films, depending on the degree of water saturation. The strain fluctuation during the drying period of 70 days corresponds to the moisture fluctuation, indicating the supporting activity of the water-films. After isolating

the specimens against the room air conditions, the strain fluctuation was minimised. However, the swelling strains could also be clearly observed.

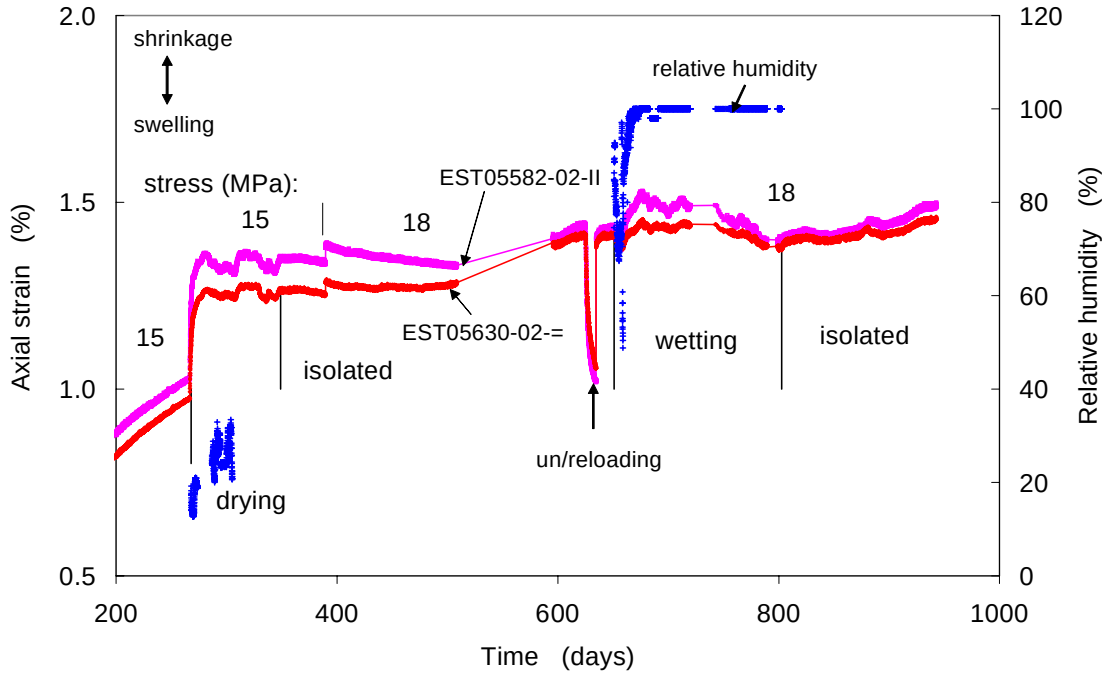

Figure 2.19 Uniaxial swelling, shrinkage and creep of Callovo-Oxfordian specimens EST05582-02 and EST05630-02

Sudden rising the axial load from 15 to 18 MPa resulted in small compressive strains of 0.03 % to 0.04 %, which were then recovered over 100 days by swelling effect. After reaching the maximum swelling strain, compressive creep occurred. Because data from 510 to 600 days were unfortunately lost due to a computer failure, the deformation process can not fully be given here. However, the data of the last 25 days before unloading clearly show compressive creep strains. After reloading to 18 MPa and stabilisation of the creep, water vapour was circulated through the annular spaces between specimens and jackets. The swelling and compressive creep occurred interactively at the beginning of the wetting phase. At 100 % relative humidity over the last 100 days, the swelling dominated. The following isolation prevented a water release. Under the constant load and environmental conditions, the compressive creep dominated.

Generally, the significant uniaxial swelling strains observed by resaturation under high axial stresses to 18 MPa reveal a high stress-supporting capability of interparticle

water-films and hence a large swelling capability of the Callovo-Oxfordian argillite. Even under isotopic confining stresses up to 20 MPa in other tests /GAS 00/, /LEB 00/, the Callovo-Oxfordian argillite immersed in water exhibits also swelling strains. If external stresses and environmental conditions are kept constant, the argillite exhibits compressive creep. Desaturation causes shrinkage or compaction depending on the load level and the degree of water saturation. These experimental observations clearly support Horseman's stress concept that interparticle water-films in compact clays carry the externally applied total stress when external water pressure is zero.

2.4 Thermo-Hydro-Mechanical Experiments

To gain a better understanding of the THM behaviour of indurated clays as host formation for HLW disposal, a preliminary experimental study of the THM behaviour of the Callovo-Oxfordian argillite and the Opalinus clay was performed. The programme included

- the development of adequate testing devices and methods,
- the conduction of hydro-mechanical and thermo-hydro-mechanical experiments.

2.4.1 Testing Devices

2.4.1.1 Oedometer

Two new oedometer cells were developed by GRS. Figure 2.20 shows the schematic setup and photos of the cell, which allows a normal specimen size of 50 mm diameter and 50 mm length. The oedometer cell was designed to be able to perform temperature-controlled and suction-controlled experiments on clays for the determination of:

- *Consolidation* by axial loading up to 25 MPa in drained and undrained conditions, and *shrinkage* due to change of water content (or suction) measured by 3 LVDT deformation transducers installed in the cell wall;
- *Swelling pressure* and *swelling strain* during hydration by supply of liquid water or water vapour under various loading conditions measured by a pressure sensor

directly embedded on the bottom and by a load sensor installed on the top loading piston and by 3 LVDT transducers;

- *Permeability* to water and to gas as a function of porosity and *two-phase-flow parameters* under suction-controlled conditions;
- *Pore pressure* induced by mechanical and thermal loading measured by two pressure transducers installed in both inlet and outlet lines;

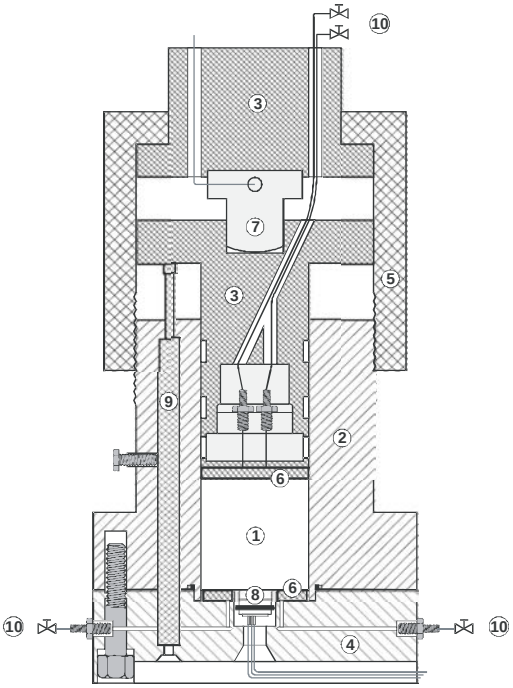

1. specimen
2. cell
3. load piston
4. bottom plate
5. screw cap
6. sintered porous disc
7. load transducer
8. pressure transducer
9. LVDT deformation transducer
10. inlet and outlet valves

Figure 2.20 Schematic setup and photos of the oedometer cell developed by GRS

- *Thermal effects* on the hydro-mechanical behaviour by changing temperature in a range between 20°C and 120°C under various conditions (drained or undrained, volume-constraint or constant load).

2.4.1.2 Triaxial Apparatus

One triaxial apparatus was modified for the conduction of THM experiments on clays. The apparatus comprises a triaxial cell designed for a maximum cell pressure of 40 MPa and a maximum axial load of 100 kN, a heating system for temperatures up to 200 °C, a hydraulic system for fluid supply up to 16 MPa, a data acquisition system and various instruments for measurement and control of stresses, strains, injection pressure of external fluid and temperature. Figure 2.21 shows schematically the assembly and the photo of the triaxial testing apparatus.

The triaxial cell allows installation of a normal cylindrical specimen of 50 mm diameter and 100 mm length. The axial force is measured by a load cell with an accuracy of ± 0.1 % of readings, and the lateral confining pressure is measured by a pressure transducer with an accuracy of ± 0.1 %. Axial deformation of the specimen is recorded by a LVDT deformation transducer with an accuracy higher than ± 0.1 %, which is mounted inside the cell between the upper and lower loading platen. A MTS-circumferential extensometer is mounted around the specimen outside the jacket at mid-height to determine lateral deformation within 1 % tolerance.

Specimen heating is accomplished using three independent electrical heaters. One is wire spiral positioned near the bottom in the cell, and the two others are inserted in the upper and lower platen, respectively. Cell temperature is measured and controlled by a temperature transducer PT100 installed near the specimen inside the cell.

Fluid is allowed to be injected into the stressed specimen through both upper and lower sintered porous discs. The fluid pressure is usually generated by gas pressure in a pressure vessel containing the fluid. Instead of this pressure generating system, a syringe pump MOD-260D generating a maximum pressure of 50 MPa with an accuracy of ± 0.5 % can be used for special desires. The inlet fluid pressure at the lower end face and the outlet fluid pressure at the upper end face are measured with two pressure transducers of an accuracy of ± 0.1 %. By using the hydraulic system it is also possible to measure permeability by means of burette or flow rate gages.

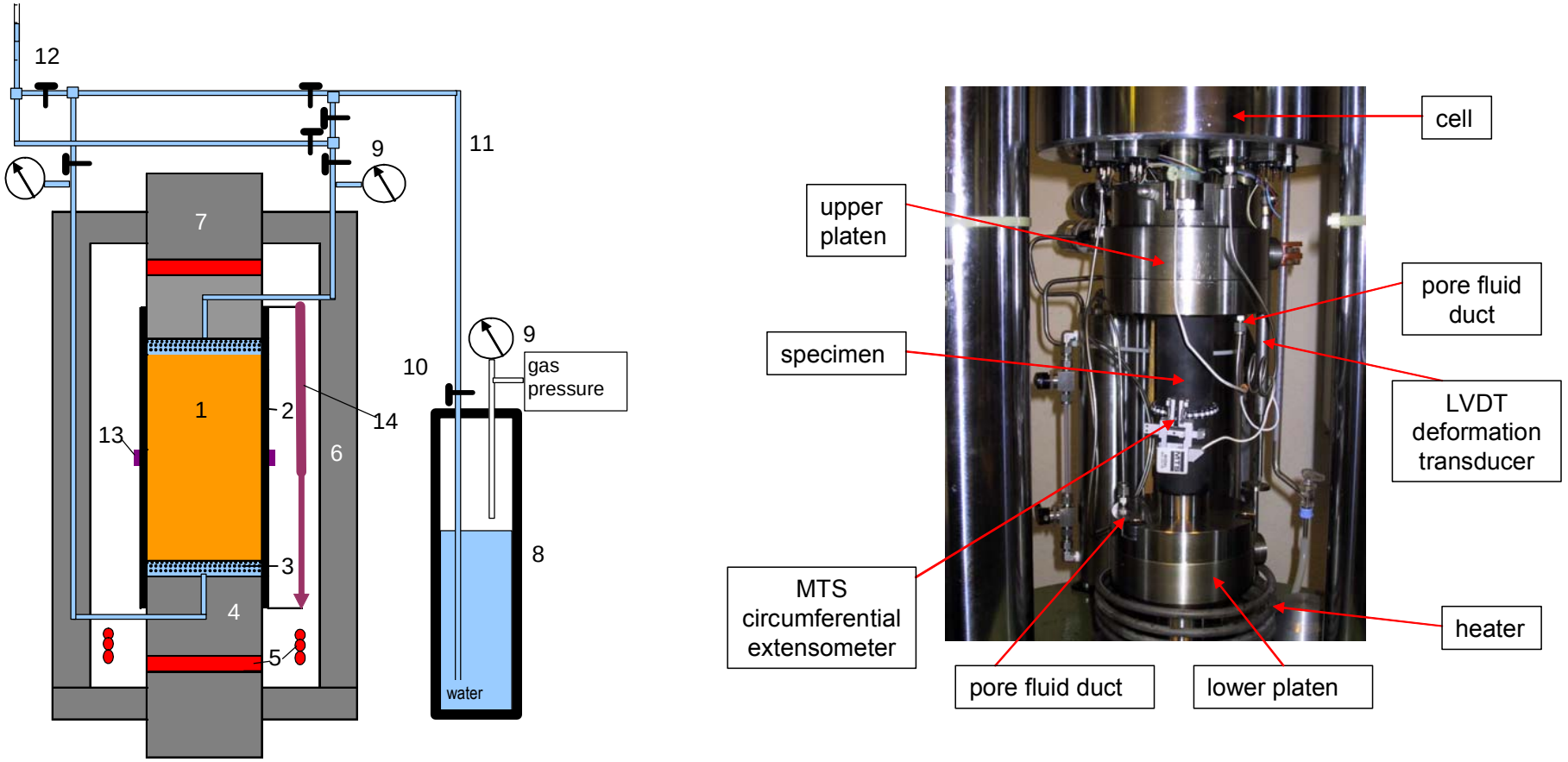

1: specimen 2: jacket 3: sintered porous disc 4: steel platen 5: heater 6: triaxial cell 7: load piston 8: fluid pressure vessel
9: pressure transducer 10: valve 11: pipe line 12: burette 13: MTS circumferential extensometer 14: LVDT deformation transducer

Figure 2.21 Schematic and photo of the modified triaxial apparatus at the GRS laboratory

2.4.2 Testing Procedure

Two Callovo-Oxfordian specimens EST05684-02-= and EST05490-01-= and one Opalinus specimen BVE1-03-= were tested in the triaxial apparatus to study the THM behaviour of the indurated clays. The specimens had a diameter of 50 mm and lengths of 85 to 100 mm. Their characteristics are given in Table 2.1. According to the calculated degrees of water saturation, both Callovo-Oxfordian specimens seemed to be initially saturated, while the Opalinus specimen was unsaturated.

Figure 2.22 shows thermo-hydro-mechanical loading conditions on a specimen. The specimen is triaxially loaded by axial stress σ_1 and radial stress $\sigma_2 = \sigma_3$, heated or cooled by changing temperature T, and subjected to external water pressures at the lower end face (inlet) p_{in} and the upper end face (outlet) p_{out}. It is to be noted that the local pressure acting in the interparticle water-film p_{fm} is the sum of the disjoining pressure Π_D and the (free) pore water pressure p_w.

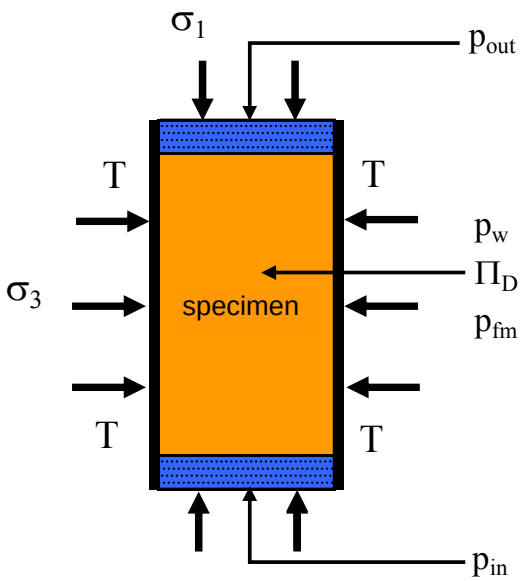

σ_1 = axial total stress

σ_3 = radial total stress

p_{in} = external water pressure in porous inlet reservoir

p_{out} = external water pressure in porous outlet reservoir

p_w = pressure of free pore water

Π_D = disjoining pressure in water-films

p_{fm} = pressure in interparticle water-films $p_{fm} = \Pi_D + p_w$

T = temperature

Figure 2.22 Thermo-hydro-mechanical loading conditions on a clay specimen

The tests were carried out in two stages: in the first stage, the HM behaviour of the specimens at ambient temperature was examined, and then in the second stage, thermal effects were investigated. In the tests, relevant *in situ* conditions of a HLW repository located deeper than 400 m (lithostatic pressure higher than 10 MPa, free pore water pressure being in equilibrium with external water reservoirs at a pressure higher than 4 MPa, and temperature up to 150 °C) were considered.

The following general testing procedure was used:

- *Saturation* under a constant isotropic total stress of 5 MPa by injecting clay formation water into the specimens at pressures of 3 - 4 MPa to ensure complete saturation,
- *Consolidation* by raising the axial and radial total stresses up to 12 - 20 MPa to examine the response of the pore water pressure,
- *Heating* by elevating the temperature up to 150 °C, and then
- *Cooling* by decreasing the temperature down to ambient condition to determine thermal effects on the hydro-mechanical behaviour.

The actual testing procedure in each test was more or less differing from the general procedure for investigating some specific aspects. Results of the tests are presented below regarding the hydro-mechanical behaviour and thermal effects.

2.4.3 Results of Hydro-Mechanical Tests

Test EST05684-02

On the Callovo-Oxfordian specimen EST05684-02-=, only the hydro-mechanical test was carried out at ambient temperature. Figure 2.23 shows the measurements of temperature, axial and radial stresses, inlet and outlet water pressures, axial, radial and volumetric strains during the test. The uncontrolled temperature in the cell varied in a relatively large range from 26 °C to 37 °C during the test period of 52 days.

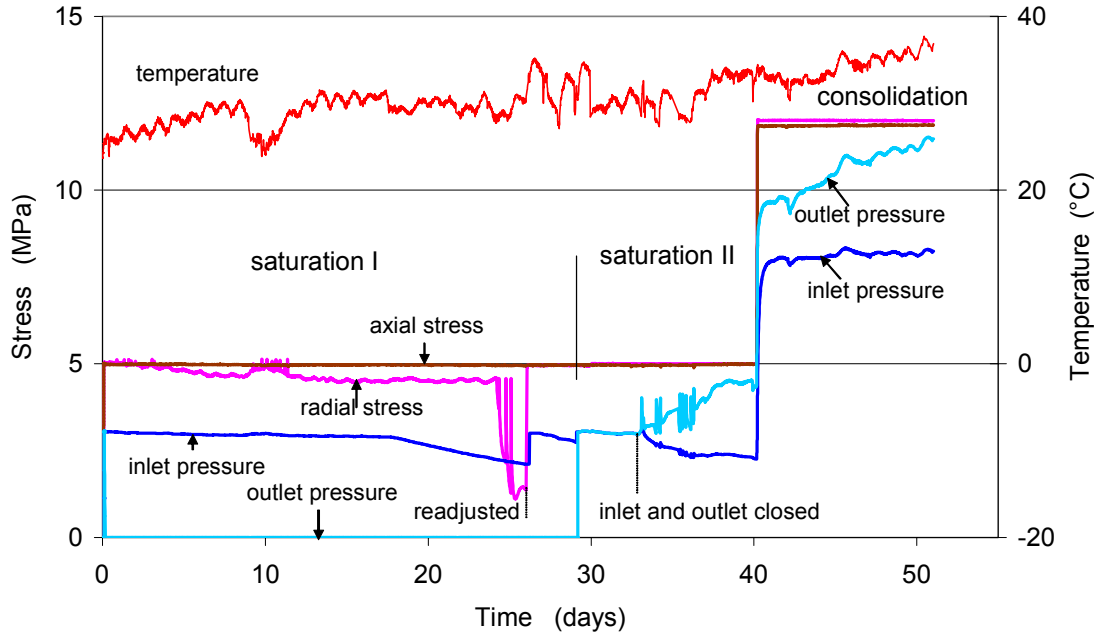

a. Evolution of temperature, axial and radial stress, inlet and outlet water pressure

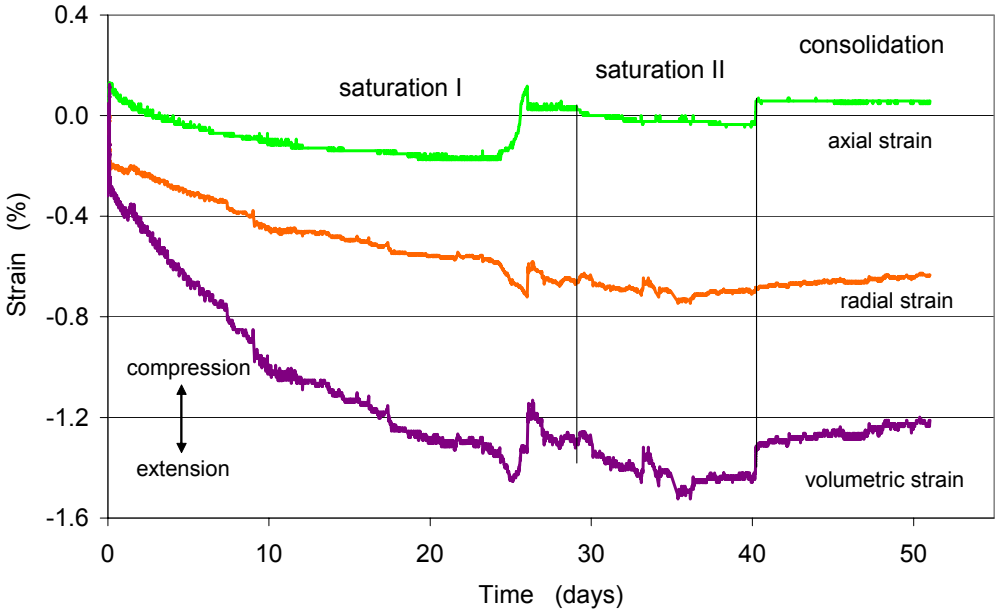

b. Evolution of axial, radial and volumetric strain

Figure 2.23 Results of the HM test on Callovo-Oxfordian specimen EST05684-02

Saturation

First, the specimen was loaded by increasing the axial stress σ_1 and the radial stress σ_3 at open inlet and outlet, i.e. in drained conditions at $p_{in} = p_{out} = 0$. Because the axial loading rate was somewhat higher than the radial loading rate, the resulting stress difference $(\sigma_1 - \sigma_3)$ ≈ 1 MPa generated an axial compression of ε_1 = 0.1 %, a radial extension of ε_3 = -0.2 %, and a volumetric expansion of ε_v = -0.3 % as well. An isotropic total stress of $\sigma_1 = \sigma_2 = \sigma_3$ = 5 MPa was then adjusted.

Phase I: Under the applied mechanical conditions, the clay water prepared by mixing distilled water with the clay powder was injected to the inlet and outlet end faces of the specimen by increasing the pressures to $p_{in} = p_{out}$ = 3 MPa. After that, the outlet pressure was reduced to zero and then outlet was closed. During saturation phase I of 29 days, the specimen was gradually expanded. Uncontrolled sudden drops of the radial stress from 4.4 MPa to 1.2 MPa and a gradual decrease of the inlet pressure down to 2.4 MPa caused a significant axial compression and radial extension. Readjusting of the radial stress to the initial value of 5 MPa and the inlet pressure to 3 MPa produced a small sudden axial extension and radial compression. On the other hand, it is clearly to be seen that the applied inlet pressure did not generate any response of the water pressure in the closed outlet reservoir. This might indicate that the specimen is impermeable for advective water flow at a pressure of 3 MPa, because this pressure might be too low to overcome the local pressures in the water-films which are probably equal to the externally applied total stress of 5 MPa.

Phase II: Both inlet and outlet water pressures were increased to 3 MPa and 5 days later, both inlet and outlet valves were closed. Under the constant external stresses and undrained conditions, both inlet and outlet water pressures behaved differently. The inlet pressure decreased to 2.3 MPa in 7 days, while the outlet pressure increased to 4.4 MPa. The decrease of the inlet pressure indicates that the specimen at the inlet side might be not fully saturated, whereas the increase of the outlet pressure might be caused by expelling of some free pore water from the outlet part of the specimen.

Consolidation

After stabilisation of the external water pressures, the axial and radial stresses were simultaneously raised to 12 MPa and then held constant. The sudden increases of the

external stresses compacted the specimen and generated rapid increases in both inlet and outlet water pressure to 8 and 9.5 MPa, respectively. Under the constant external stresses, the inlet pressure maintained almost unchanged while the outlet pressure rose steadily to a 11.2 MPa in 14 days and tended to the external stress of 12 MPa. The different responses of both external water reservoirs to the compression imply that there existed no hydraulic interconnection through the specimen. The highly pressured interparticle water-films in the compact argillite may act as barriers against advective water flow.

Assuming that the inlet and outlet water pressures represent the free pore water pressures in the lower and upper parts of the specimen, Skempton's pore pressure coefficient B = $\Delta p_w / \Delta\sigma$ can be determined from the undrained compression results: B = 84 % by $\Delta\sigma$ = 12 – 5 = 7 MPa and Δp_{in} = 8.2 – 2.3 = 5.9 MPa for the lower part of the specimen, and B = 97 % by Δp_{out} = 11.2 - 4.4 = 6.8 MPa for its upper part. The B-values less than 1 indicate that the specimen was not fully saturated.

Test EST05490-01

Figure 2.24 shows the results of the HM test on the Callovo-Oxfordian specimen EST05490-01-=. The temperature in the cell varied between 31 °C and 41 °C during the test period of 50 days.

Saturation

The specimen was isotropically compressed to $\sigma_1 = \sigma_3$ = 5 MPa at open inlet and outlet ($p_{in} = p_{out} = 0$). This resulted in compressive strains with ε_1 = 0.01 %, ε_3 = 0.02 %, and ε_v = 0.05 %. After the loading, the axial strain was fixed ($\Delta\varepsilon_1 = 0$) and the inlet water pressure was raised to 3 MPa while the outlet water reservoir was closed. The increment of the inlet water pressure resulted in a similar increase of the axial stress ($\Delta\sigma_1 \approx \Delta p_{in}$). Due to the temperature fluctuation, the axial stress varied between 7.6 and 10.0 MPa during the saturation phase of 38 days. This was mainly caused by thermal expansion and extraction of the pore water. After opening the outlet valve, the thermally-induced increment of the axial stress caused a drained compaction from ε_v = 0.05 % to 0.17 % over 21 days. At 39 days, sudden reduction of the inlet water pressure from 3 MPa down to zero generated a similar drop of the axial stress.

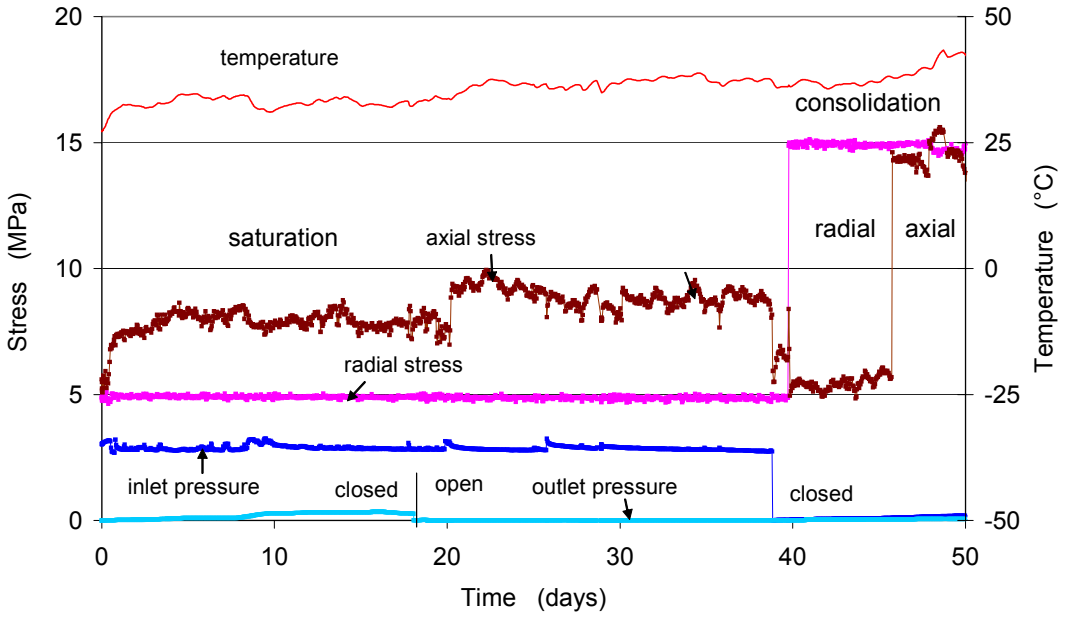

a. Evolution of temperature, axial and radial stress, inlet and outlet water pressure

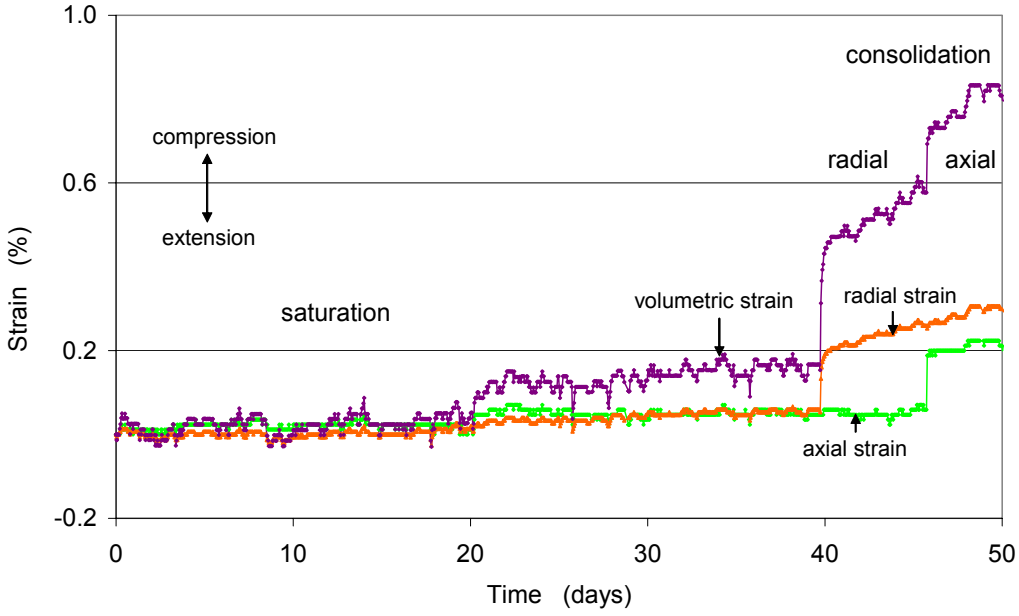

b. Evolution of axial, radial and volumetric strain

Figure 2.24 Results of the HM test on Callovo-Oxfordian specimen EST05490-01

Consolidation

After closing both inlet and outlet valves, increasing radial stress from 5 to 15 MPa generated a radial compression from 0.06 % to 0.19 % and a volumetric compaction from 0.17 % 50 0.6 % over 5 days. At constant radial stress, the axial stress was increased to σ_1 = 14.6 MPa. Correspondingly, the axial compressive strain increased from 0.06 % to 0.2 % and the volumetric compaction increased from 0.6 % to 0.8 %. However, both radial and axial compression did not produce significant changes of water pressures in the closed external reservoirs. This implies that the specimen was probably not fully saturated.

Test BVE1-03

Figure 2.25 shows the results of the HM test on the Opalinus specimen BVE1-03-=. The temperature in the cell varied between 29 °C and 37°C during the test period of 16 days.

Saturation

The specimen was isotropically compressed to $\sigma_1 = \sigma_3$ = 5 MPa at open inlet and outlet ($p_{in} = p_{out}$ = 0) resulting in significant compressive strains of ε_1 = 0.11 %, ε_3 = 0.46 %, and ε_v = 1.03 %. Synthetic Opalinus clay solution was then injected to the stressed specimen at an inlet pressure of p_{in} = 5 MPa and an outlet pressure of p_{out} = 2 MPa. Whereas the outlet pressure was reduced to zero again and the outlet reservoir was immediately closed, the inlet pressure was reduced to 4 MPa and maintained constant. The water injection resulted in a gradual expansion to the original volume over 8 days. During the water injection phase, no change in the outlet water pressure was observed. The following increase in the outlet water pressure to 4 MPa caused a further expansion to $\Delta\varepsilon_v$ = 0.65 % over 2 days. The mechanical responses to the sudden changes in external water pressures are delayed due to a very low hydraulic conductivity of the material.

Consolidation

After closing both inlet and outlet valves, the axial and radial stresses were raised to σ_1 = 13 MPa and σ_3 = 12.3 MPa. Correspondingly, both inlet and outlet water

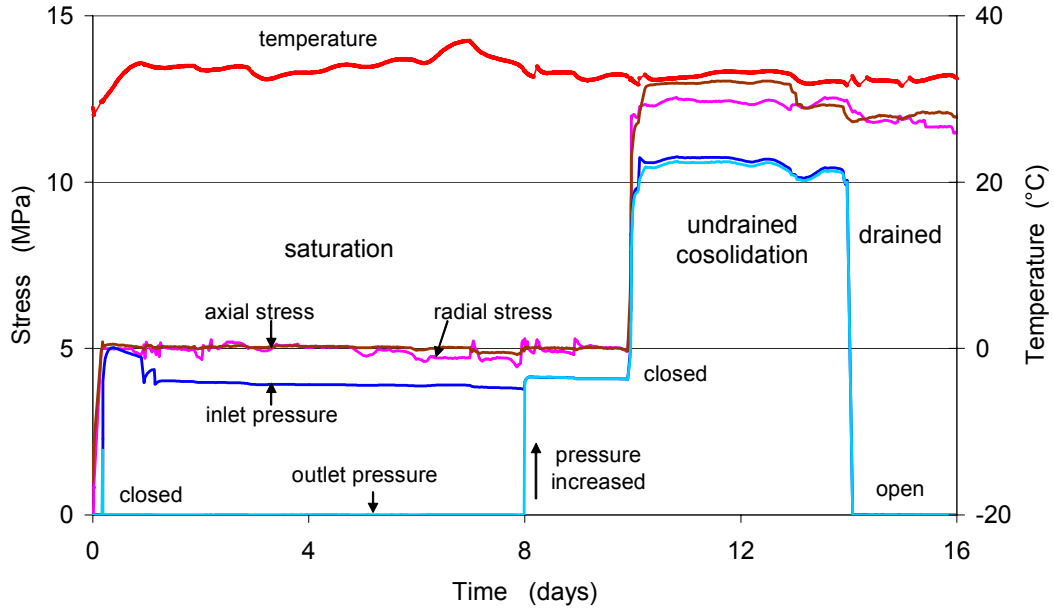

a. Evolution of temperature, axial and radial stress, inlet and outlet water pressure

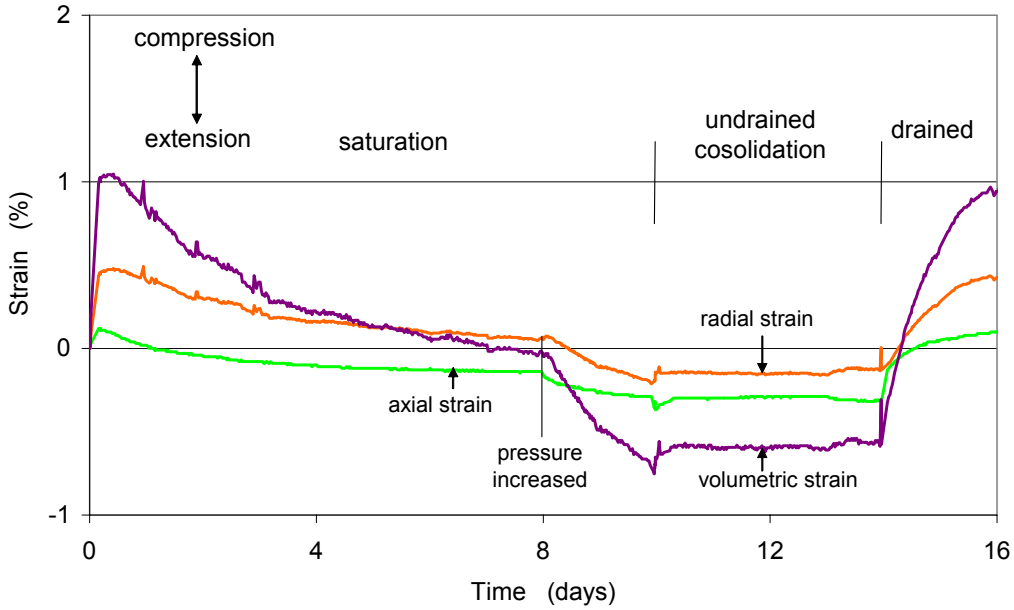

b. Evolution of axial, radial and volumetric strain

Figure 2.25 Results of the HM test on Opalinus clay specimen BVE1-03

pressure rose simultaneously to $p_{in} = p_{out}$ = 10.7 MPa. The same behaviour of both external water reservoirs indicates that there existed hydraulic pathways through the specimen to the external reservoirs. The unity value of the inlet and outlet pressures represents the free pore water pressure in the specimen of $p_w = p_{in} = p_{out}$ = 10.7 MPa. From the undrained consolidation results, Skempton's pore pressure coefficient can be determined by B = 6.7 / 7.5 = 89 %, indicating unsaturation of the specimen. Additionally, it can also be seen that the changes of the external water pressures in equilibrium with the pore water were exactly correlated with the uncontrolled change of the applied external stresses. The following sudden opening of both inlet and outlet valves produced a drained condition ($p_{in} = p_{out} = 0$) and resulted in a significant increase of the effective stress from σ_{eff} = 12.5 - 10.7 = 1.8 MPa to 12.5 MPa. The high effective stress compacted the specimen by $\Delta\varepsilon_v$ = 1.52 % over 2 days.

2.4.4 Results of Thermo-Hydro-Mechanical Tests

Test EST05490-01

After the hydro-mechanical experiment (Figure 2.24), the Callovo-Oxfordian specimen EST05490-01-= was tested subsequently to examine thermal effects by heating and cooling. Figure 2.26 shows the measurements of temperature, axial and radial stresses, inlet and outlet water pressures, axial, radial and volumetric strains during the THM test.

Consolidation

The specimen was loaded to an axial stress of σ_1 = 20 MPa and an radial stress of σ_3 = 18 MPa. The loads resulted in compressive strains of ε_1 = 0.21 % to 0.38 %, ε_3 = 0.31 % to 0.34 % and ε_v = 0.83 % to 1.06 %. However, the high external stresses generated only very insignificant increments of both external water pressures of 0.5 and 1.0 MPa, respectively.

Heating

Under σ_1 = 20 MPa and σ_3 = 18 MPa and undraind conditions, the specimen was heated by rapidly elevating temperature from 32 °C to 91 °C, which then remained

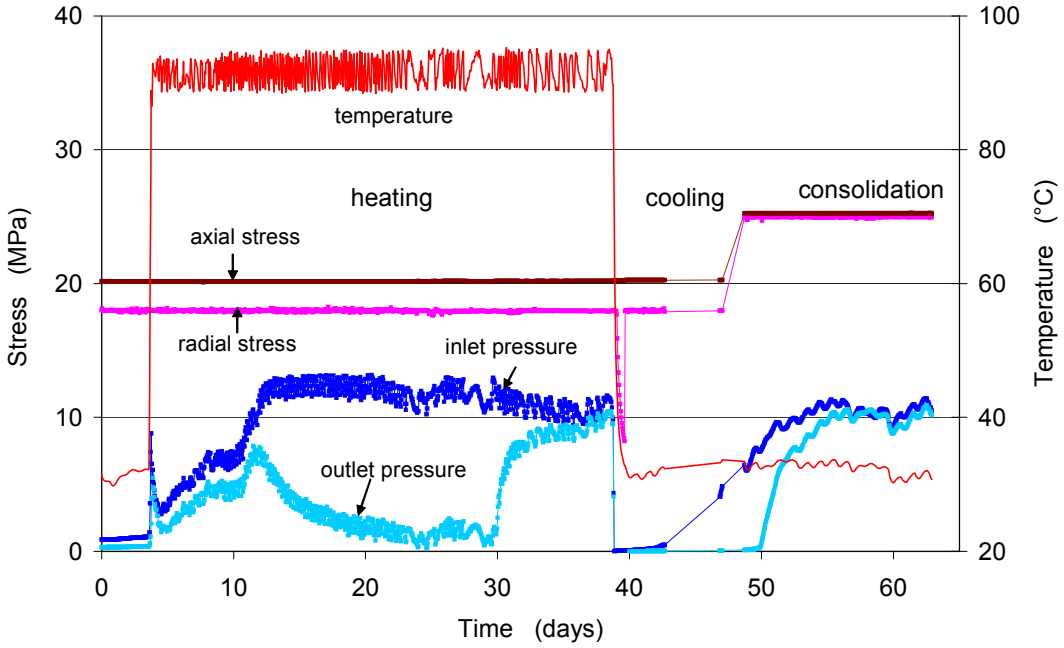

a. Evolution of temperature, axial and radial stress, inlet and outlet water pressure

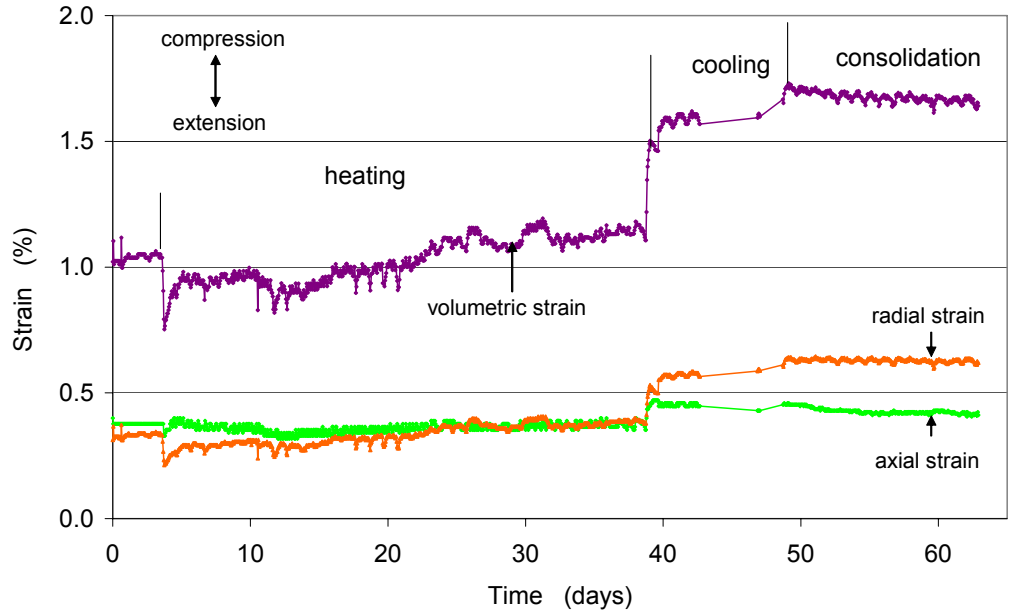

b. Evolution of axial, radial and volumetric strain

Figure 2.26 Results of the THM test on Callovo-Oxfordian specimen EST05490-01

constant within a tolerance of ± 2 °C. The sudden heating generated high impulses of the inlet and outlet water pressures to 6 and 8 MPa. The pressure dissipated then quickly down to 2.6 and 1.6 MPa and subsequently rose gradually to 12.5 and 7.8 MPa, respectively. Whereas the inlet pressure maintained almost constant, the outlet pressure dropped then gradually down to zero. The reduction of the outlet pressure indicates that the outlet part of the specimen was not fully saturated. At the high temperature, the adsorbed water might become free and move out of the interparticle films by the effect of pressure gradient. Consequently, both external water reservoirs would be interconnected through the thermally-desorbed pore water in the specimen. And finally, an equilibrium between both external water reservoirs was reached at a pressure of 10.5 MPa. This value might represent the free pore water pressure under the not fully-saturated conditions, while the maximum pressure of 12.5 MPa measured in the inlet reservoir might be close to the free pore water pressure of the specimen in saturated conditions.

Additionally, the sudden heating caused also a rapid thermal expansion of $\Delta\varepsilon_1$ = -0.05 %, $\Delta\varepsilon_3$ = -0.1 % and $\Delta\varepsilon_v$ = -0.3 %. During the heating phase, the specimen was laterally compressed while the axial strain was relatively unchanged. The thermal consolidation was probably caused by collapse of some unsaturated pores. When the equilibrium between the external waters and the pore water was reached, the strains maintained almost constant.

Cooling

After stabilisation of the THM processes during the heating phase, the temperature was rapidly reduced to 31 °C. Correspondingly, the inlet and outlet water pressure fell simultaneously down to zero due to contraction of the pore water and the external waters. Because the loading system was not well regulated, the radial stress dropped down to 8 MPa. Consequently, the specimen was largely compacted by $\Delta\varepsilon_1$ = 0.11 %, $\Delta\varepsilon_3$ = 0.14 % and $\Delta\varepsilon_v$ = 0.42 %. After readjusting of the radial stress to 18 MPa, the strains were almost unchanged over the further cooling phase. However, the external water pressures in both reservoirs behaved differently. The inlet pressure increased to 4.8 MPa over 7 days, while the outlet pressure maintained at zero. The different external water pressures might indicate that the prior thermally-desorbed pore water at the high temperature was more or less adsorbed again on the mineral surfaces at the

low temperature, forming interparticle films as barriers separating both external water reservoirs.

Consolidation

In the last stage, the external stresses were increased to 25.2 MPa, causing a compaction of about 0.1 %. Under the constant stresses, the external water pressures increased gradually to an unity value of about 10.5 MPa. If the specimen had been initially saturated, a higher pore water pressure could have been expected.

Test BVE1-03

After the HM experiment (Figure 2.25), the Opalinus specimen BVE1-03-= was tested to investigate hydro-mechanical responses to heating and cooling. The THM test was carried out in 3 phases: 1) isotropic compaction to 15 MPa at 25°C, 2) multi-step heating to 150°C at 15 MPa, and 3) cooling down to 30°C at 15 MPa. Figure 2.27 shows the test results.

Consolidation

The specimen was loaded to an isotropic stress of 5 MPa and subjected to 3.2 MPa external water pressures at both end faces for 3 days. After closing the inlet and outlet valves, the external isotropic stress was rapidly increased up to 15 MPa and then maintained constant. The sudden compaction increased the inlet and outlet pressure to 10.5 and 12.7 MPa, respectively. Under the constant external stresses, the inlet pressure increased from the lower level whereas the outlet pressure decreased from the higher level. Finally, both pressures tended to an equilibrium at an unity value of 12.2 MPa. This unity value represents the pore water pressure in the specimen. From this, the Skempton's coefficient B = 90 % can be determined, indicating unsaturation of the specimen.

On the other hand, the specimen was compacted by the externally applied stresses even under undrained conditions. At the end of the consolidation phase, the inlet and outlet valves were shortly opened, and the water pressures dissipated to zero. The reduction of the external water pressure and the pore water pressure under the constant total stress resulted in a significant increase in effective stress from 2.8 to 15 MPa, under which the specimen was compacted from ε_v = 1.27 % to 4.41 %.

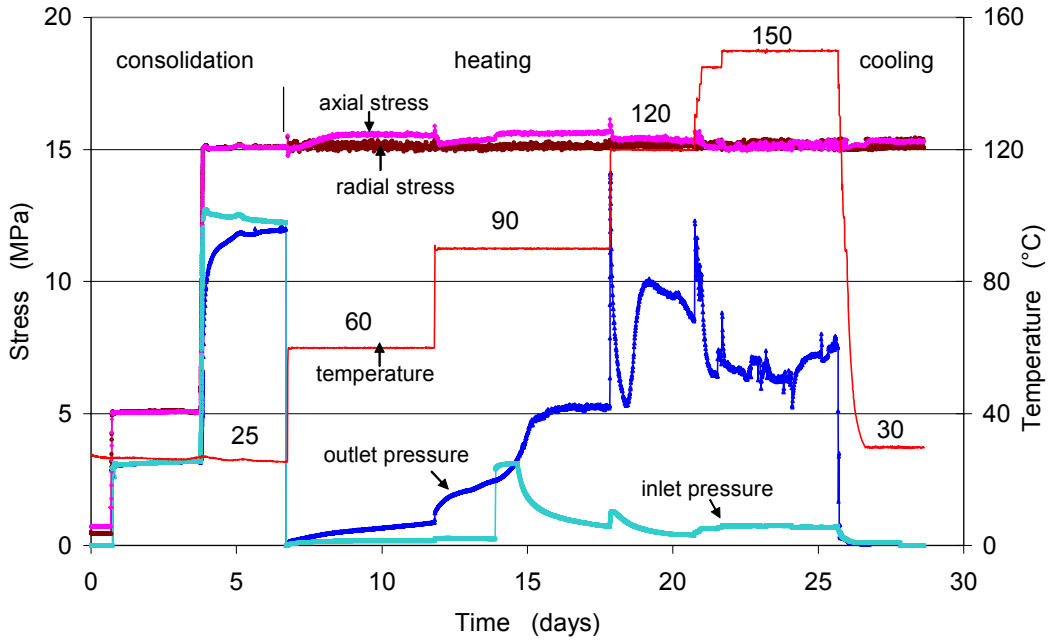

a. Evolution of temperature, axial and radial stress, inlet and outlet water pressure

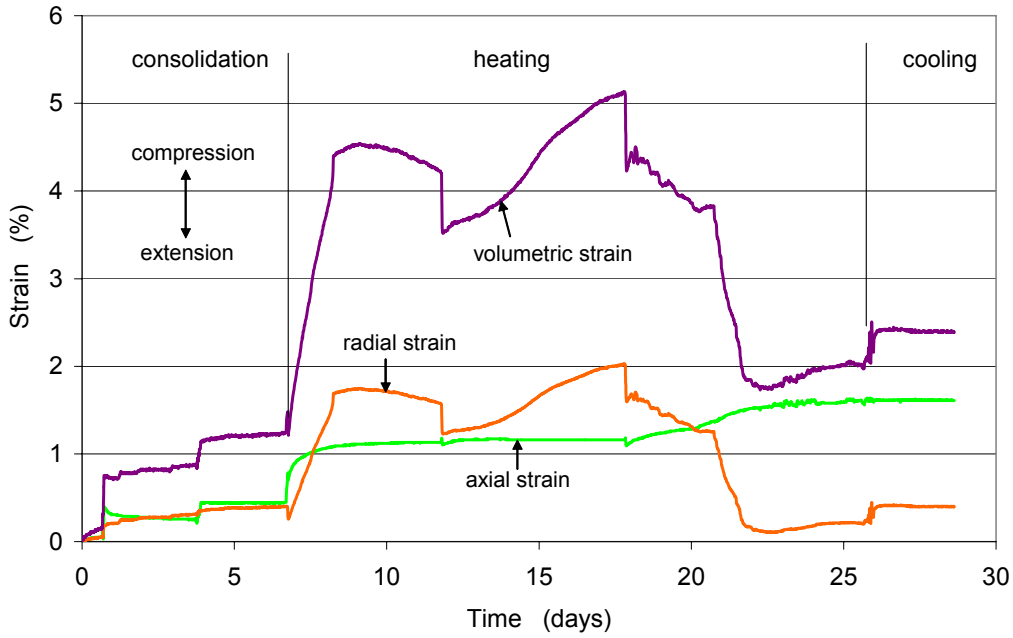

b. Evolution of axial, radial and volumetric strain

Figure 2.27 Results of the THM test on Opalinus clay specimen BVE1-03

Heating

After switching off the inlet and outlet valves again, the specimen was heated by elevating temperature from 25 °C to 60 °C, 90 °C, 120 °C and 150 °C. Each heating phase lasted for 2 to 5 days. After improvement of the temperature regulating system, a high precision of ± 0.1 °C was reached.

T = 25 → 60 °C: The temperature increment generated a gradual increase of the outlet water pressure to 1 MPa, but the inlet pressure remained at zero. During the heating phase, the specimen expanded gradually from ε_v = 4.5 % to 4.2 %.

T = 60 → 90 °C: This temperature elevation caused a further increase of the outlet pressure, while the inlet pressure was almost unchanged. To check if there existed leakage in the inlet water reservoir, the inlet water pressure was raised to 3 MPa and then closed. As the outlet pressure reached the maximum of 5.3 MPa, the inlet pressure fell down to 1 MPa. This clearly confirms the existence of leakage in the inlet water reservoir. This leakage produced practically a drained condition. On the other hand, the sudden heating caused a radial and volumetric expansion of $\Delta\varepsilon_3$ = - 0.4 % and $\Delta\varepsilon_v$ = - 0.8 %, while the axial strain was unchanged. Due to the partly-drained condition in the inlet reservoir, the specimen was significantly consolidated.

T = 90 → 120 °C: This temperature rise produced a high impulse of the outlet water pressure to 14 MPa close to the external stress of 15 MPa. The peak pressure dissipated quickly down to the initial state and then rose again to 10 MPa. Due to the partly-drained condition in the inlet reservoir, the maximum water pressure in the outlet reservoir could not be maintained, but decreased gradually. Although under the partly-drained condition, the heating phase caused also a significant volumetric expansion from ε_v = 5.1 % to 3.8 %.

T = 120 → 150 °C: This temperature rise was performed by short multi-steps to 130 °C, 135 °C, 140 °C, 145 °C and 150 °C over one day. The small temperature increments resulted in small impulses of the outlet water pressure. After reaching the peak value of 12.3 MPa at 130 °C, further temperature increments did not generate any high water pressures. At 150 °C, the outlet water pressure varied between 5.5 and 8.5 MPa, while the inlet water pressure increased slightly to 0.75 MPa and maintained constant. A large thermal expansion from $\Delta\varepsilon_v$ = 3.8 % to 1.8 % occurred at the beginning of the

heating phase. After that, the specimen was compacted mainly due to the release of the pore water.

Cooling

In the last stage, the specimen was cooled by reducing temperature from 150 °C to 30 °C over one day. In correspondence to the cooling, the pore water pressure dropped quickly down to zero. This increased the effective stress and caused a compaction. After these sudden changes, the THM processes were rapidly stabilized.

2.4.5 Discussions and Conclusions

From the preliminary THM experiments on the Callovo-Oxfordian argillite and the Opalinus clay, very complex coupled thermo-hydro-mechanical phenomena were observed.

Effects of external stress on the hydraulic behaviour

Under undrained conditions, application of an external stress to the clays results in an increase in pore water pressure. The increments of the pore water pressure observed on the Collovo-Oxfordian and Opalinus specimens are close to the increments of the applied external stresses with the Skempton's coefficient B = $\Delta p_w / \Delta \sigma$ = 84 % to 97 %, indicating unsaturation of the specimens. The different pressure responses of both separated water reservoirs to the applied external stresses on the specimens imply that there are practically no hydraulic pathways through the intact clays for advective water flow. The adsorbed water-films act in fact as barriers against advective water flow.

Effects of external water pressure on the mechanical behaviour

Application of an external water pressure to the indurated clays increases the pore water pressure and hence reduces the effective stress under a constant total stress. The reduction of the effective stress causes a volumetric expansion of the material. Under isotropic total stress of 5 MPa and 3 to 4 MPa water injection pressures, a volumetric expansion of about 1.0 % was measured on the Callovo-Oxfordian and Opalinus specimens over days and weeks. In contrast to that, it is also observed on the Opalinus specimen that under total stresses of 12.5 to 15 MPa and drained conditions, reduction of the pore water pressures from 10.5 MPa and 12.2 MPa down to zero

causes significant compactions of 1.5 % and 3.2 %, respectively. Another interesting observation is that at fixed axial strain, application of an external water pressure produces a similar increment of the axial total stress. During the saturation phase, in which the external water pressures of 3 to 4 MPa were applied to one end face of the specimen under the total stress of 5 MPa, no pressure response in the other closed reservoir was recognised over more than one month. These observations may suggest that the indurated clays are probably impermeable for advective water flow until the external water pressure is raised to the disjoining pressure in the interparticle water-films or the effective stress in the clays.

Thermal effects on the hydro-mechanical behaviour

Difference in thermal expansion between pore water and solid particles in a saturated clay is the driving force in case of heating. Because the very low hydraulic conductivity of the clays does not allow the thermally-desorbed pore water so fast to disperse, heating results in an increase in pore water pressure which reaches the maximum under fully-saturated and undrained conditions. Under the external stress of 18.8 MPa and undrained conditions, a maximum pore water pressure of 12.5 MPa was observed by heating the Callovo-Oxfordian specimen from 32 to 91 °C. Under the external stress of 15 MPa and partly drained conditions, heating the Opalinus specimen from 25 to 120 °C caused the pore water pressure to rise up to 10 MPa. Additionally, increasing temperature results in expansion of the clays under undrained conditions. Even under high external stresses up to 15 MPa and partly-drained conditions, significant thermal expansions were also observed by heating the Opalinus specimen from 25 to 60, 90, 120 and 150 °C. However, under unsaturated and drained conditions, volumetric reduction of the clays was observed due to release of the pore water and collapse of unsaturated pores during the heating phases. In contrast to heating, cooling causes contraction of the pore water and reduces the pore water pressure. Correspondingly, the effective stress under a constant external stress is increased. Consequently, the clays can be compacted if drained conditions prevail. Under undrained conditions, the consolidation is negligible.

It is to be pointed out that the reported results are very preliminary but very interesting. The above discussions and conclusions are more qualitative. Mechanisms dominating the THM behaviour of the indurated clays are not very clear. Therefore, further theoretical studies and precise experiments are considered extremely important and necessary.

3 Geochemical Experiments

3.1 Diffusion of Cs+, I-, and SeO42- in the Callovo-Oxfordian Argillite

3.1.1 Introduction

In the event of water intrusion to the near field of an underground repository for radioactive waste it cannot be excluded that eventually, after corrosion of the waste containment and leaching of the waste matrix, radionuclides are released. Within the framework of a long-term safety assessment of the repository system the transport of radionuclides through the geologic barrier to the aquifer must be accounted for. Transport may occur principally through inhomogeneities (e. g. fissures or cracks) in the host rock or through the homogeneous matrix itself, predominantly by diffusion. This work deals with the investigation of diffusion through indurated clay as it is encountered in the MHM underground research laboratory at Bure.

Under the condition of a constant gradient of concentration in time, diffusion may be described by the Fick's First Law:

$$\frac{\partial N}{A \partial t} = -D \frac{\partial N}{\partial z} \tag{3.1}$$

where N is the number of particles which pass through a plane of area A within the unit of time t. The velocity of diffusion is dependent of the gradient in concentration, i.e. the change of the particle number within a distance z, and a constant of proportionality, the so called diffusion coefficient D. The flux of particles in the above equation is given in the unit of mol / m^2 s. Hence the unit for D is m^2/s. The diffusion coefficient is specific for the given conditions of temperature and solution composition in the pores of the clay. It is further specific for the diffusing particle and, via its gradient, the concentration. Last not least, D is specific for the clay itself.

It may therefore be concluded that, for a reliable measurement to perform, it is essential to ensure isothermal conditions, a properly characterized specimen of clay in terms of A and ∂z, and that the specimen investigated is in true equilibrium with the background solution in its pores, in which the particles are meant to diffuse. Due to

unavoidable inhomogeneities between various samples drawn from the host rock, it is further advisable to repeat a diffusion experiment for a number of times.

At the time, when this project was begun, there was no method available in the GRS to perform diffusion experiments with solution-saturated clays. It was therefore not the objective to corroborate measured diffusion data by the repetition of experiments, but rather, as a first step, to install a simple and low-cost prototype diffusion cell and to check its performance with a specimen of the Callovo-Oxfordian argillite.

3.1.2 Materials and Methods

A core of the Callovo-Oxfordian argillite with a diameter of 4,21 cm was submerged in liquid synthetic resin („Aralgit"). After hardening of the resin, a slice with a thickness of 1 cm was cut from the core, hereafter called „sample". The sample was placed in the diffusion cell assembled for this study. It is shown in Figures 3.1 and 3.2.

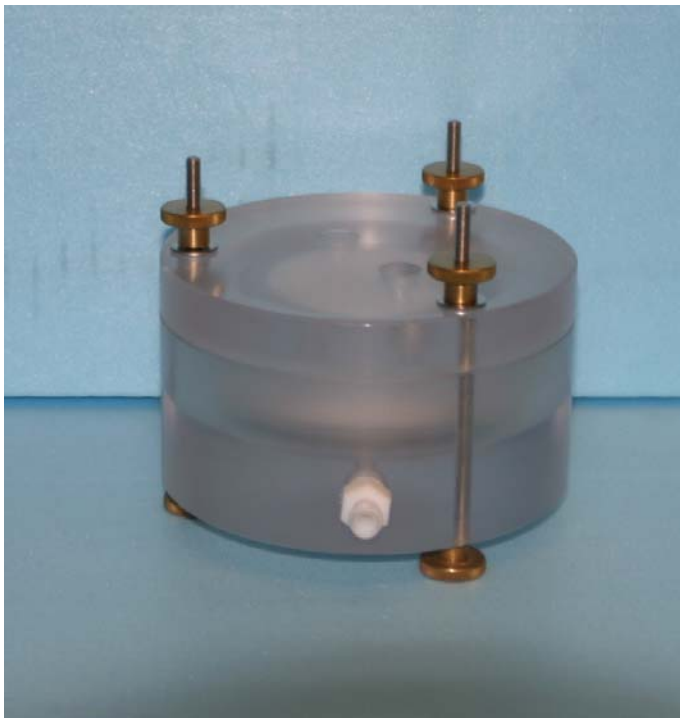

Figure 3.1 Diffusion cell

Figure 3.2 Diffusion cell disassembled. The clay closes up with the glass frits. The rubber rings have contact to the ring of synthetic resin which surrounds the clay. Their tightness was checked prior to the experiment.

The diffusion cell consists of two parts, the „lower part", and the „upper part". It was made of plexiglass The clay inside the cell is covered on both sides by glass frittes. Above and below the glass frittes solution is distributed or collected via interconnected grooves cut into the material.

Before the beginning the dry sample was placed in the diffusion cell. Unspiked solution was circulated through the lower part and the diffusion cell let in an unpright position. In this phase of the experiment entrapped gas was allowed to excape. Every week the diffusion cell was opened and the electrical conductivity of the upper surface measured. After one month electrical conductivity had increased.

In the second phase of experiment unspiked solution was circulated at both sides of the sample for app. two months. After this time the sample was assumed to be in equilibrium with the solution.

At the beginning of the third phase of the experiment, the solution for the lower part of the diffusion cell was replaced by an identical but spiked solution. The concentrations

were $1 \cdot 10^{-5}$ M (I^-, Cs^+) and $0.5 \cdot 10^{-5}$ M (SeO_4^{2-}). The upper part was continously supplied with unspiked solution.

In operation, a peristaltic pump delivered solution both through the lower and the upper part of the diffusion cell. The total volume of solution circulated through the lower part was chosen such, that the decrease of total concentration of the diffusing ions was negligibly small throughout the experiment. The solution passing through the upper part was collected in small glass vessels, which were changed weekly. The collected solutions were analyzed for I, Cs, and Se. Measured quantities for later data processing were: thickness of sample, diameter of sample, duration of the experiment (taken after each change of the glass vessel from the time of first contact between pre-equilibrated sample and spiked solution), mass and density of solution collected in each time increment, concentration of spikers.

Opalinus solution, type A1 as described in /PEA 99/ was used as background solution. Analysis of Al, Ca, Fe, K, Mg, Sr, Na, S, and Si were preformed according to EN ISO 11885, Cl according to DIN 38405-D12. Inorganic C (TIC) was determined by the expulsion of CO_2 and UV-spectrometry.

3.1.3 Data Processing

From the mass of each individual solution sample collected, its density and its composition, the mass of spikers transported through the sample during each time increment in mol may be calculated. Divided by the total time and the area of the sample gives a flux in mol / m^2 s. This is the left side of equation (3.1). In a stationary state of equilibrium the cumulated masses of each spiker diffused through the sample and related to the area of the sample must be linearly in time. As long as it is not, a stationary equilibrium is not achieved. As soon as it is, and provided a sufficient number of data points is available, the diffusion coefficient D can be calculated by the division of the slope of the linear part of the graph by the concentration gradient, which is the factor for D on the right side of equation (3.1). The concentration gradient in the presented experimental setting can be assumed to be constant and is calculated as the spiker concentration in the lower part of the diffusion cell divided by the thickness of the sample.

3.1.4 Results

The observed flux of spikers is shown in Figure 3.3, calculated diffusion coefficients are presented in Table 3.1. Cs, positively charged and therefore capable of ion exchange with sites of permanent negative charge on the Callovo-Oxfordian argillite exhibits the lowest rate of diffusion. Selenate diffuses at a higher rate than iodide. This is contrary to expectations as long as the ionic radii of iodide and selenate are considered, which is larger for selenate. It may be speculated that transport of iodide in comparison to selenate is retarded by a reaction with inner surfaces of the argillite. Oxidation to elemental I_2 (aq) could also lead to retardation but having the constituents of the argillite in mind (Emmanuel Jacquot, ANDRA, 24.2.2003, personal communication) no obvious electron acceptor seems to be available for that purpose.

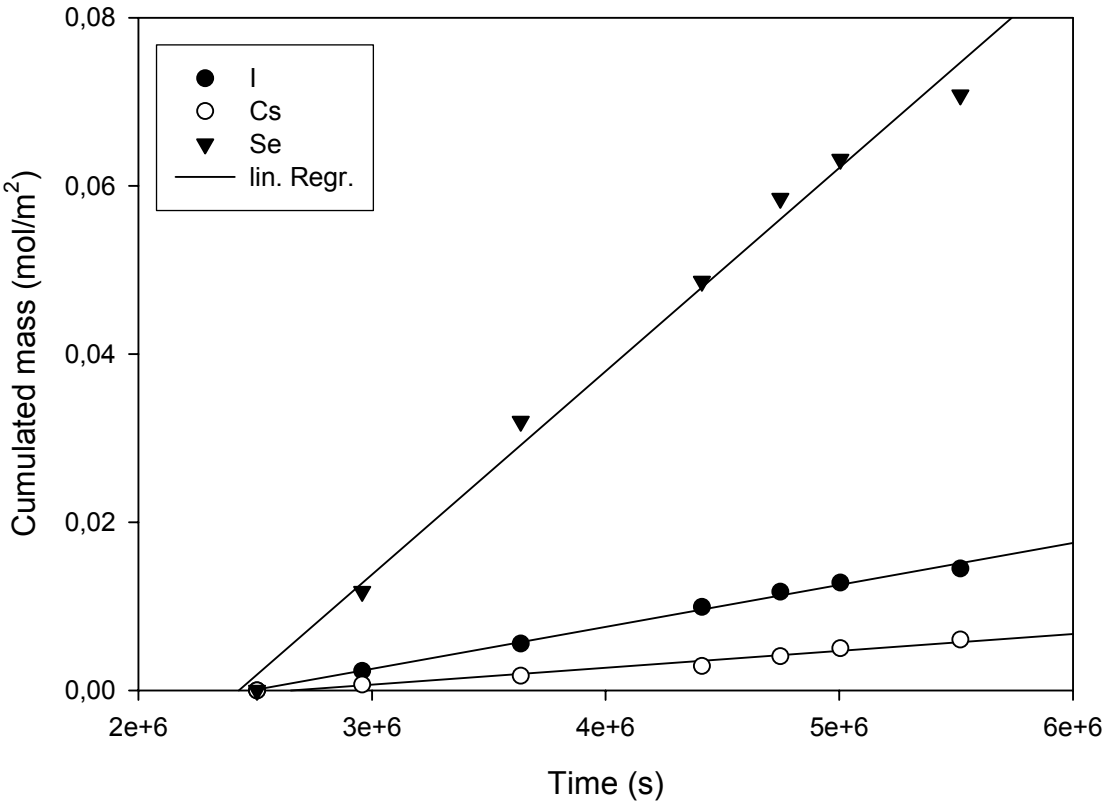

Figure 3.3 Flux of spikers through Bure clay

Table 3.1 Diffusion coefficients of I-, Cs+, and SeO_4^{2-} in the Callovo-Oxfordian argillite

Diffusing species	Diffusion Constant (m^2 / s)
I^-	$4.8 \cdot 10^{-9}$
Cs^+	$2.0 \cdot 10^{-9}$
SeO_4^{2-}	$4.4 \cdot 10^{-8}$

3.2 Leaching of the Callovo-Oxfordian Argillite

3.2.1 Introduction

Once released from waste containments radionuclides may be transported through the geosphere. For ionic contaminants the transport medium will be primarily aqueous solution, filling pores and fissures in the geologic matrix. The modelling of speciation and solubility of contaminants is essential for ultimately assessing their mobility within the geologic matrix. This can be done only if the composition of aqueous solution in the pores of the geologic matrix is known.

The determination of pore water composition in clay stones is an intricated matter and has given rise to much discussion in the scientific literature. Extraction by low pressure may be impossible due to the very small pore diameters in clay stones. Squeezing is difficult if not impossible, having in mind water contents of very few percents. In addition, squeezing may lead to erraneous results because the composition of expelled solution varies with overload pressure due to ultrafiltration by the clay matrix.

Another approach combines various techniques, where e. g. the phase assemblage of the clay is determined together with the cation composition on the surface of clays with permanent charge. Leaching and thermodynamic modelling ultimately lets one approximate iteratively a theoretical composition of pore water, in accordance with all previous findings.

It was the objective of this project to explore the possibility to make use of another method, the so-called „Cascade Leaching Experiment", originally invented for the investigation of the interaction of solid toxic waste with aqueous solutions.

3.2.2 Materials and Methods

In each equilibration ground Callovo-Oxfordian argillite and quartz sand in a weight ratio of 1:1 were agitated head-over with the three-fold mass of solution. A cascade chamber is presented in Figure 3.4. Mixing of the argillite with quartz sand was necessary to be able to transfer solution through the lower filter. Throughout the experiment the slurry had contact with nitrogen only.

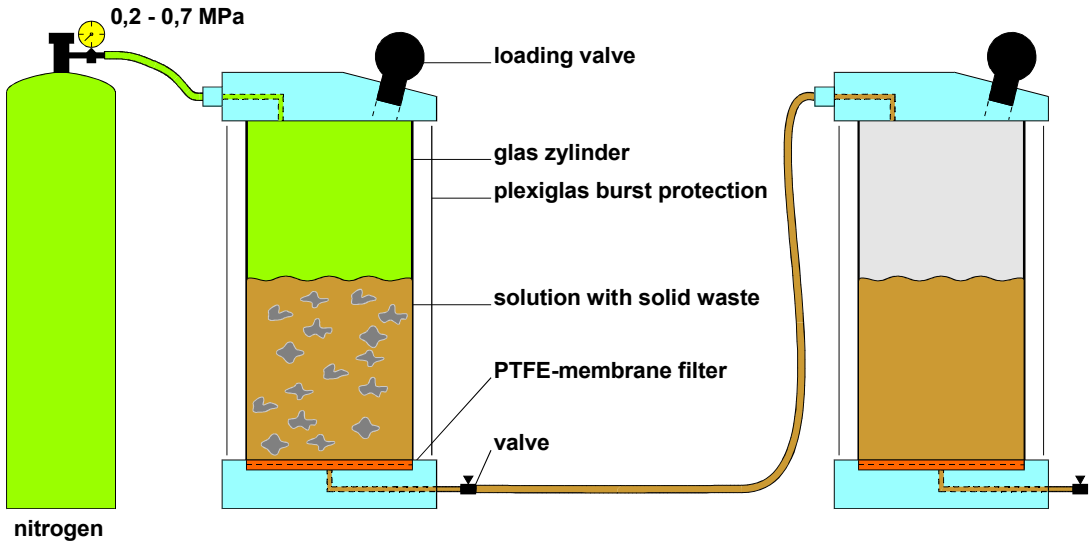

Figure 3.4 Principal sketch of a cascade reaction chamber and how after equilibration solution is transferred into another chamber.

Figure 3.5 illustrates, how with every new cascade the effective solid-solution-ratio is successively increased. After each equilibration solution is transferred into a new cascade with unreacted solid. Ideally, after a sufficient high number of equilibration steps, the solution composition should approximate that to which the original solid is in equilibrium.

As in each step a small part of the solution is retained in the solid, the available solution volume for the next equilibration step decreases, until after a number of steps, new solution with the composition of the last equilibrated one must be prepared.

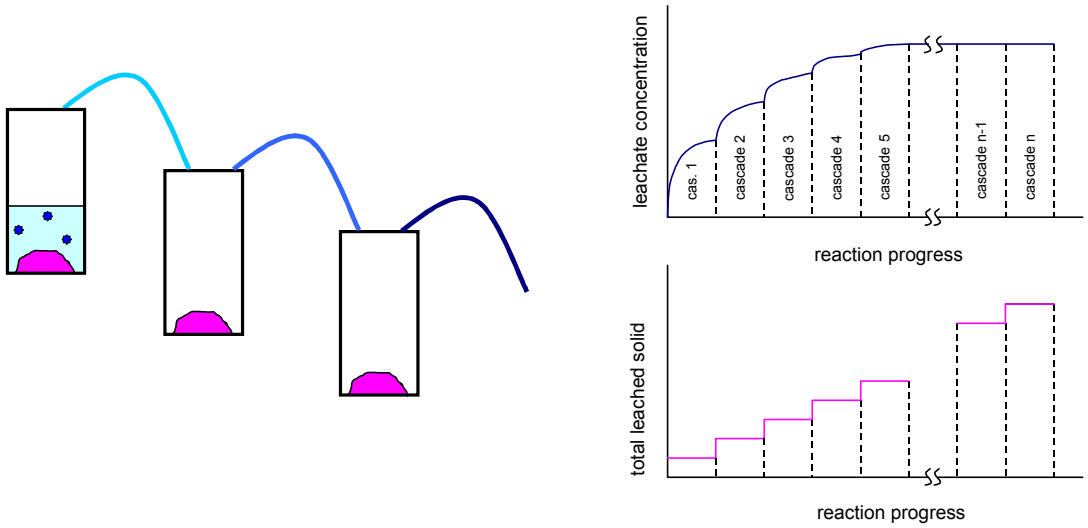

Figure 3.5 Principal sketch of a cascade leaching experiment

The first experiment was begun with Opalinus solution. However, during the experiment we felt, that the total salinity of this solution might be too high for the Callovo-Oxfordian argillite. Therefore, in a late phase of the project we decided to perform a second, shorter experiment in which a much more diluted solution was taken. This was stored over a deposit of calcite, kaolinite, and pyrite prior to the experiment.

Analyses of the solutions were performed as was described in chapter 3.1.2. As the air-dried argillite takes up water from solution, analytical results were normalized to constant concentration of chloride, assuming that no solubility limiting chloride-bearing phase is present in the argillite.

3.2.3 Results

Figure 3.6 shows how concentrations of Mg, Ca, and SO_4 evolve with increasing solid-solution-ratio (SSR). For Ca in the second experiment, concentrations level out to slightly lower values than in the first one.

For SO_4, concentrations are lower with the second experiment though higher at the beginning. Ca and SO_4 in both experiments follow the same tendency, i.e. decreasing and increasing with SSR.

With Mg, two opposite trends are observed: increasing during the first experiment, and decreasing during the second one.

As a matter of fact, several processes take place during the reaction between the argillite with all its constituents and solution: dissolution and precipitation, and ion exchange. These processes take place simultaneously, dissolution and precipitation, having the mineral assemblage of the argillite in mind, are subject to kinetic control. On this background it is difficult to find explanations from a single leaching curve, and identifying one process to be most probably the dominating one does not exclude to take place other processes as well.

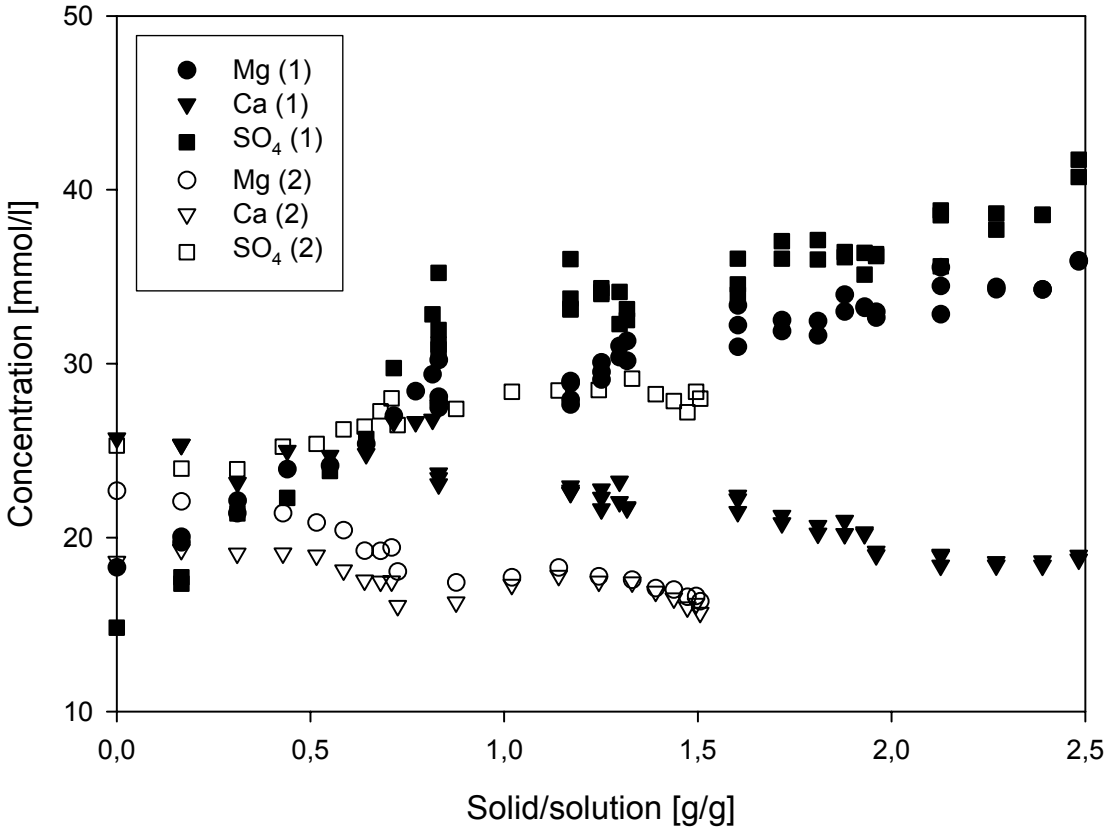

Figure 3.6 Evolution of concentrations for Mg, Ca, and SO_4 during both experiments

However, the opposite trends of Mg indicate that ion exchange is responsible here. For the first experiment Opalinus solution was prepared in which Na/Mg (mmol-base) was about 14.8. For the second experiment, Na/Mg was about 1.1 with a solution normality of about a third compared to Opalinus solution. The accessible surface of the smectitic

and illitic fraction of the argillite is covered with cations whose composition attains ion exchange equilibrium with cations in solution. At high Na/Mg values, as in Opalinus solution, Mg and in fact other bivalent cations like Ca and Sr as well are released in favour of Na. The change of Na (Figure 3.7) is not significant with Opalinus solution due to the compareably high normality. But it can be taken from the second experiment.

With a lower Na/Mg ratio, as with the second solution, the exchanger complex in the argillite is taking up Na in favour of bivalent cations like Mg. It is hypothesized that the different trends of Mg are due to ion exchange. As Mg and Ca should exhibit similar exchange properties the in both cases decreasing tendency of Ca indicates another process taking place simultaneously.

K, generally at low concentration, increases in both experiments to approximate very similar values. As K exhibits a quite high affinity to smectitic phases, the increase seems to indicate rather towards a dissolution process, while the occupancy with K of ion exchanger sites is near to equilibrium.

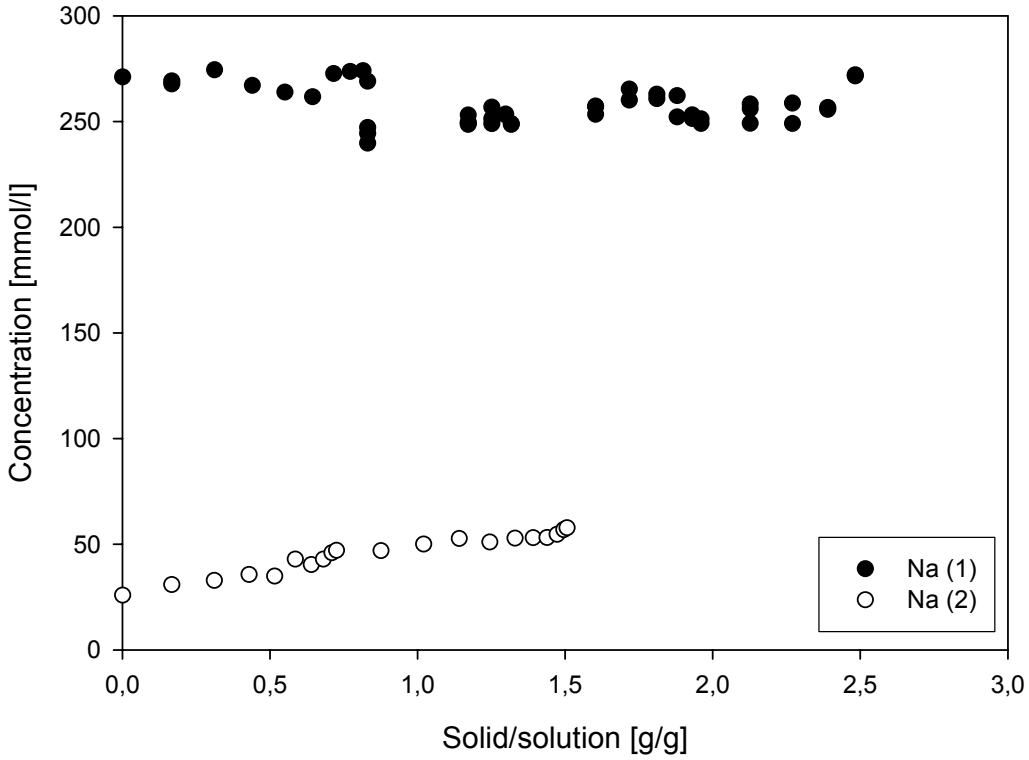

Figure 3.7 Evolution of concentrations for Na during both experiments

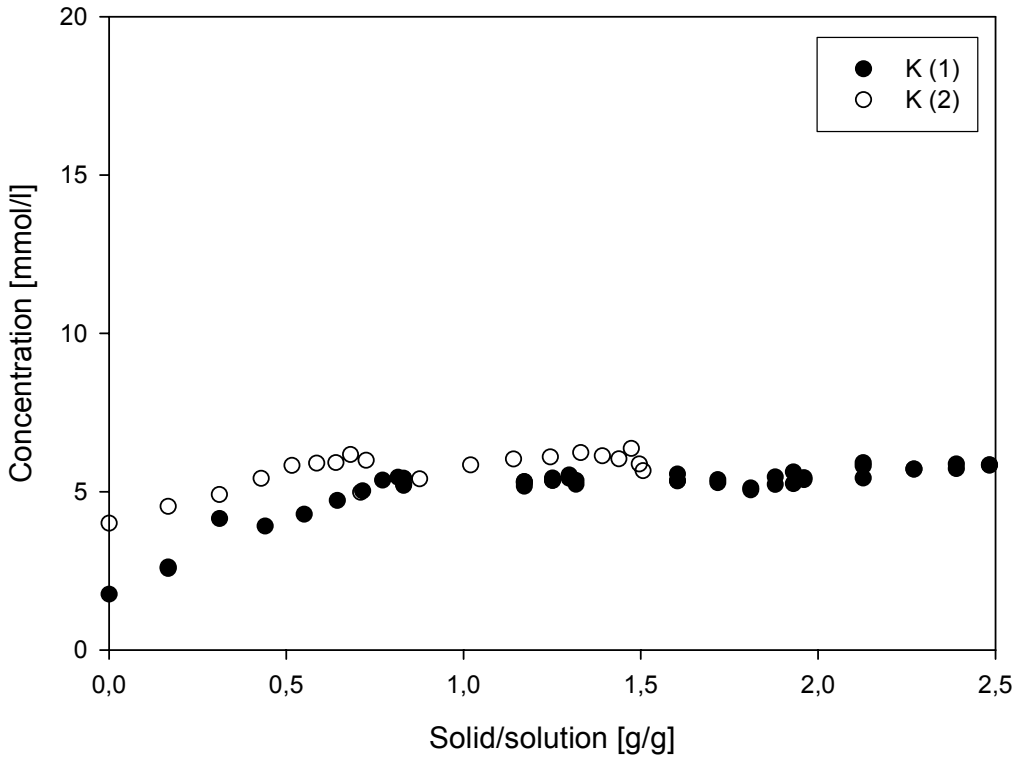

Figure 3.8 Evolution of concentrations for K during both experiments

Reactions determining pH (Figure 3.9) seem to be rapidly in equilibrium. However, after equilibration times of days or a week in this project, carbonates may have attained equilibrium, but phases containing Si or Al surely have not. But as carbonates in the argillite are positively identified (calcite, ankerite), the true pH in the pore waters can at least not be much lower.

In summary, solutions in equilibrium with unaltered the Callovo-Oxfordian argillite have clearly not been created in the course of these experiments. But the solution compositions measured indicate unbroken tendencies for each parameter sparking hope, that after a sufficient high number of cascades ion exchange equilibrium could be attained. As to much slowlier reactions taking place like dissolution and precipitation, much longer times of equilibration may be necessary. Elements like Si, Al, and Fe are then key parameters to be determined. However, with the presented set of experiment, difficulties will occur. First, the quartz sand utilized in the experiments reported here, released Si in proportions much higher than the argillite itself. Second, even if another truly inert stuff is found to loose up the clay structure for later filtration, colloids will remain within the pores of the - during filtration slightly compacted - clay, and tend to

entrap dissolved Si, Al, and Fe. Additional experiments are necessary to explore this effect prior to the continuation of efforts for the creation of equilibrated pore water with the cascade leaching technique.

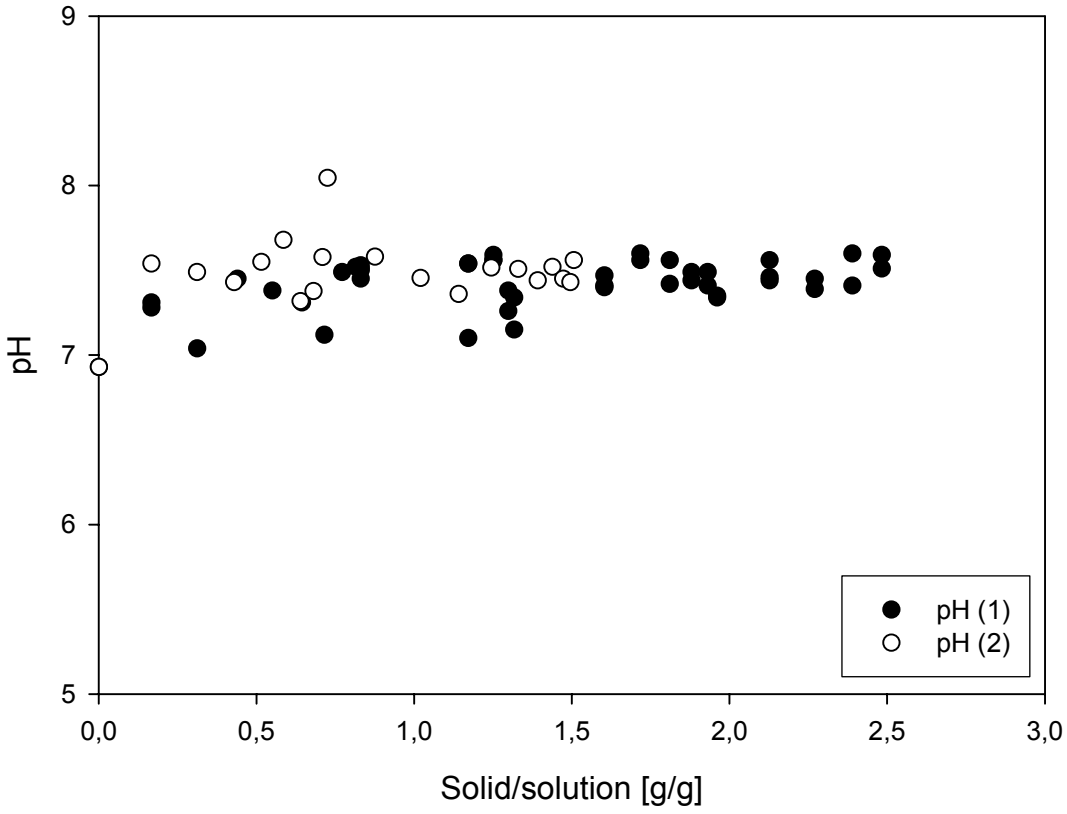

Figure 3.9 Evolution of pH during both experiments

4 Numerical Modelling

To gain experiences with numerical modelling of coupled thermo-hydro-mechanical processes in clays, a number of scoping calculations were performed by using the computer programme CODE-BRIGHT which has been developed by the Geotechnical Engineering Department of the Technical University of Catalonia in Barcelona for the analysis of coupled THM phenomena in geological media /UPC 02/. In this report, the theoretical framework of the CODE-BRIGHT is briefly reviewed. The associated material parameters for different clays, which haven been deduced from comprehensive laboratory and *in situ* experiments, are summarised and applied in some calculations. These modelling exercises included scoping calculations of coupled THM phenomena in clays under laboratory and *in situ* conditions. Some of the results were published /ZHA 03/.

4.1 Theoretical Framework

The programme CODE-BRIGHT handles coupled thermo-hydro-mechanical problems in porous media. The theoretical framework employed in the code is composed of three main parts: balance equations, equilibrium restrictions and constitutive equations. A general and detailed description of this formulation is presented in /OLI 94/. According to the manual of CODE-BRIGHT /UPC 02/ and the literature /OLI 94/, /GEN 98/, /ALO 02/, the equations are summarized in the following sections.

4.1.1 Balance Equations

The balance equations are established for the porous medium as a whole. The compositional approach is adopted to establish the mass balance equations. It consists of balancing the species rather than the phases. The following balance equations are considered:

- Balance of energy:

$$\frac{\partial}{\partial t}\left[E_s \rho_s (1-\phi) + E_l \rho_l S_l \phi + E_g \rho_g S_g \phi\right] + \nabla \cdot (\mathbf{i}_c + \mathbf{j}_{Es} + \mathbf{j}_{El} + \mathbf{j}_{Eg}) = f^E \qquad (4.1)$$

where E_s, E_l and E_g are specific internal energies corresponding to the solid, liquid and gaseous phases, ρ_s, ρ_l and ρ_g are the densities of the three phases, ϕ is porosity, S_l is the volumetric liquid fraction and S_g is the volumetric gaseous fraction with respect to the pore volume, $S_l + S_g = 1$. $\mathbf{i}_c$ is the non-advective (conductive) heat flux and $\mathbf{j}_{Es}$, $\mathbf{j}_{El}$, $\mathbf{j}_{Eg}$ are the advective energy flux of each of the three phases with respect to a fixed reference system. The most relevant advection energy fluxes correspond to vapour and liquid water motion. f^E is the energy supply per unit volume of the considered medium.

- Balance of water mass:

$$\frac{\partial}{\partial t}(\theta_l^w S_l \phi + \theta_g^w S_g \phi) + \nabla \cdot (\mathbf{j}_l^w + \mathbf{j}_g^w) = f^w \tag{4.2}$$

where θ_l^w and θ_g^w are the mass of water per unit volume of liquid and gas, respectively, $\mathbf{j}_l^w$ and $\mathbf{j}_g^w$ denote the total mass flux of water in the liquid and gas phases with respect to a fixed reference system and f^w is the external mass supply of water per unit volume of medium.

- Balance of air mass:

$$\frac{\partial}{\partial t}(\theta_l^a S_l \phi + \theta_g^a S_g \phi) + \nabla \cdot (\mathbf{j}_l^a + \mathbf{j}_g^a) = f^a \tag{4.3}$$

where θ_l^a and θ_g^a are the mass of dry air per unit volume of liquid and gas, respectively, $\mathbf{j}_l^a$ and $\mathbf{j}_g^a$ indicate the total mass flux of air in the liquid and gas phases with respect to a fixed reference system, and f^a is the external mass supply of air per unit volume of medium.

- Balance of momentum (equilibrium):

$$\nabla \cdot \boldsymbol{\sigma} + \mathbf{b} = \mathbf{0} \tag{4.4}$$

where $\boldsymbol{\sigma}$ represents the stresses and **b** the body forces.

4.1.2 Equilibrium Restrictions

Equilibrium restrictions are given for the concentration of water vapour in gas and of dissolved air in water.

The mass of water vapour per unit volume of gas (θ_g^w) is determined via the psychrometric law:

$$\theta_g^w = (\theta_g^w)^0 \exp\left[\frac{-(P_g - P_l) M_w}{R(273.15 + T)\rho_l} \right] \tag{4.5}$$

where P_l and P_g are liquid and gas pressures, respectively, $(\theta_g^w)^0$ is the vapour density in the gaseous phase in contact with a planar surface (i.e. when $P_g - P_l$ = 0), M_w is the molecular mass of water (0.018 kg/mol), R is the gas constant (8.314 J/mol K) and T is the temperature (in degrees Celsius). $(\theta_g^w)^0$ is dependent on temperature. The vapour partial pressure is computed by means of the ideal gas law.

The solubility of air in water is controlled by Henry's law:

$$\omega_l^a = \frac{P_a}{H} \frac{M_a}{M_w} \tag{4.6}$$

where ω_l^a is the mass fraction of air in the liquid, P_a is the partial pressure of air, M_a is the molecular mass of air (0.02895 kg/mol) and H = 10000 MPa is Henry's constant. According to the definition of partial density, $\theta_l^a = \omega_l^a \rho_l$.

4.1.3 Constitutive Equations

4.1.3.1 Thermal Equations

It is assumed that the conductive heat flow is governed by Fourier's law:

$$\mathbf{i}_c = -\lambda \nabla T \tag{4.7}$$

where λ is the global thermal conductivity. The dependence of λ on the degree of liquid saturation and porosity is given by the geometric mean approximation:

$$\lambda = \lambda_s^{(1-\phi)} \lambda_l^{(\phi \cdot S_l)} \lambda_g^{\phi(1-S_l)} = \lambda_{sat}^{S_l} \lambda_{dry}^{(1-S_l)} \tag{4.8}$$

where λ_s, λ_l and λ_g are the thermal conductivities of the individual phases, $\lambda_{sat} = \lambda_s^{(1-\phi)} \lambda_l^{\phi}$ and $\lambda_{dry} = \lambda_s^{(1-\phi)} \lambda_g^{\phi}$ are the thermal conductivities for saturated and dry conditions, respectively.

The internal energies per unit mass for each phase can be written as

$$E_l = E_l^w \omega_l^w + E_l^a \omega_l^a \tag{4.9a}$$

$$E_g = E_g^w \omega_g^w + E_g^a \omega_g^a \tag{4.9b}$$

where E_l^w = 4180.0 T (J/kg), E_l^a = 1006.0 T (J/kg), E_g^w = $2.5 \cdot 10^6$ +1900 T (J/kg) and E_g^a = 1006 T (J/kg). The value of E_s depends on the type of solid material.

4.1.3.2 Hydraulic Equations

Liquid and gas flow follow Darcy's law:

$$\mathbf{q}_l = -\mathbf{K}_l (\nabla P_l - \rho_l \mathbf{g}) \tag{4.10a}$$

$$\mathbf{q}_g = -\mathbf{K}_g (\nabla P_g - \rho_g \mathbf{g}) \tag{4.10b}$$

where $\mathbf{K}_\alpha = \mathbf{k}\, k_{r\alpha} / \mu_\alpha$ is the permeability tensor. The intrinsic permeability tensor (**k**) depends on the pore structure of the porous medium. $k_{r\alpha}$ is the value of relative permeability that controls the variation of permeability in the unsaturated regime and μ_α denotes the dynamic viscosity. α stands for either l or g depending on whether liquid or gas flow is considered. **g** is the gravity vector. The variation of intrinsic permeability with porosity is given by

$$\mathbf{k} = \mathbf{k}_0 \frac{\phi^3}{(1-\phi)^2} \frac{(1-\phi_0)^2}{\phi_0^3} \tag{4.11}$$

where ϕ_0 is a reference porosity. The relative permeabilities of the liquid and gaseous phases are dependent on the degree of liquid saturation according to

$$S_e = \frac{S_l - S_{lr}}{S_{ls} - S_{lr}} \tag{4.12}$$

$$k_{rl} = S_e^{1/2} \cdot \left[1 - (1 - S_e^{1/\beta})^{\beta}\right]^2 \qquad S_e \leq 1 \tag{4.13}$$

or power law

$$k_{rl} = A \cdot S_e^B \tag{4.14}$$

$$k_{rg} = 1 - k_{rl} \tag{4.15}$$

where S_l, S_{lr}, S_{ls}, S_e are the actual, residual, maximum and effective saturation of liquid, respectively, and β, A and B are parameters.

It is necessary to define the retention curve of the materials relating the degree of saturation to suction $(P_g - P_l)$. The expression of Van Genuchten is selected

$$S_e = \left[1 + \left(\frac{P_g - P_l}{P_0}\right)^{1/(1-\beta)}\right]^{-\beta} \qquad P_g - P_l \geq 0 \tag{4.16}$$

where P_0 is a material parameter.

The molecular diffusion of vapour in air is governed by Fick's law:

$$\mathbf{i}_g^w = -\mathbf{D}_g^w \nabla \omega_g^w = -(\phi \ \rho_g S_g \tau \ \mathbf{D}_m^w \ \mathbf{I} \ + \ \rho_g \ \mathbf{D}_g') \ \nabla \omega_g^w \tag{4.17}$$

where $\mathbf{i}_g^w$ is the non-advective mass flux of water in gas, $\mathbf{D}_g^w$ is the dispersion tensor, ω_g^w is the mass fraction of water in gas, τ is the tortuosity and $\mathbf{D}_g'$ is the mechanical dispersion tensor. Usually, a constant dispersion coefficient corresponding to the molecular diffusion of vapour in air is assumed:

$$D_m^w = 5.9 \cdot 10^{-12} \cdot \frac{(273.15 + T)^{2.3}}{P_g} \qquad (m^2 / s) \tag{4.18}$$

P_g is given in MPa. $\mathbf{D}'_g$ can be neglected if air flow is insignificant.

4.1.3.3 Mechanical Equations

In saturated porous materials, mechanical behaviour is best understood in terms of effective stress $\boldsymbol{\sigma}' = \boldsymbol{\sigma} - P_l \mathbf{m}$ where $\mathbf{m}^T$ is an auxiliary vector [1, 1, 1, 0, 0, 0]. For unsaturated materials it is necessary to consider two independent stress variables: net stresses $(\boldsymbol{\sigma} - P_g \mathbf{m})$ and capillary suction $s = (P_g - P_l)$. The net stress is the excess of total stress over gas pressure. If full saturation is achieved, net stress becomes effective stress.

The mechanical constitutive equation takes the incremental form

$$d\boldsymbol{\sigma}' = \mathbf{D} d\boldsymbol{\varepsilon} + \mathbf{h} ds + \boldsymbol{\beta} dT \tag{4.19}$$

where $\boldsymbol{\sigma}'$ is now used for net stresses, $\boldsymbol{\varepsilon}$ is the strain tensor. $\mathbf{D}$ is the constitutive stiffness matrix and $\mathbf{h}$ is a constitutive vector relating changes of suction to changes in net stresses and **ß** is a thermal expansion vector.

An elastoplastic law named Barcelona Basic Model (BBM) is implemented in the CODE-BRIGHT, which is able to represent many mechanical features of unsaturated soils in a consistent and unified manner /ALO 98/00/02/, /GEN 95/98/. In terms of stress invariants, the yield surface is written as

$$F = f\left(p', J, \theta, \varepsilon_v^o, s, T\right) \tag{4.20a}$$

where

$$p' = \frac{1}{3}(\sigma'_x + \sigma'_y + \sigma'_z) = p - \max(p_g, p_l) \tag{4.20b}$$

$$J = \frac{1}{2}\,\mathrm{trace}\left(\mathbf{s} : \mathbf{s}\right) \qquad \mathbf{s} = \boldsymbol{\sigma}' - p'\mathbf{I} \tag{4.20c}$$

$$\theta = -\frac{1}{3}\sin^{-1}(1.5\sqrt{3}\det \mathbf{s}/J^3) \tag{4.20d}$$

I is the identity tensor. For simplicity, a form of the classical Modified Cam-Clay model is taken as the yield function:

$$F = \frac{3J^2}{g_y^2} - L_y^2(p' + p_s)(p_0 - p') \tag{4.21}$$

where g_y is a function of Lode's angle (θ), $L_y = M/g_y\big|_{\theta=-\pi/6}$ and M is a constant characterising the critical failure state line

$$q = M \cdot p' \tag{4.22}$$

where q is the deviatoric stress.

It is assumed that the apparent cohesion increases with suction by

$$p_s = p_{so} + \kappa \cdot s \cdot \exp(-p\Delta T) \tag{4.23}$$

where p_{so} is the tensile strength in saturated conditions, κ and p are parameters.

The net isotropic yield stress p_o is considered to be dependent on suction and temperature through

$$p_o = p^c\left(\frac{p_o^*(T)}{p^c}\right)^{\frac{\lambda(o)-k_{io}}{\lambda(s)-k_{io}}} \tag{4.24a}$$

with

$$p_o^*(T) = p_o^* + 2(\alpha_1 \Delta T + \alpha_3 \Delta T|\Delta T|) \tag{4.24b}$$

$$\lambda(s) = \lambda(o)[(1-r)\exp(-\beta s) + r] \tag{4.24c}$$

$$\Delta T = T - T_{ref} \tag{4.24d}$$

where p_o^*, $p_o^*(T)$ are the net yield stresses for saturated conditions at a reference temperature (T_{ref}) and elevated temperature (T), respectively; α_1, α_3 are parameters for the plastic thermal strain; $\lambda(o)$, $\lambda(s)$ are the slopes of the virgin compression lines for saturated and unsaturated conditions, respectively; r is a constant related to the maximum stiffness $r = \lambda(s_{max})/\lambda(o)$; β provides the rate of change of $\lambda(s)$ with s; k_{io} is the initial slope of the isotropic unloading-reloading paths for saturated conditions; p^c is a reference stress.

Hardening depends on plastic strain according to

$$\frac{dp_o^*}{p_o^*} = \frac{v}{\lambda(o) - k_{io}} d\varepsilon_v^p \tag{4.25}$$

where $v = 1 + e$ is the specific volume, e is the void ratio.

The plastic potential is taken as

$$G = \frac{3J^2}{g_p^2} - \alpha L_p^2 (p' + p_s)(p_o - p') \tag{4.26}$$

where g_p is a function of Lode's angle (θ), $L_p = M/g_p\big|_{\theta=-\pi/6}$ and α is a non-associativity parameter.

Volumetric elastic strains induced by changes of net mean stress, suction and temperature inside the elastic domain are given by

$$d\varepsilon_v^e = d\varepsilon_{vp}^e + d\varepsilon_{vs}^e + d\varepsilon_{vT}^e \tag{4.27a}$$

with

$$d\varepsilon_{vp}^e = \frac{k_i\, dp'}{v\ p'}$$

$$k_i = k_{io}(1 + \alpha_i s) \tag{4.27b}$$

$$d\varepsilon_{vs}^{e} = \frac{k_s}{v}\frac{ds}{s + p_{at}}$$

$$k_s = k_{so}\left(1 + \alpha_{sp}\ln\left(\frac{p'}{p_{ref}}\right)\right)\exp(\alpha_{ss}s) \tag{4.27c}$$

$$d\varepsilon_{vT}^{e} = \alpha_o \Delta T + 2\alpha_2 |\Delta T| \Delta T \tag{4.27d}$$

where k_{io}, k_i are the slopes of the isotropic unloading-reloading paths for saturated and unsaturated conditions, respectively; k_{so}, k_s are the slopes of the wetting-drying paths for saturated and unsaturated conditions at a given stress p' in the elastic domain, respectively; p_{at}, p_{ref} are the atmospheric pressure and reference pressure, respectively; $\alpha_i, \alpha_{sp}, \alpha_{ss}, \alpha_o, \alpha_2$ are parameters.

Deviatoric elastic deformations are computed through shear modulus G:

$$d\varepsilon_{q}^{e} = \frac{G}{3}dq \tag{4.28}$$

with

$$G = \frac{3(1-2\nu)(1+e)}{2(1+\nu)\ k_i}p'$$

where ν is Poisson's ratio.

The relationship between the displacements (**u**) and the strains ($\boldsymbol{\varepsilon}$) is expressed as:

$$\boldsymbol{\varepsilon} = \frac{1}{2}\left(\nabla \mathbf{u} + \nabla \mathbf{u}^{T}\right) \tag{4.29}$$

4.2 Material Parameters

A number of parameters associated with the above equations are physical constants, the values of which have been indicated in chapter 4.1. However, there are material-specific parameters which are to be determined by laboratory and *in situ* experiments. In the international research projects of BACCHUS 2 /VOL 96/, RESEAL /VOL 00/, CATSIUS CLAY /ALO 00/, FEBEX /GEN 98/, /HUE 00/, VE /VE 02/, HE-B /HEB 02/, /FLO 02/, MODEX-REP /MOD 03/, /ZHA 02/ etc., various clays were investigated as host rock and buffer/backfill for the disposal of radioactive wastes in geological formations, such as:

- Boom clay as host rock at the HADES URL at Mol, Belgium;
- Serrata bentonite quarried in Southeastern Spain, which was used as sealing material in the borehole sealing test in the HADES URL, in the FEBEX experiment at Grimsel, and in the HE-B heating experiment in the Opalinus clay in the Mont Terri URL;
- FoCa bentonite from the Paris Basin, France, was used as sealing material in the borehole and shaft sealing test in the HADES URL;
- Opalinus clay as host rock at the Mont Terri URL;
- Callovo-Oxfordian argillite as host rock at the MHM - URL Bure in France.

Many THM experimental results are given in the literature mentioned above. Based on these, the material parameters associated with the constitutive equations implemented in the CODE-BRIGHT were determined for the clays and used in the analyses of the THM processes occurring in geological and engineered barriers. The mean values of the parameters taken from the literature are represented in Tables 4.1 and 4.2. It is to be noted that the certainty of the parameter values for some clays should be further improved, for instance, the mechanical parameters of the Opalinus clay were preliminarily determined based on very limited test data. The parameters for the Callovo-Oxfordian argillite have not been determined, yet. However, because of the great similarity between the Opalinus clay and the Callovo-Oxfordian argillite, the parameters of the Opalinus clay could be assumed to be adequately representative for the Callovo-Oxfordian argillite for the purpose of scoping calculations. Some important THM properties of the clays are compared in the following chapters 4.2.1 - 4.2.3 by using mean values.

Table 4.1 Physical properties of some clays

Property	Sym-bol	Unit	Serrata bentonite	FoCa bentonite	Boom clay	Opalinus clay	Callovo-Oxfordian argillite
Grain density	ρ_s	kg/m^3	2700	2670	2650	2710	2700
Dry density	ρ_d	kg/m^3	1550	1660	1670	2340	2250
Void ratio	e_o	-	0.741	0.608	0.588	0.190	0.202
Porosity	ϕ_o	-	0.426	0.378	0.370	0.160	0.168
Water content	w_o	(%)	14.0	11.0		6.85	7.70
Initial suction	s_o	MPa	107	117	0	0	0

4.2.1 Thermal Parameters

A basic parameter for temperature evolution and distribution is the thermal conductivity λ. A linear relationship between λ and S_l was determined for the Boom clay. Equation (4.8) is adopted for the Serrata bentonite. The thermal conductivity of the Opalinus clay exhibits an anisotropy with a value of λ = 2.1 W/(mK) parallel to the bedding and λ = 0.96 W/(mK) perpendicular to the bedding /BOC 01/. In the following calculations, equation (4.8) is adopted for the thermal conductivity of the Opalinus clay without consideration of the anisotropy. The thermal conductivities of the materials are illustrated in Figure 4.1. Generally, the thermal conductivity increases with liquid saturation. The heat capacity C = 1091 J/(kgK) for the Serrata bentonite solid phase is higher than C = 800 J/(kgK) for the Opalinus clay solid.

4.2.2 Hydraulic Parameters

The retention curves of the clays are plotted in Figure 4.2. For the Serrata bentonite, the retention curves for the drying and wetting paths are given, while for the Boom clay and the Opalinus clay the retention curves determined by drying are shown.

The intrinsic permeability of the different clays is presented in Figure 4.3 as a function of porosity. The permeability of the Serrata bentonite and the Opalinus clay decrease with decreasing porosity, while the permeability of the Boom clay was assumed as constant in some numerical calculations. The relative permeability to liquid of the clays is given as a function of liquid saturation in Figure 4.4.

Table 4.2 Constitutive parameters for some clays

Parameter in equation	Symbol	Unit	Serrata bentonite	FoCa bentonite	Boom clay	Opalinus clay
Thermal						
(4.8)	λ_{sat}	W/(mK)	1.507		1.44	1.6
(4.8)	λ_{dry}	W/(mK)	0.42		0.65	0.7
heat capacity	C	J/(kgK)	1091			800
Hydraulic						
(4.11)	ϕ_o	-	0.407	0.407	0.37	0.16
(4.11)	k_o	m^2	$6\cdot10^{-21}$	$6\cdot10^{-21}$	$4.5\cdot10^{-19}$	$2\cdot10^{-20}$
(4.12)	S_{lr}	-	0.01	0.01	0.0	0.007
(4.12)	S_{ls}	-	1.0	1.0	1.0	1.0
(4.14)	A	-	1	1		1
(4.14)	B	-	3	3		5
(4.16)	β	-	0.42[a]/0.35[b]	0.27	0.6	0.4
(4.16)	P_o	MPa	62[a]/7[b]	17	20	20
(4.17)	τ	-	1	1	1	0.8
Mechanical						
Elastic						
(4.27b)	k_{io}	-	0.05	0.1	0.00265	0.0035
(4.27b)	α_i	-	-0.003	-0.008	0	0
(4.27c)	k_{so}	-	0.3	0.3	0.0032	$4\cdot10^{-5}$
(4.27c)	α_{sp}	-	-0.1638	-0.1638	0	0
(4.27c)	α_{ss}	MPa^{-1}	-0.03	-0.03	0	0
(4.27c)	p_{ref}	MPa	0.01	0.01	-	-
(4.27d)	α_o	$^oC^{-1}$	$1\cdot10^{-5}$			$2.7\cdot10^{-5}$
(4.27d)	α_2	$^oC^{-2}$	0			0
(4.28)	ν	-	0.4	0.4	0.333	0.33
Bulk modulus [c]	K	MPa	35	16	600	3500
Shear modulus [c]	G	MPa	7.5	3.5	230	1340
Young's modulus	E	MPa	20	10	612	3570
Plastic						
(4.22)	M	-	1.5	1.5	1.0	1.5
(4.23)	k	-	-0.1		-0.007	-0.007
(4.23)	ρ	$^oC^{-1}$	0.2			0.2
(4.24a)	p^c	MPa	0.1		0.06	0.1
(4.24b)	p_o^*	MPa	14.0		6.0	20.0
(4.24b)	α_1	MPa^oC^{-1}	0		0	0
(4.24b)	α_3	MPa^oC^{-2}	0		0	0
(4.24c)	$\lambda(o)$	-	0.15	0.196	0.26	0.027
(4.24c)	r	-	0.75		0.564	0.6
(4.24c)	β	MPa^{-1}	0.05		0.544	0.015

[a]: Values obtained from drying tests
[b]: Values from wetting tests
[c]: Elastic parameters K,G and E are calculated for saturated conditions at p' = 1 MPa and $e=e_o$, $K=p'(1+e)/k_{io}$, $G=3K(1-2\nu)/2(1+\nu)$, $E=2G(1+\nu)$.

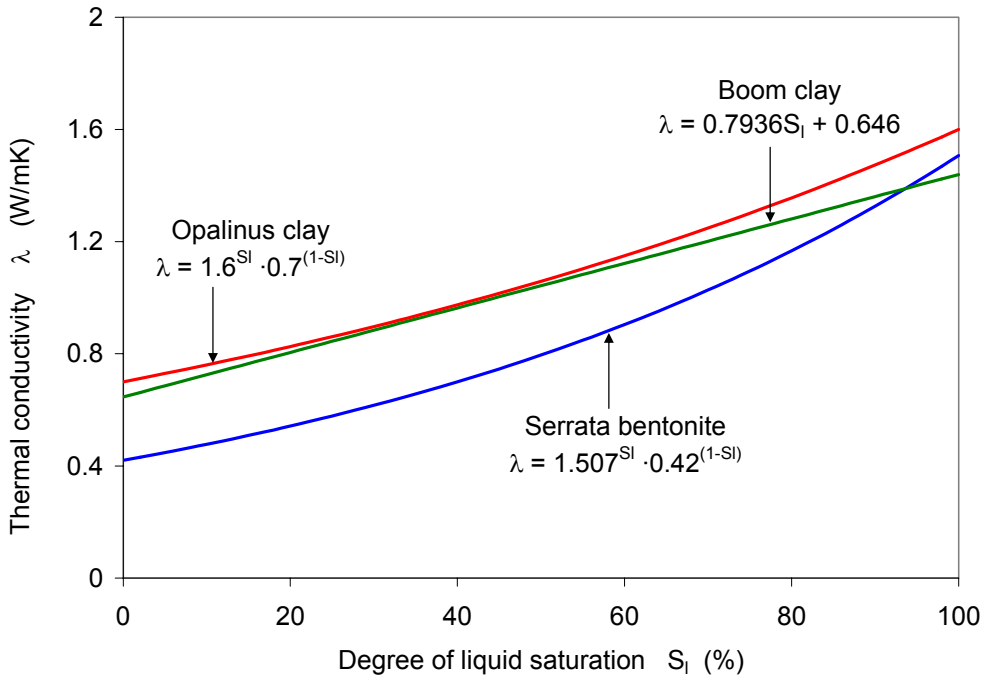

Figure 4.1 Thermal conductivity of clays as a function of liquid saturation

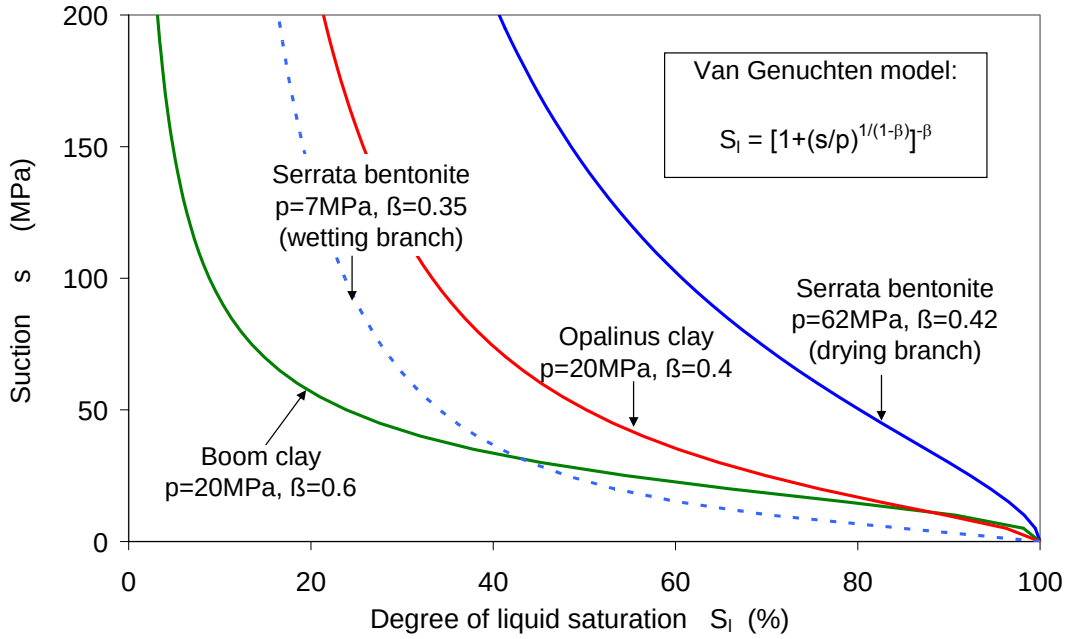

Figure 4.2 Retention curves of clays

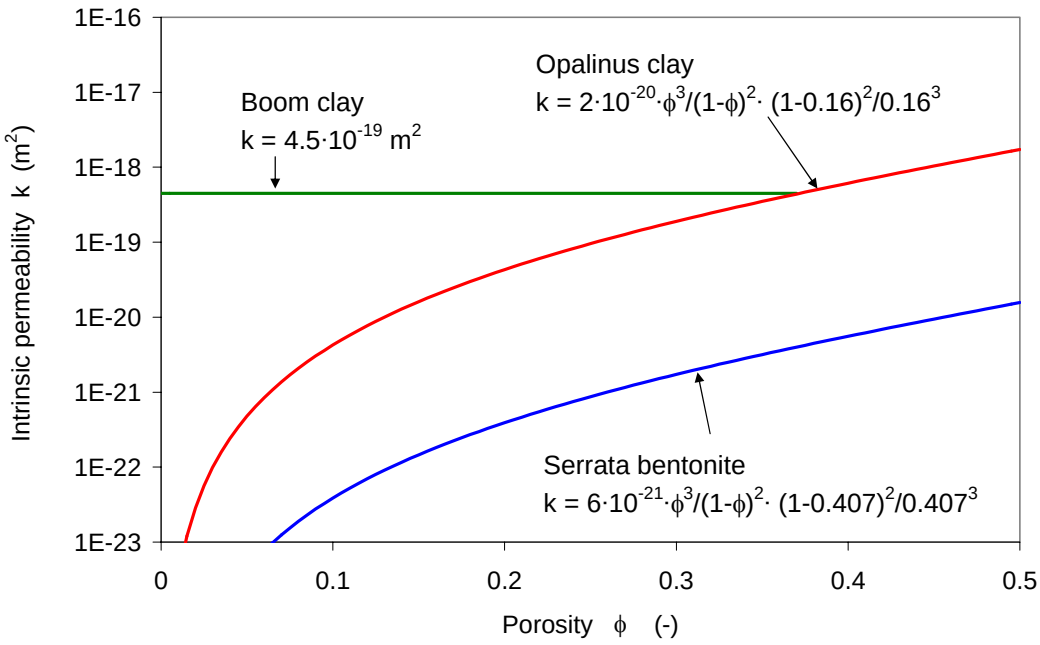

Figure 4.3 Intrinsic permeability of clays as a function of porosity

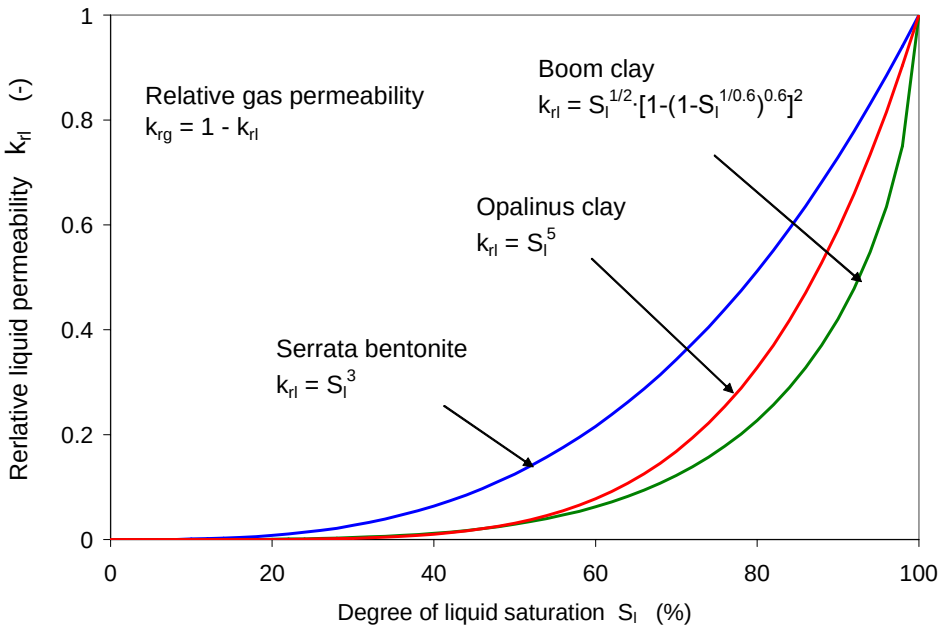

Figure 4.4 Relative permeability of clays as a function of liquid saturation

4.2.3 Mechanical Parameters

The main features of the BBM model implemented in the CODE-BRIGHT are represented below. A Loading-Collapse (LC) yield surface as a basic feature of the BBM model is illustrated in Figure 4.5 for the $p'-s$ space and for the $q-p'$ space. A family of ellipses is selected to represent the saturated and unsaturated yield loci. The smallest elastic domain corresponds to saturated conditions. Due to the shape of the LC yield surface, the elastic domain enlarges as suction increases. The slopes of the corresponding critical failure state lines are assumed to be the same one. Equation (4.23) is adopted for the apparent cohesion increase with suction.

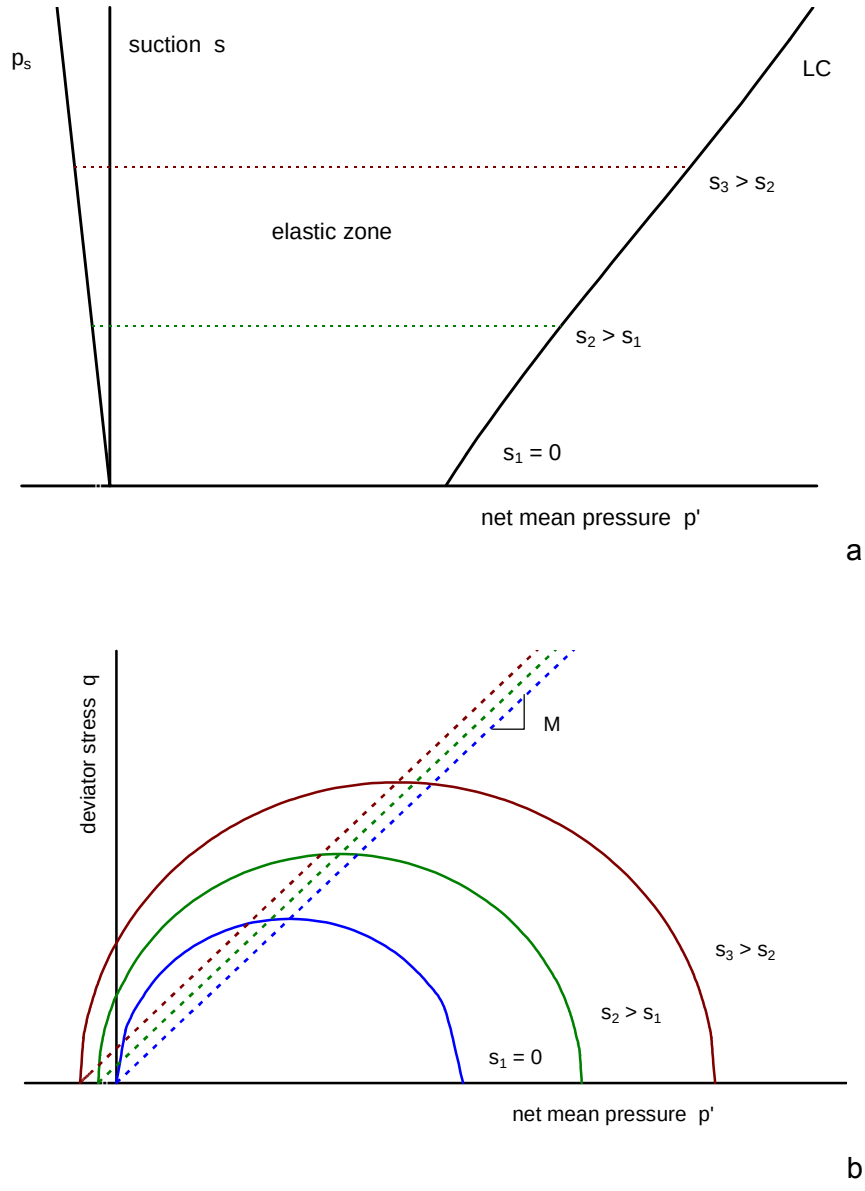

Figure 4.5 Yield surface of the BBM model for unsaturated soils

Figure 4.6 gives an example of the capability of the BBM model for reproducing the typical volumetric behaviour of unsaturated soils upon wetting and loading. If a soil specimen is wetted at low stress (point B inside the elastic zone) a recoverable swelling will ensue. However, if suction reduction occurs at a higher value of applied stress (point D on the LC yield surface), saturation will cause a movement of the yield surface and hence irreversible compressive strains (collapse). On the other hand, if the applied stress p' at point D increases, there will be also a translation of the LC yield surface leading again to irreversible compressive strains.

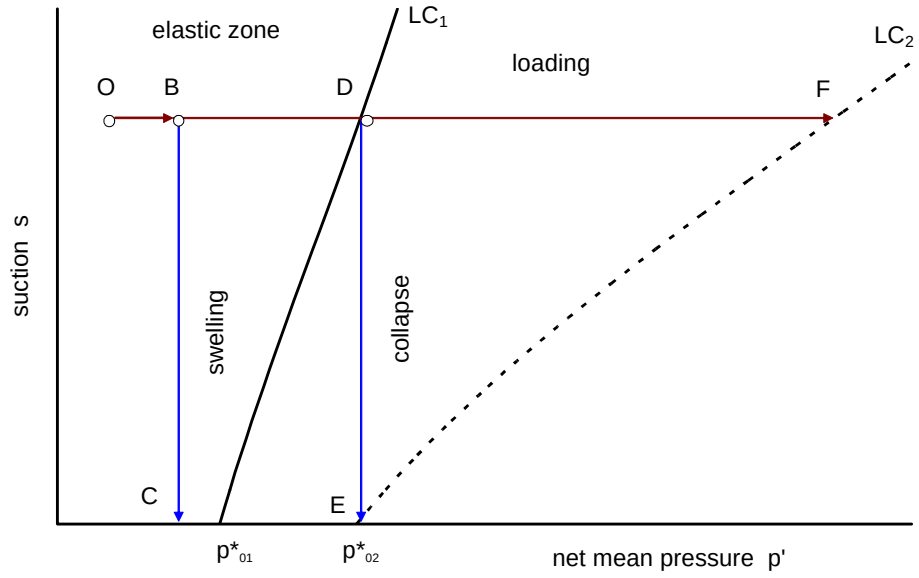

Figure 4.6 Volumetric response of unsaturated soils to wetting and loading

Because the LC yield curve (Eq. 4.24) integrates most of the plastic parameters $(p_o^*, p^c, k_{io}, \lambda(o), r, \beta, \alpha_1, \alpha_3)$, a useful way to compare them for different materials is to plot the LC curves, as given in Figure 4.7a for the Serrata bentonite, the Boom clay and the Opalinus clay. The yield curves in the $q-p'$ space and the failure state lines are given in Figure 4.7b for saturated conditions.

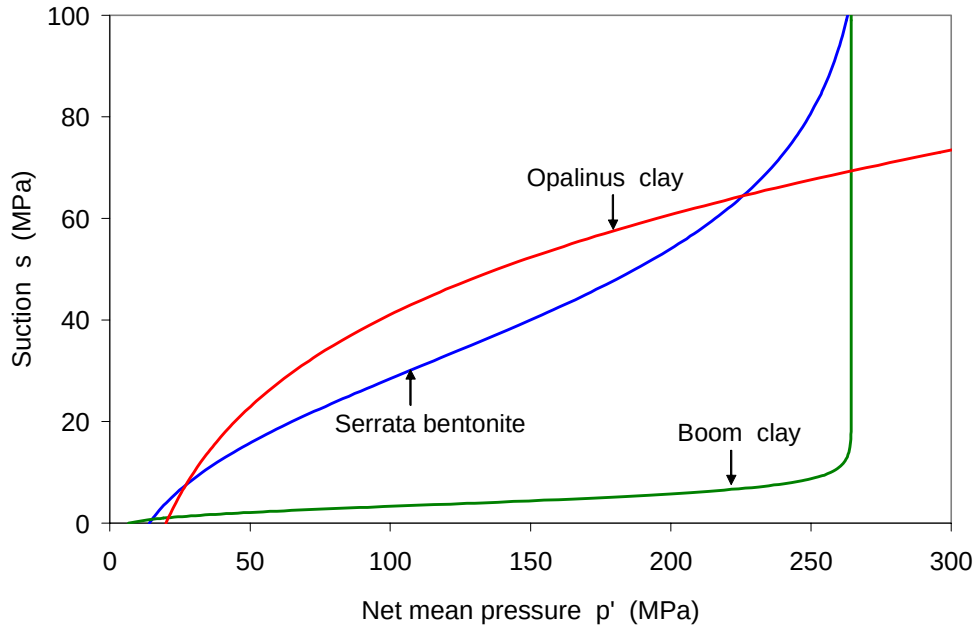

a: suction versus net mean pressure

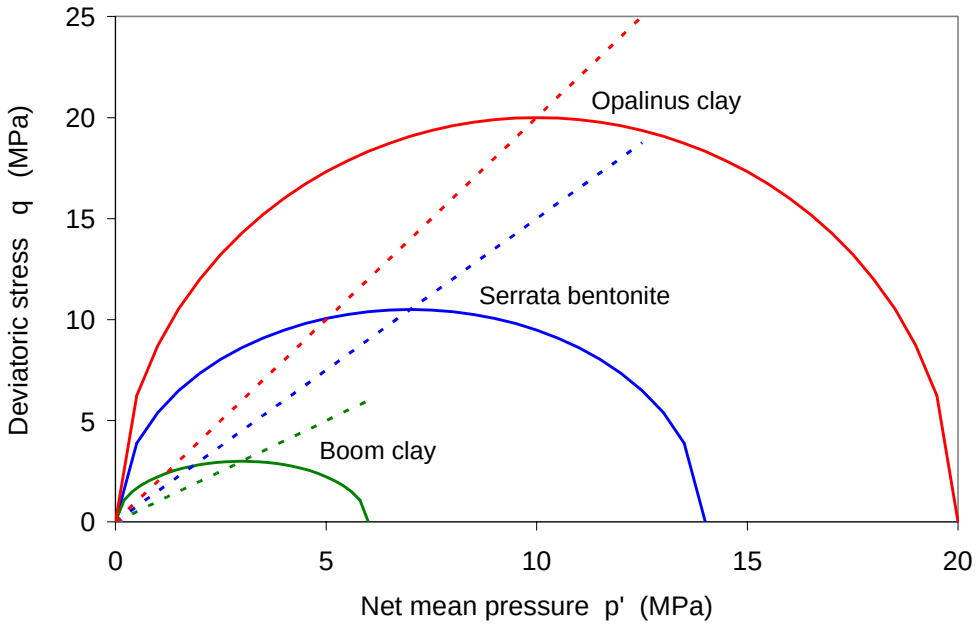

b: deviatoric stress versus net mean pressure

Figure 4.7 Comparison of yield curves of different clays

Figure 4.8 shows the isothermal consolidation behaviour of the clays in saturated (s = 0) conditions. The highly pre-consolidated Opalinus clay is much stiffer than the others.

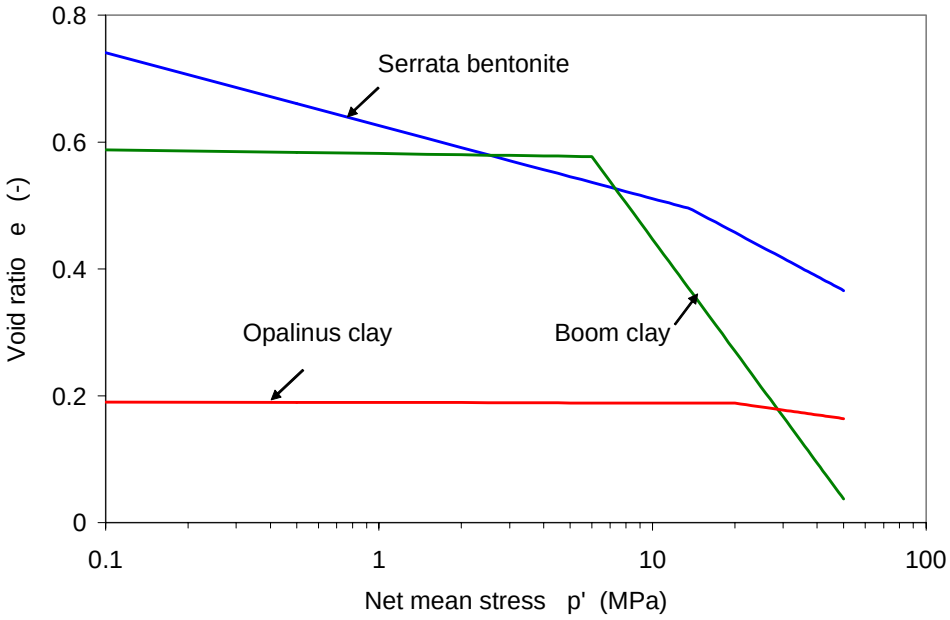

Figure 4.8 Consolidation behaviour of clays in saturated conditions

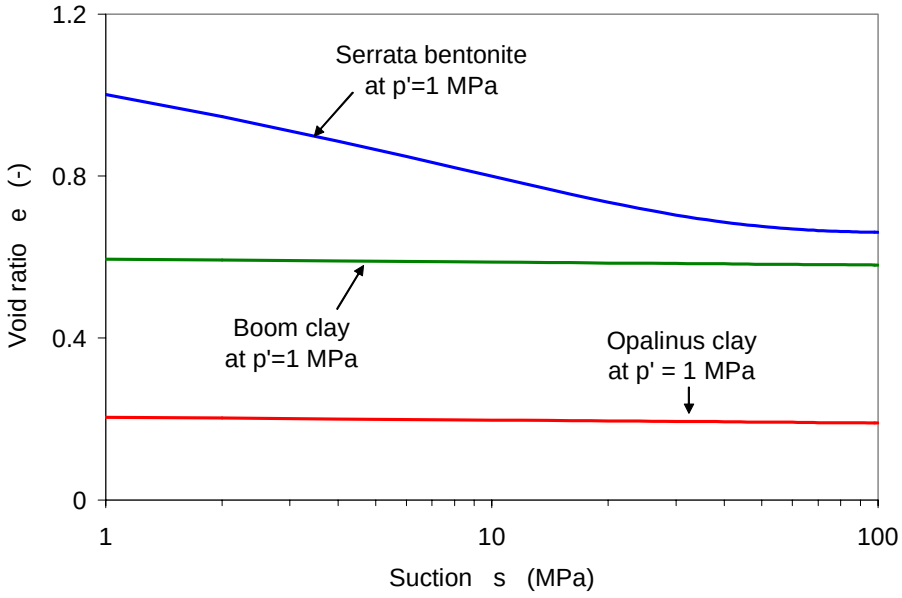

Figure 4.9 Swelling deformations of different clays

The swelling curves of the clays are compared in Figure 4.9 for a constant confining pressure p′ = 1 MPa. The Serrata bentonite highly expanses when wetted (reduction of suction), whereas the Boom clay and the Opalinus clay are less expansive.

4.3 Modelling of Normal Laboratory Experiments

In order to gain an insight into the capability of the CODE-BRIGHT for representing THM phenomena usually observed in the laboratory and to gain experiences for an adequate use of the code, a series of modelling exercises simulating normal laboratory experiments on clays was performed. The followings were considered: swelling behaviour due to hydration, consolidation and collapse by loading and wetting, resaturation by wetting and desaturation by drying, hydro-mechanical responses to heating.

4.3.1 Swelling Behaviour of Bentonite

Two isothermal swelling tests on the highly expansive Serrata bentonite were simulated, to examine:

1) swelling pressure at a constant volume,

2) swelling deformation at a constant vertical load.

An initially unsaturated specimen is placed in an oedometer cell of 70 mm diameter and 20 mm length and then wetted at the bottom by a constant water pressure of 0.1 MPa in both tests. The initial conditions of the specimens were: porosity ϕ = 42.6 %, degree of saturation S_l = 23.8 %, suction s = 107 MPa, initial stress $\sigma_1 = \sigma_2 = \sigma_3$ = 0.15 MPa in the swelling pressure test and $\sigma_1 = \sigma_2 = \sigma_3$ = 0.2 MPa in the swelling deformation test. Vertical displacement is constraint at the top and at the bottom of the specimen in the swelling pressure test, whereas a constant vertical load of 0.2 MPa is applied on the top of the specimen in the swelling strain test. Oedometer conditions are prescribed on the lateral sides of both tests.

The swelling behaviour of the bentonite is assumed to be controlled mainly by coupled hydro-mechanical effects. The equations solved are stress equilibrium (Eq. 4.4) and water mass continuity (Eq. 4.2). Vapour phase flow and air flow are not taken into

account. As a consequence, diffusive fluxes do not exist. The BBM model (Eqs. 4.21-28) is used to describe the mechanical behaviour of the specimen, while the hydraulic behaviour is defined by Darcy's law (Eq. 4.10), the intrinsic permeability (Eq. 4.11), the relative permeability (Eq. 4.14), and the retention curve (Eq. 4.16) obtained by wetting. The material parameters are given in Tables 4.1 and 4.2.

4.3.1.1 Swelling Pressure

Figure 4.10 shows the evolution of the water saturation in the elements at the bottom, centre and top of the specimen during wetting. The region at the bottom is saturated first. After about 400 hours the specimen is fully saturated. The saturation deduces local swelling strains, as shown in Figure 4.11, in which the porosities at the bottom, centre and top are plotted versus time. The bottom region is expanded, so that the other regions are compacted due to the confined volume. Figure 4.12 shows the swelling pressures in the axial and lateral direction during wetting. The swelling pressure increases with increasing water saturation. The swelling pressures reach the maximum values when the specimen is fully saturated. Whereas the vertical swelling pressure is independent on the location in the specimen, the lateral swelling pressure is higher at the bottom than in other regions. The inhomogeneous distribution of the lateral swelling pressure might be due to the different expansions in the specimen.

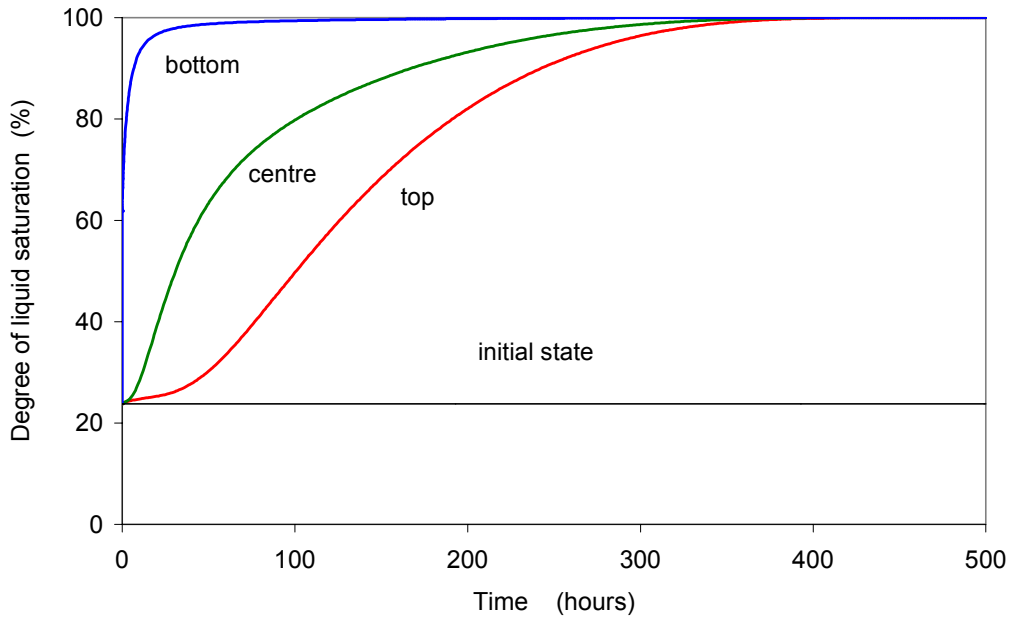

Figure 4.10 Evolution of water saturation during wetting

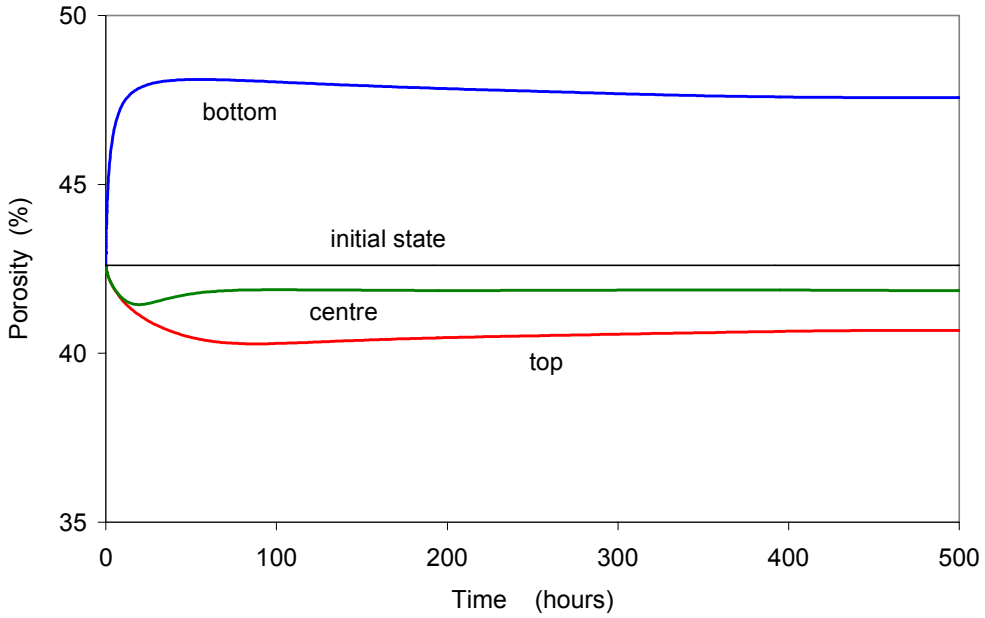

Figure 4.11 Porosity variation during wetting

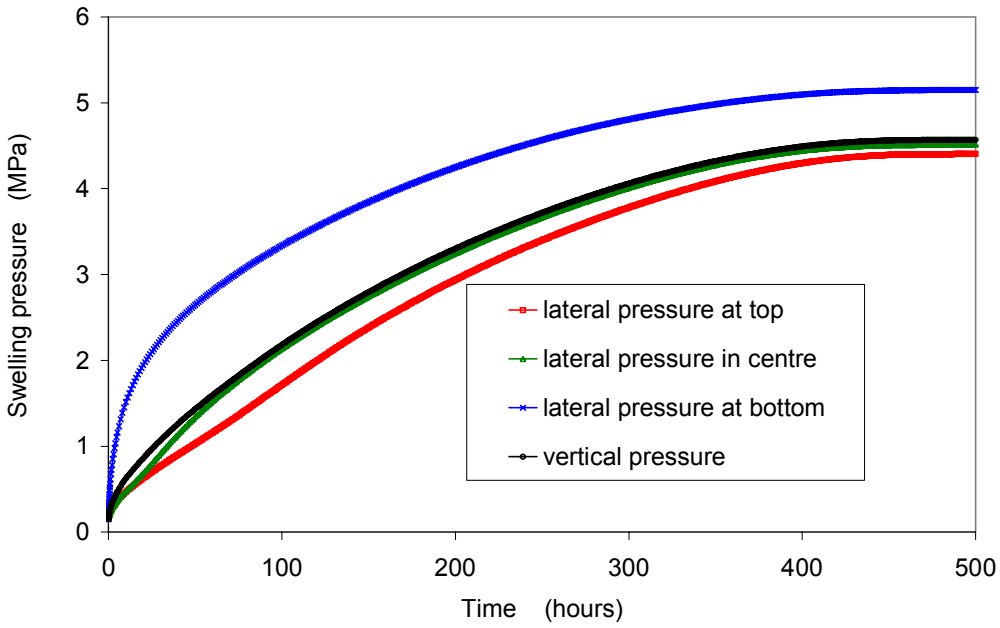

Figure 4.12 Evolution of swelling pressure during wetting

4.3.1.2 Swelling Strain

The evolution of the water saturation in the swelling strain test is similar to that in the swelling pressure test. In contrast to the swelling pressure test, the swelling strain test allows vertical deformation of the specimen. Figure 4.13 gives the evolution of the swelling strain, which reaches the maximum of 18 % when fully saturated. The specimen expands from the initial porosity of 42.6 % to the final value of about 52.3 %. In Figure 4.14 it is interesting to see that the lateral swelling pressures increase with increasing saturation up to a maximum of about 2.8 MPa due to the restricted lateral displacement, while the vertical swelling pressure maintains constant at the initial value of 0.2 MPa.

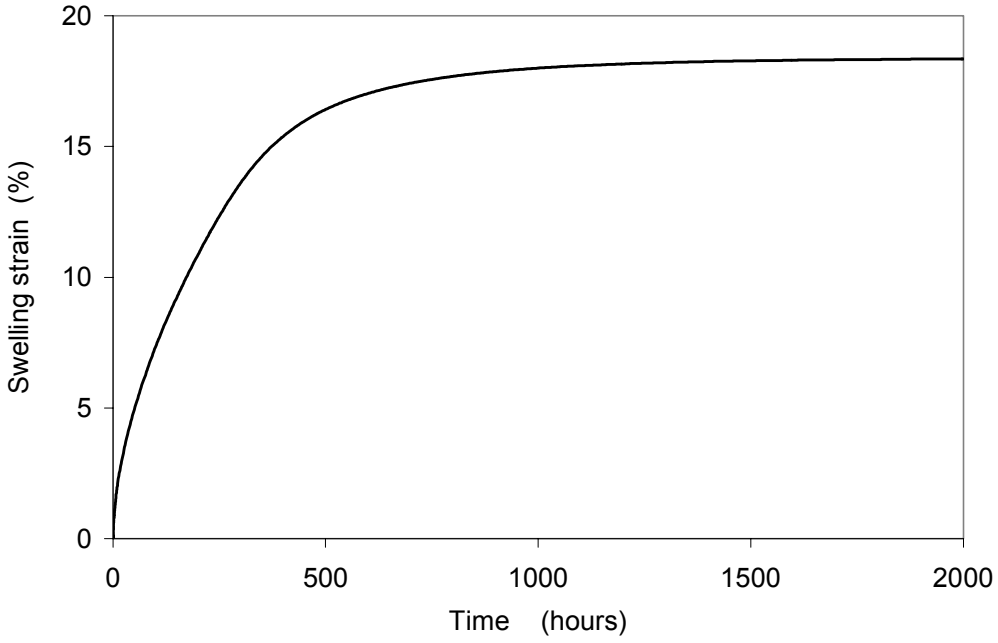

Figure 4.13 Swelling deformation during wetting

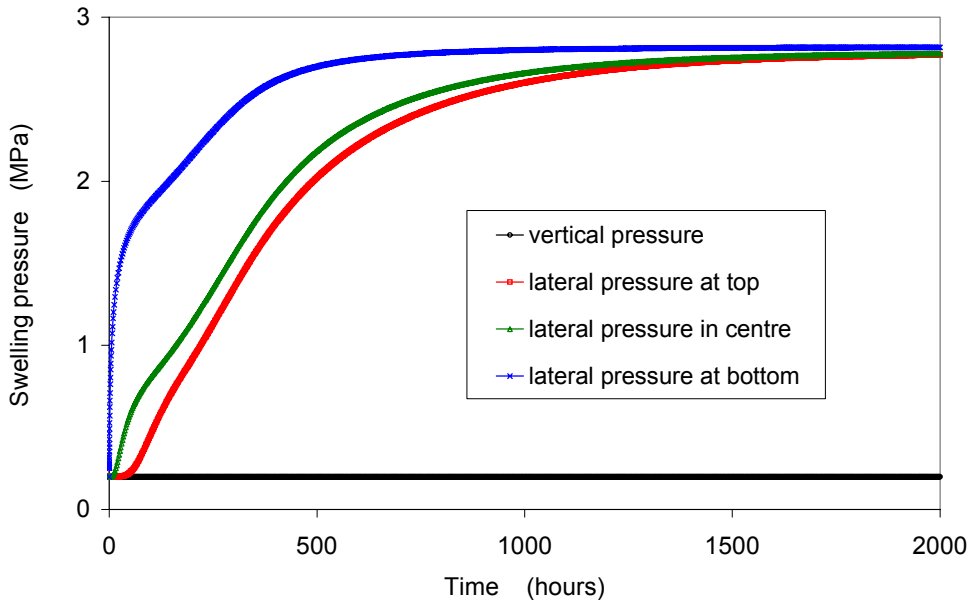

Figure 4.14 Swelling pressures during wetting

4.3.2 Consolidation and Collapse of Bentonite

When an unsaturated porous soil is wetted at a relatively high pressure, an irrecoverable volumetric compression (collapse) may occur. This phenomenon is examined by simulating a suction-controlled oedometer test on the Serrata bentonite. The initial conditions of the specimen are: porosity ϕ = 60 %, degree of saturation S_l = 21,6 %, suction s = 130 MPa. First, the specimen is compacted with a vertical strain rate of $5 \cdot 10^{-7}$ m/s until the vertical stress reaches 27.2 MPa. Then it is wetted at the bottom at constant stress. The oedometer conditions prescribed and the equations used are the same as in the swelling tests above.

The resulting stresses in different regions of the specimen are illustrated in Figure 4.15, whereas the evolution of the water saturation is given in Figure 4.16, the porosity versus time in Figure 4.17. The compaction results in a reduction of porosity, an increase in water saturation and in stress. Under the constant vertical stress of 27.2 MPa, wetting causes a collapse of the specimen from the bottom towards the top. The collapse causes a reduction in lateral stress. After the collapse, the specimen reaches stability at lower porosity. Figure 4.18 shows the consolidation curve during loading and wetting. The pattern of the curve is the same as that observed in the suction-controlled experiments /VOL 96/00/, /ALO 00/.

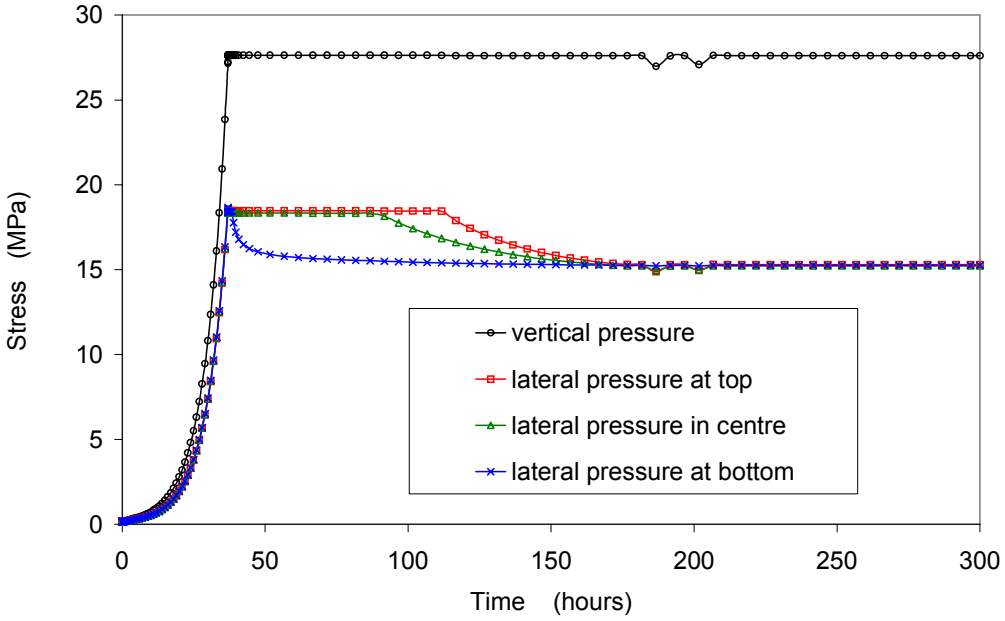

Figure 4.15 Evolution of stresses during compaction and wetting of bentonite

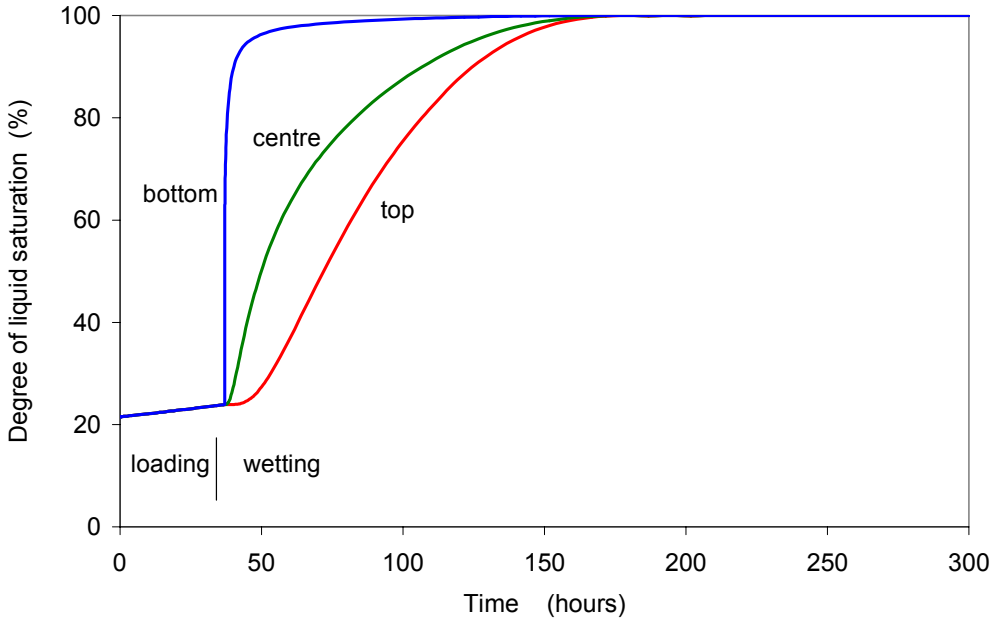

Figure 4.16 Evolution of water saturation during compaction and wetting of bentonite

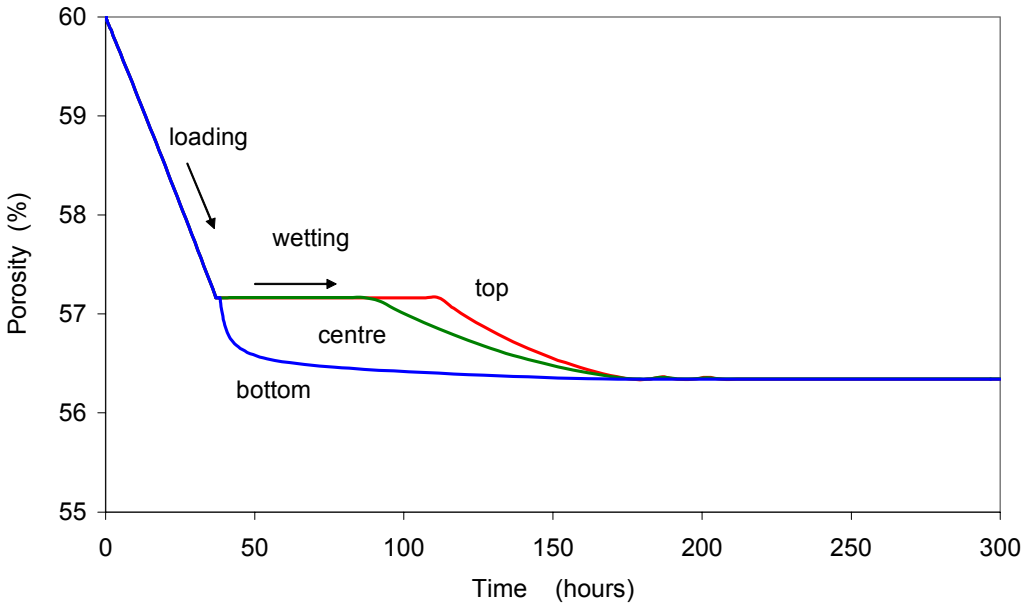

Figure 4.17 Porosity evolution during compaction and wetting of bentonite

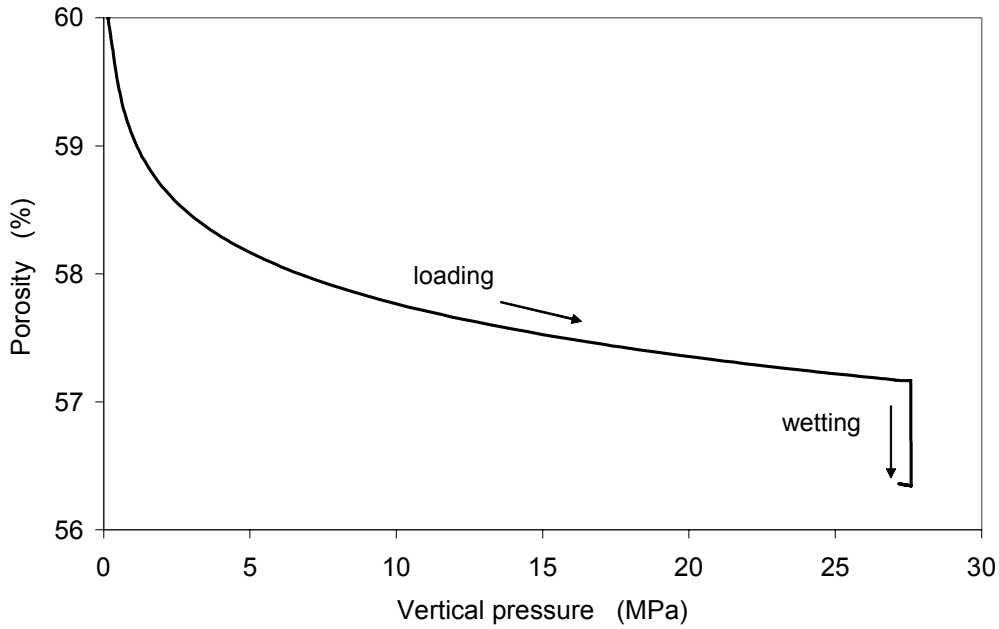

Figure 4.18 Consolidation behaviour during loading and wetting of bentonite

4.3.3 Resaturation of Bentonite

In the framework of the GRS-project „modelling of the hydration behaviour of bentonite" /KRÖ 03/, a series of hydration tests on MX-80 bentonite was conducted in the GRS geotechnical laboratory. The initially unsaturated specimens were confined in steel cylinders of 50 mm diameter and 100 mm length. A hydraulic pressure of 0.01 MPa was applied at the bottom of each specimen by using burettes. The other end was closed. The initial conditions of the specimens are: grain density ρ_s = 2800 kg/m^3, dry density ρ_d = 1520 kg/m^3, porosity ϕ = 45.7 %, degree of saturation S_l = 31.9 %. An isostatic stress state of $\sigma_1 = \sigma_2 = \sigma_3$ = 0.2 MPa is assumed for the modelling. The initial suction is calculated according to the retention curve obtained by wetting the Serrata bentonite, s = 60 MPa. During the tests, the specimens were not allowed to deform. The distributions of water content and density were determined after different durations by cutting the specimens into small discs and measuring their water contents and densities.

The hydration tests were blindly predicted by applying the material parameters of the Serrata bentonite. The hydration behaviour of the bentonite is assumed to be controlled by coupled THM effects. The equations solved are energy balance (Eq. 4.1), water mass continuity (Eq. 4.2) and stress equilibrium (Eq. 4.4). Air flow is not taken into account, whereas vapour flow is allowed, i.e. water diffusion exists. The same hydraulic and mechanical constitutive laws as applied for the modelling of the above swelling tests are adopted. Additionally, conductive heat flow (Eqs. 4.7 - 4.8) and molecular diffusion of vapour (Eqs. 4.17 - 4.18) are used, too. The retention curve (Eq. 4.16) for the wetting path is adopted.

Water saturation data measured on thin discs cut from the MX-80 specimens and the model results are compared in Figure 4.19. It is interesting to see that the resaturation behaviour of the MX-80 bentonite is quite well predicted for the first 10 – 20 days, and then somewhat overestimated on the long term. However, the general patterns of the measured and predicted distributions are very similar. A better prediction can be expected by adjusting the parameters to the studied material.

Due to the swelling of the bentonite during the wetting, the porosity is locally changed. From Figure 4.20 one can see that the resaturation results in local swelling in a region near the water inlet, causing the compaction in the remaining domain. The prediction

agrees well with the test results. The relatively high porosities measured at the inlet may be caused by volumetric expansion due to the distressing at the beginning of the discs cutting procedure.

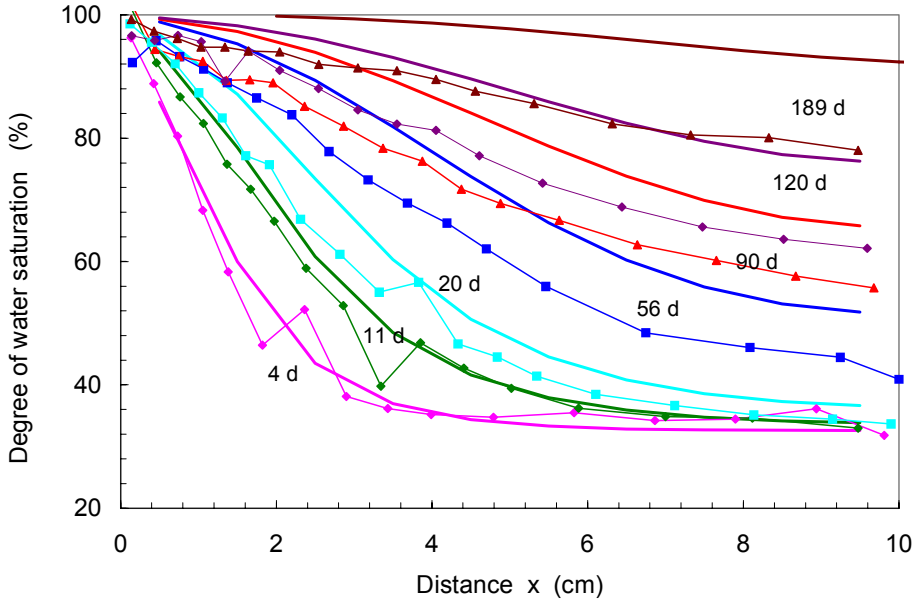

Figure 4.19 Comparison of water saturation measured on MX-80 bentonite (dotted-thin lines) and calculated for Serrata bentonite (thick lines)

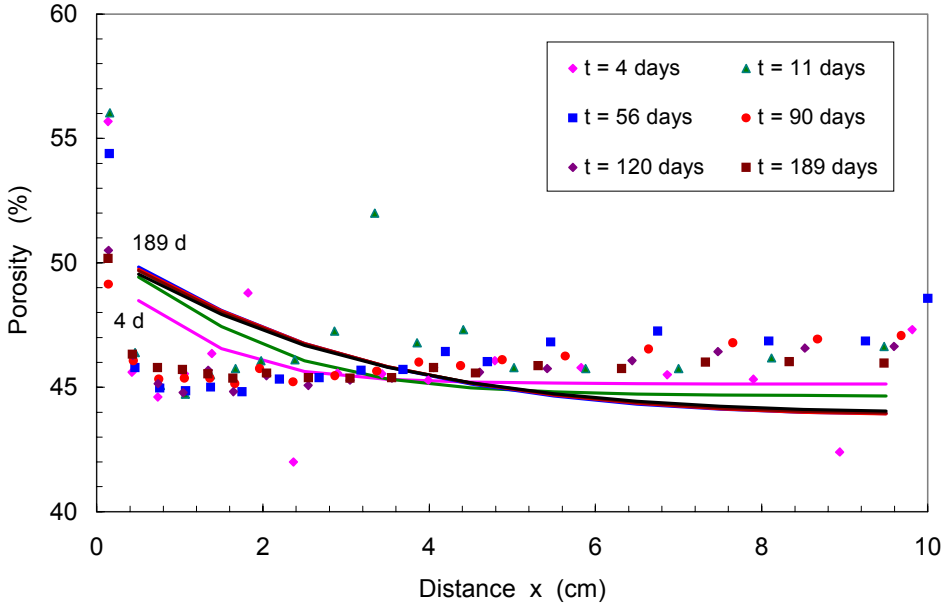

Figure 4.20 Comparison of porosity measured on MX-80 bentonite (points) and calculated for Serrata bentonite (thick lines)

4.3.4 Desaturation of Opalinus Clay

In the project „Ventilation Experiment in Opalinus clay" (VE-experiment), a laboratory drying test on Opalinus clay core samples was performed by AITEMIN /VE 02/. In the test, evaporation rates from three Opalinus clay specimens (D/L= 100/280 mm) were measured under controlled atmospheric conditions (T = 30 °C, RH = 26 – 40 %) inside a drying chamber. Evaporation took place by gas flowing along the top surface, whereas the bottom and lateral surfaces of the specimens were isolated (see Figure 4.21). The specimens were initially saturated. The drying test was simulated with CODE-BRIGHT by DM Iberia, in which thermo-hydro coupling was adopted. The parameters used for the Opalinus clay are summarized in Tables 4.1 and 4.2.

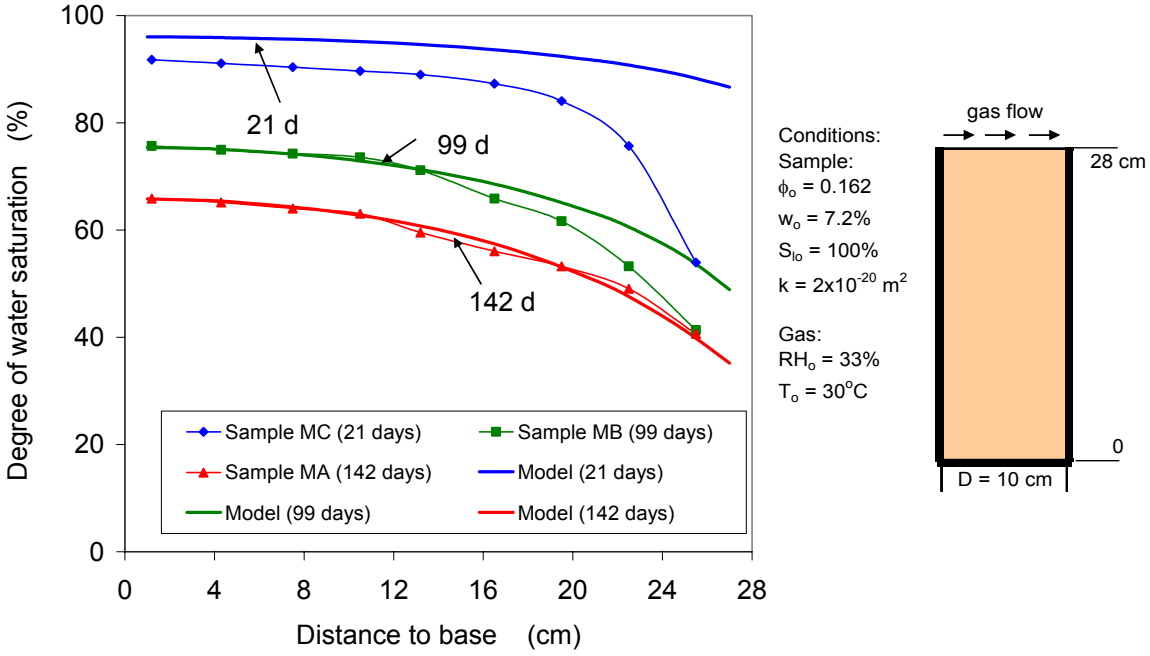

Figure 4.21 Comparison of water saturation in Opalinus clay samples observed in a drying test conducted by AITEMIN /VE 02/ and data calculated by GRS

The calculation performed by DM Iberia was repeated by GRS under the same conditions and by using the same parameters. However, the results of DM Iberia could not be represented by the GRS calculation. Therefore, some of the parameters were modified for further calculations, such as initial porosity ϕ_o = 16.2 %, the turbulence coefficient β_g = 6·10^{-5} m/s, P_o = 10 MPa and β = 0.45 for equation (4.16). The newly obtained results are compared with the test data in Figure 4.21. Generally, a good

agreement can be found. The desaturation near the top surface (h = 28 cm) of the specimens was very rapid in the first 20 days and then slowed down with time. At 99 and 142 days, a similar value of water saturation of 40 % was measured at the top surface. However, this observation could not be represented by the modelling, yet.

4.3.5 Response of Bentonite to Heating

To examine hydro-mechanical responses of clays to heating, a number of heating tests were carried out and numerically simulated by different authors by using different THM codes /MOH 96/, /VOL 96/, /THO 98/, /LI 98/, /KAN 99/ and /HUE 00/. In one of the heating experiments made by CIEMAT /VOL 96/, an unsaturated specimen of the Serrata bentonite was uniaxially compacted at an initial water content of 12.4 % to a dry density of 1.62 g/cm^3 in a stainless steel cell of 14.6 cm height and 15 cm inner diameter (Figure 4.22). A heater is placed at the centre of the top boundary. The temperature distribution within the specimen was measured by 9 thermocouples at different positions.

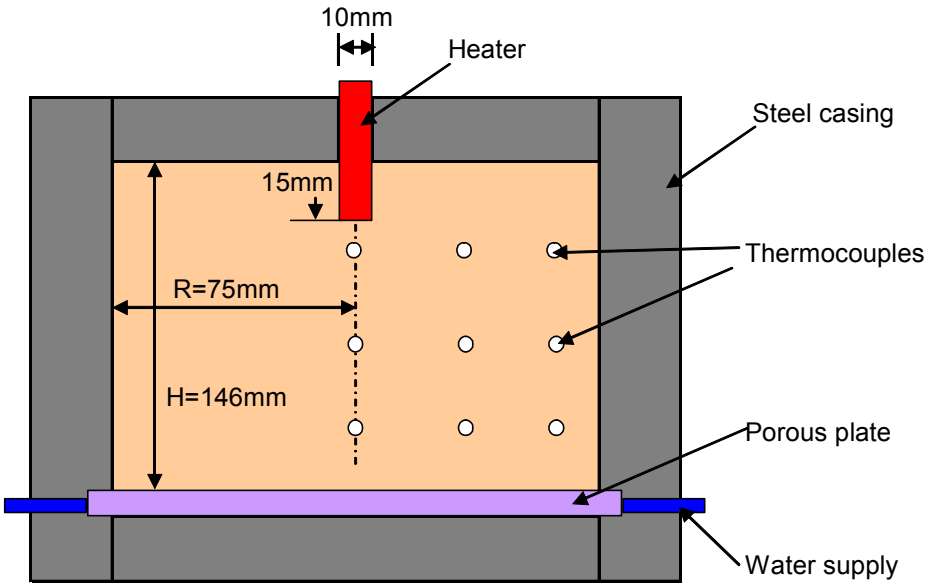

Figure 4.22 Thermo-hydraulic cell used in CIEMAT heating tests /VOL 96/

This experiment was also simulated by GRS for modelling the coupled heat, moisture and air transfer in clay, by using the parameters of the Serrata bentonite. Due to

symmetry, only half of the specimen is used for the axisymmetric analysis. The heater is simulated by two stiff edge lines.

In the test vertical and horizontal boundaries are fixed. The initial conditions of the test are given as: T_o = 28 °C, ϕ_o = 42.6 %, S_{lo} = 53.0 %, P_{go} = 0.1 MPa, P_{lo} = -130 MPa, $\sigma_1 = \sigma_2 = \sigma_3$ = 0.2 MPa. All boundaries are impermeable. The temperature of the heater is specified as 100 °C. The temperature along the outside boundaries is fixed at 28 °C.

Additionally, to examine the coupled THM processes in saturated conditions, a second test on an initially saturated specimen was assumed and calculated as well. The initial conditions of the second test are given as: T_o = 28 °C, ϕ_o = 42.6 %, S_{lo} = 100 %, P_{go} = 0.1 MPa, P_{lo} = 0.1 MPa, $\sigma_1 = \sigma_2 = \sigma_3$ = 5 MPa.

Drained conditions by applying a water back pressure of 0.1 MPa at the bottom are assumed for the second test. The temperature of the heater is fixed at 100 °C and the temperature along the outside boundaries at 28 °C. The initially applied high compressive stresses of 5 MPa are necessary to overcome high tensile stresses caused by high pore water pressures thermally-induced during the heating. In case tensile stresses exceed the tensile strength of the specimen, computing stops.

4.3.5.1 Response of Unsaturated Bentonite to Heating

After about 1 hour of suddenly imposed heating, steady state temperature distribution is reached in the computing. Figure 4.23 shows the distribution of temperature in the specimen after 200 hours. This result is well comparable with the experiment made by CIEMAT and the numerical results of /THO 98/, /VOL 96/, using the code COMPASS. The heat is gradually transferred away from the heater to the regions near the outside boundaries, forming the temperature gradient.

The heating induces moisture migration away from the heater to the outside boundaries (Figure 4.24). Consequently, the degree of water saturation around the heater is lower than in the other regions.

Heating results in changes in stress and suction, and hence in porosity. Figure 4.25 gives the distribution of porosity in the specimen after 200 hours heating. It can be seen that small shrinkage takes place near the heater and small swelling occurs in the

regions near the bottom. In this case, the thermal expansion effects are less than the shrinkage induced by stress and suction changes around the heater. This result does not agree with the experimental observations of CIEMAT /VOL 96/. The difference might be induced by the material parameters related to temperature, suction and stress in the models.

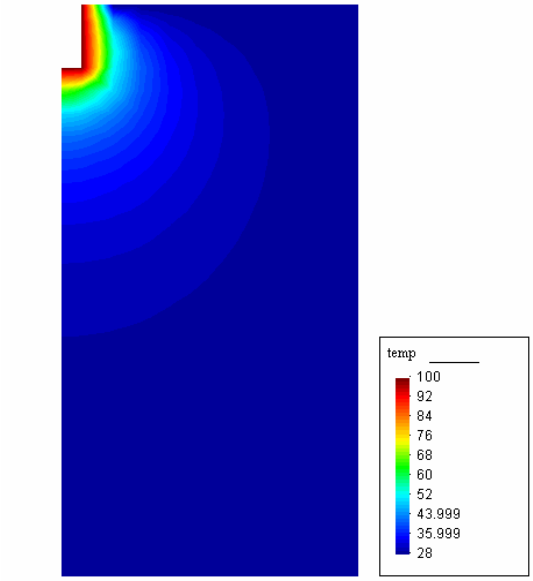

Figure 4.23 Distribution of temperature in the specimen after 200 hours heating

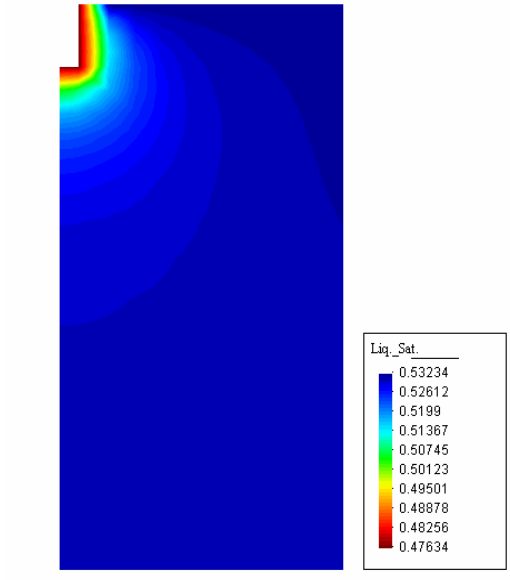

Figure 4.24 Distribution of water saturation in the specimen after 200 hours heating

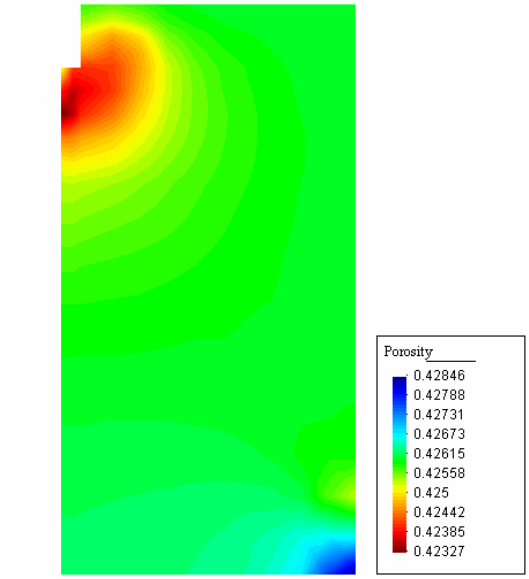

Figure 4.25 Distribution of porosity in the specimen after 200 hours heating

4.3.5.2 Response of Saturated Bentonite to Heating

The driving effect of temperature in a clay mass is the thermal expansion of the pore water /PEL 99/. In the heating test on the initially saturated specimen under drained conditions, suddenly elevating temperature of the heater results in a sudden evaporation of liquid water around the heater and then a rapid increase in pore water pressure due to the difference in thermal expansion between the solid particles and the pore water under confined conditions.

The temperatures at some typical points in the specimen are shown in Figure 4.26, while the time evolution of pore water pressure at the same points is depicted in Figure 4.27. After a short time of heating, the pore water pressure rises to a maximum value of about 2.5 MPa near the heater due to the low permeability which does not allow the pore pressure so fast to disperse. The pore water pressure reduces gradually to a steady state due to the drained conditions. Because of the mechanically confined boundary conditions, the variations in total stress correspond to the change in pore water pressure (compare Figure 4.27 and 4.28). The changes in stress and pore water pressure directly cause the variations of porosity in different regions shown in Figure 4.29. The region near the heater is first thermally expanded and then compacted at relatively high effective stresses (total stress minus water pressure). In contrast to this, the region near the bottom is first compacted by the expansion of the heated region and then expanded due to the reduction of the effective stresses. The distribution of temperature in the saturated specimen is similar to the pattern in the unsaturated specimen modelled above.

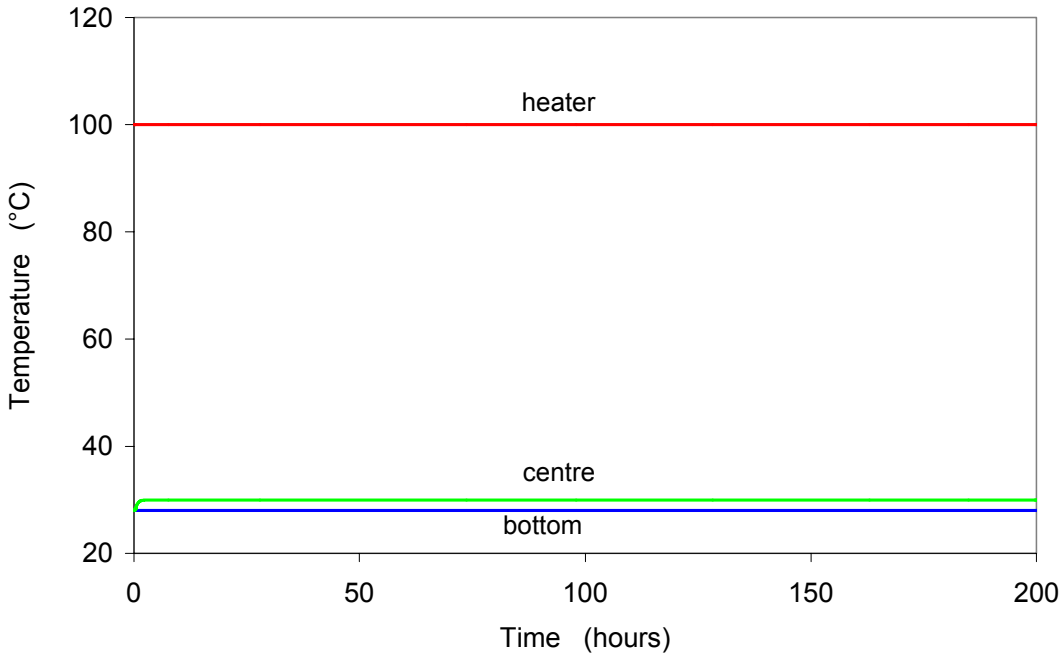

Figure 4.26 Evolution of temperature during heating of bentonite

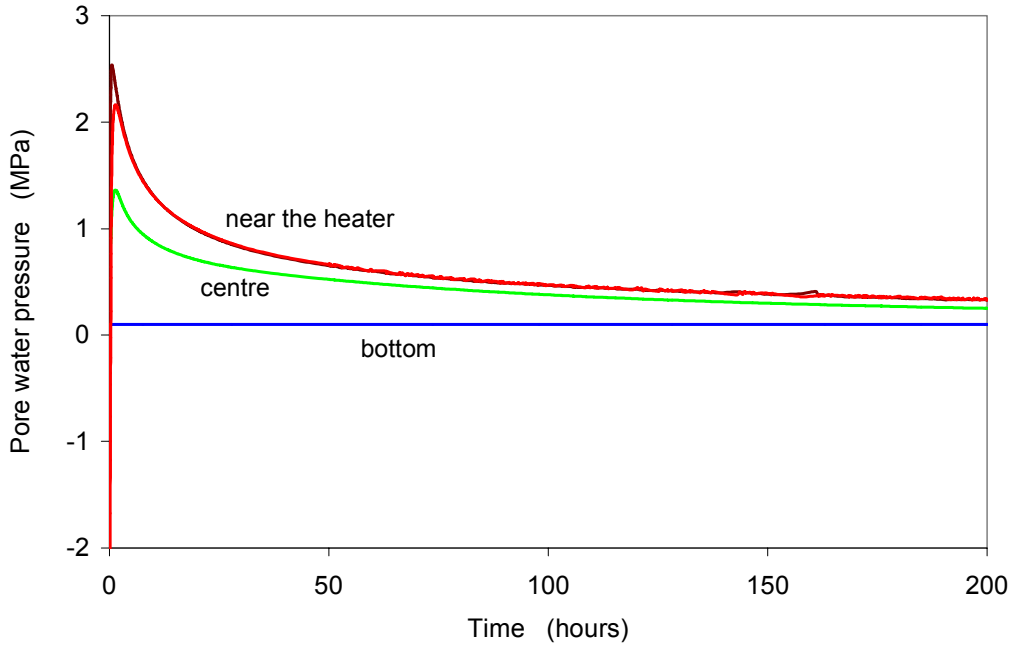

Figure 4.27 Evolution of pore water pressure during heating of bentonite

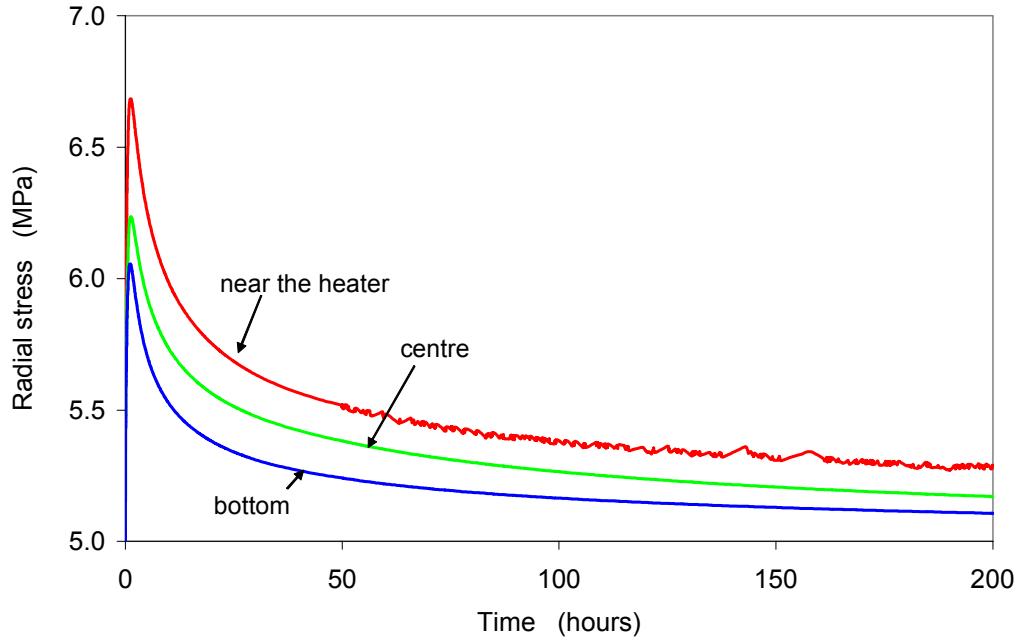

Figure 4.28 Evolution of lateral stress during heating of bentonite

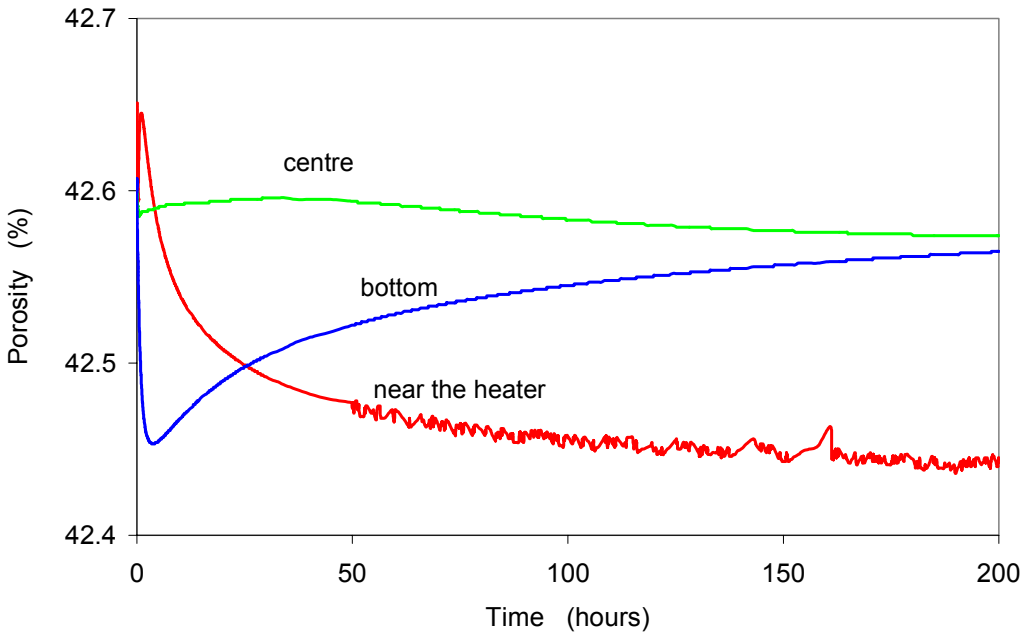

Figure 4.29 Evolution of porosity during heating of bentonite

4.4 Predictions of Large-Scale Laboratory Experiments

Full-scale *in situ* experiments provide the possibility of the observations of coupled THM effects in host rocks and engineered barriers. However, because the prevailing processes are usually not well known, the interpretation of the experimental results and the validation of theoretical models are difficult. Large-scale laboratory experiments can bridge the gap between laboratory results obtained on small-scale specimens and *in situ* results, because large samples can more realistically represent the rock mass *in situ*, testing conditions can be well defined, and THM processes can be monitored by instruments installed inside and outside of the samples.

Such large-scale THM experiments can be performed at the GRS geotechnical laboratory in the big triaxial MTS-testing apparatus, which allows a maximum specimen size of 27 cm diameter and 70 cm length. Taking relevant disposal concepts and *in situ* conditions in clays into account, GRS has proposed two large-scale laboratory experiments to be carried out:

- *Ventilation of a borehole in clay* to examine its hydro-mechanical responses to desaturation and resaturation, thereby supporting the ongoing ventilation experiment in the Opalinus clay – VE Experiment /VE 02/;
- *Heating of a rock-buffer-system* to study coupled THM processes developing in the clay rock and in the buffer, with special respect to the interaction between clay rock and bentonite, hereby supporting the HE-B Experiment – THM processes in the near field /HEB 02/.

In order to gain preliminary knowledge about the THM processes prevailing in the large samples, scoping calculations were performed.

4.4.1 Ventilation of a Borehole in Clay

After the excavation of underground openings, they are ventilated for couple of years before backfilling and sealing. Due to the excavation and ventilation, coupled hydro-mechanical processes take place in the surrounding rock. The resulting desaturation in the rock may have an important effect on its hydro-mechanical behaviour. Particularly, desaturation in clay may give rise to cracking and to extension of the excavated damage zones (EDZ) surrounding the drifts. After backfilling and sealing, however, the rock will be resaturated by the ground water. The EDZ will heal due to the swelling of

clay minerals and the support effects of backfill and seal. The ongoing VE ventilation experiment at the Mont Terri URL /VE 02/ focuses on investigation of the *in situ* desaturation and its effect on the extension of the EDZ in the Opalinus clay. Accompanying the *in situ* experiment phase II, GRS has proposed to conduct a laboratory ventilation test on large samples from the Opalinus clay.

Figure 4.30 shows the scheme of the laboratory ventilation test with a sample of 27 cm diameter and 70 cm length, in which a central borehole of 10 cm diameter is drilled. The saturated sample can be mechanically loaded by applying axial and radial stress and can also be desaturated by ventilating air through the borehole. The hydro-mechanical responses of the sample to the ventilation can be monitored by measurements of water content distribution, air humidity, stress and deformation etc. during the test.

Testing conditions

The following test conditions were assumed in the scoping calculations. First, the initially saturated sample will be externally loaded in radial direction to 12 MPa at the outside boundary by maintaining null vertical deformation. Under the applied mechanical conditions, the borehole in the sample will be ventilated by circulating gas with a relative humidity of 20 % for 500 days, assuming the turbulence coefficient $\beta_g = 10^{-4}$ m/s. After that, the sample will be resaturated by circulating water vapour through the borehole for 2500 days. such very long durations of the desaturation and resaturation phases, however, can not be realized in the test. Here, only two to three months for each phase will be adopted. Due to symmetry, only half of the sample is considered in the axisymmetric analysis. THM coupling is adopted in the calculations by solving the same equations as in the modelling of the hydration test in chapter 4.3.3. Diffusive vapour flow through the sample is taken into account, but air flow is not considered.

Results

Figure 4.31 shows the stress distribution in the sample along the radius at the mid-height after the loading phase. The radial loading results in an increase in the vertical stress due to the fixed deformation in this direction. The circumferential stress is higher than the vertical and radial stresses. The high deviatoric stresses concentrated on the

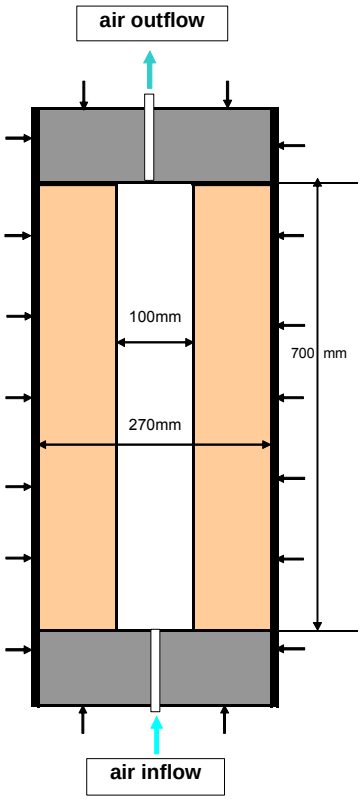

material: Opalinus clay

specimen: D = 27 cm, d = 10 cm, L = 70 cm
porosity ϕ = 16 %
degree of water saturation S_l = 100 %

Initial conditions:
stresses $\sigma_1 = \sigma_2 = \sigma_3$ = 0.2 MPa
water pressure P_l = 0.1 MPa
gas pressure P_g = 0.1 MPa
temperature T = 20 °C

1. loading:
inner wall: support stress σ_r = 0.2 M Pa
air relative humidity RH = 20 %
turbulence coefficient β_g = $1 \cdot 10^{-4}$ m/s
outer wall: strain rate $\dot{\varepsilon}_r$ = $1.2 \cdot 10^{-7}$ 1/s
radial stress σ_r = 0.2 → 12.0 MPa
no water outflow through the outer wall

2. desaturation:constant mechanical conditions after the loading
air relative humidity RH = 20%
turbulence coefficient β_g = $1 \cdot 10^{-4}$ m/s

3. resaturation: constant mechanical conditions after the loading
air relative humidity RH = 100%
turbulence coefficient β_g = $1 \cdot 10^{-4}$ or 10 m/s

Figure 4.30 Scheme of the proposed large-scale ventilation test

inner wall causes the material yielding. In this region, the porosity increases, indicating possible material damage. However, the influence of the following desaturation on the porosity is negligible (Figure 4.32). Possible initiation and evolution of any damaged zone (EDZ) could not be modelled by the used version of CODE-BRIGHT. The convergence of the borehole is plotted in Figure 4.33, indicating negligible effects of the desaturation and resaturation on the mechanical deformation.

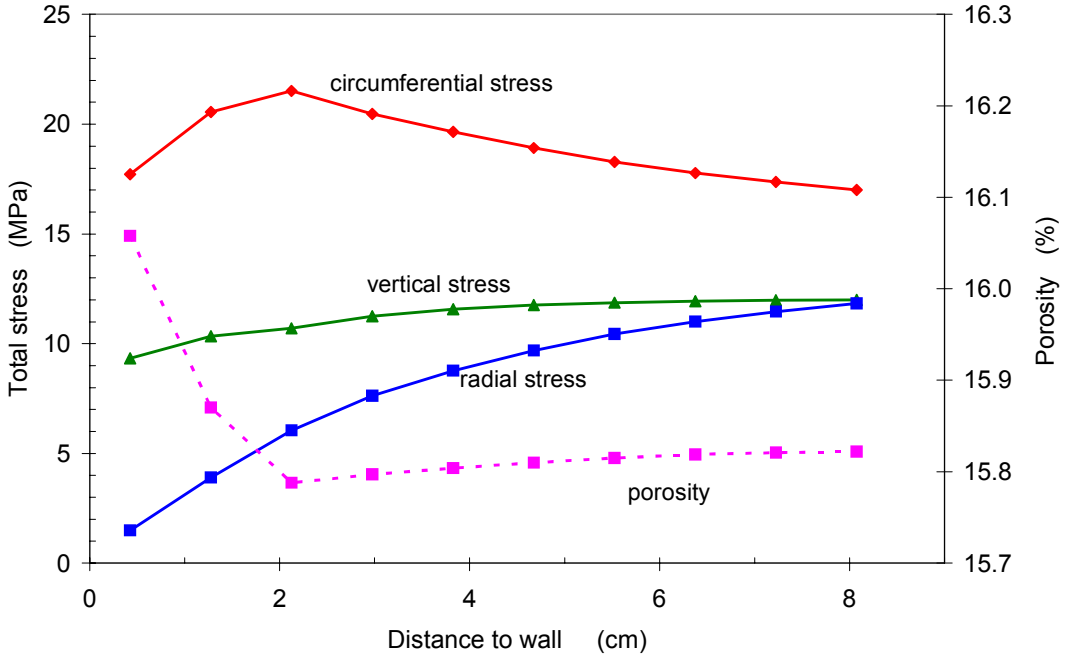

Figure 4.31 Stress and porosity distribution in the hollow sample after loading

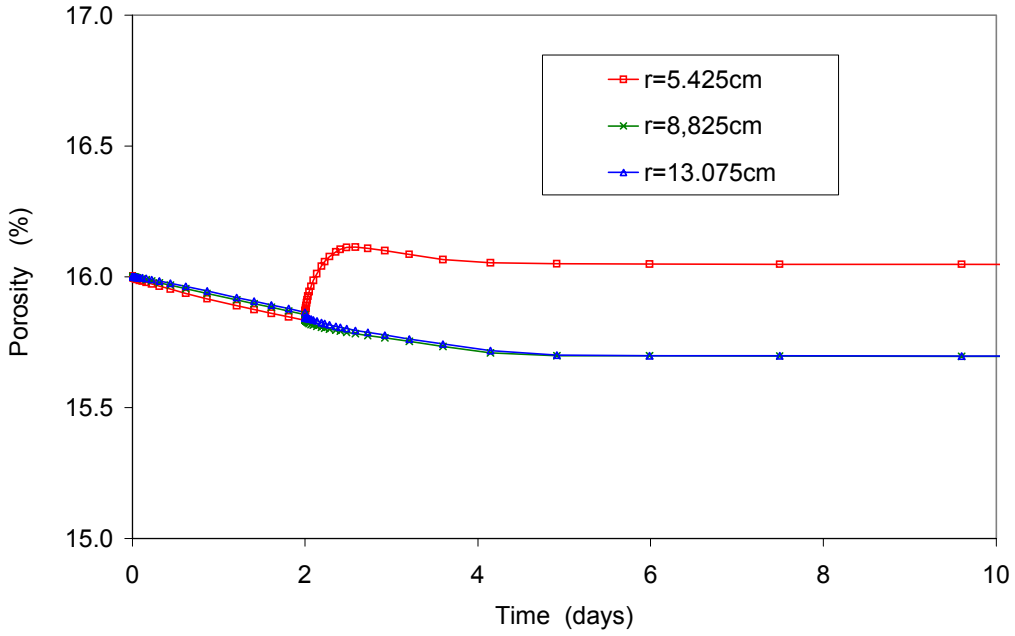

Figure 4.32 Evolution of porosity in the hollow sample

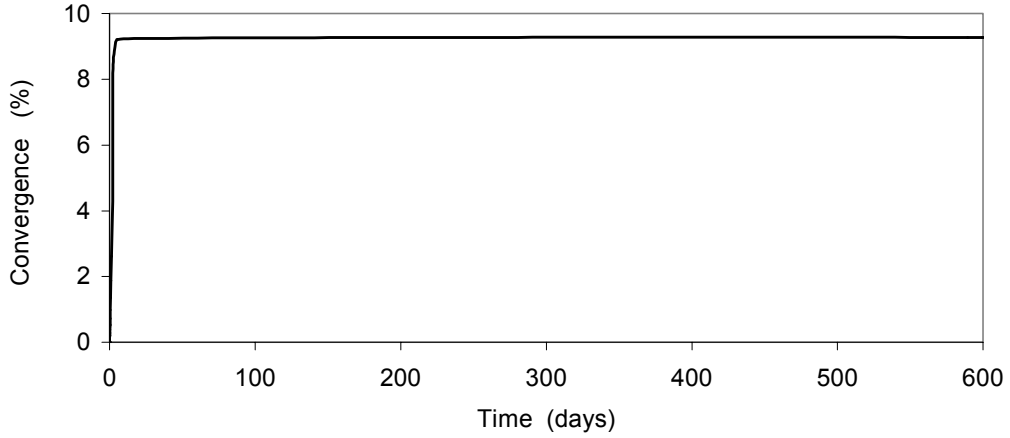

Figure 4.33 Evolution of the borehole convergence

The desaturation and resaturation at different radii are shown in Figure 4.34. After 500 days of desaturation, the degree of water saturation in the specimen attains 24 % - 26 %. The resaturation time is strongly dependent on the turbulence coefficient of the gas flow on the wall. By adopting the high turbulence coefficient of β_g = 10 m/s, a nearly full resaturation with 99 % water saturation is achieved in about 100 days, while by using β_g = 10^{-4} m/s the resaturation needs about 2000 days. Full resaturation to 100 % needs longer times.

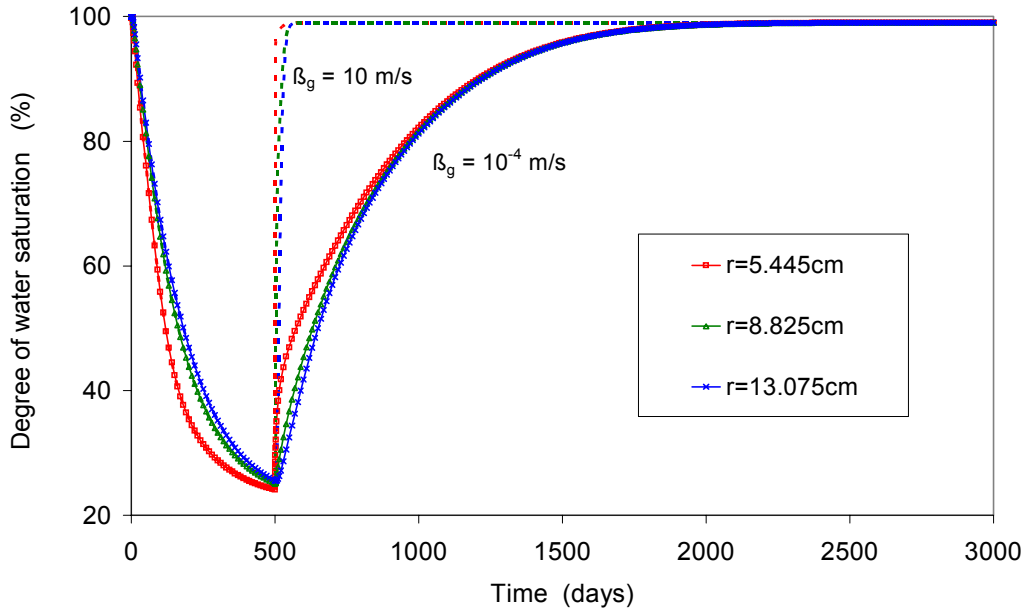

Figure 4.34 Desaturation and resaturation of the hollow sample

4.4.2 Response of Rock-Buffer-System to Heating

In the multi-barrier concepts for disposal of high level radioactive wastes (HLW) in granite and clay formations, the HLW-canisters will be placed in drifts or boreholes, and surrounded by a buffer made of compacted bentonite blocks to fill the space between the canisters and the host rock. Usually, the host rock is saturated by ground water. After emplacement, the initially unsaturated buffer takes up water from the host rock. The interaction between buffer and host rock leads to complex coupled THM processes in the near- and far-field for very long periods of time.

Testing conditions

To study the THM processes in the near-field, GRS has proposed a laboratory heating experiment with a large rock-buffer-sample under relevant *in situ* conditions. Figure 4.35 shows the general scheme of the experiment. The rock-buffer-sample consists of a hollow cylinder of clay rock and a bentonite buffer filling the borehole. The hollow cylinder has a length of 60 cm and an outer diameter of 26 cm. The borehole diameter is 10 cm. Relevant *in situ* stress conditions can be applied to the sample by axial and lateral loading. Simulating the groundwater *in situ*, water can be supplied to the sample through the filters around the outside boundary. The rock-buffer-sample can be heated by a heater installed in the buffer, simulating the heat-generating waste canister.

The hollow cylinder will be taken from the Opalinus clay or the Callovo-Oxfordian argillite, while expansive bentonite will be used as buffer material. The rock is initially saturated, whereas the buffer is unsaturated. The test will be carried out in five stages:

(1) In the first stage, the rock-buffer-sample will be isotropically compressed up to 11 MPa at ambient temperature of 20 °C, and simultaneously, water will be externally supplied at an injection pressure of 2 MPa. During the test, gas is enclosed in the rock-buffer-system.

(2) In the second stage, the sample will be consolidated and resaturated under the applied conditions for 30 days.

(3-4) After that, the rock-buffer-sample will be heated in two steps by applying heat flow of 3 kJ/s/m and 5 kJ/s/m. Each stage will last for 30 days.

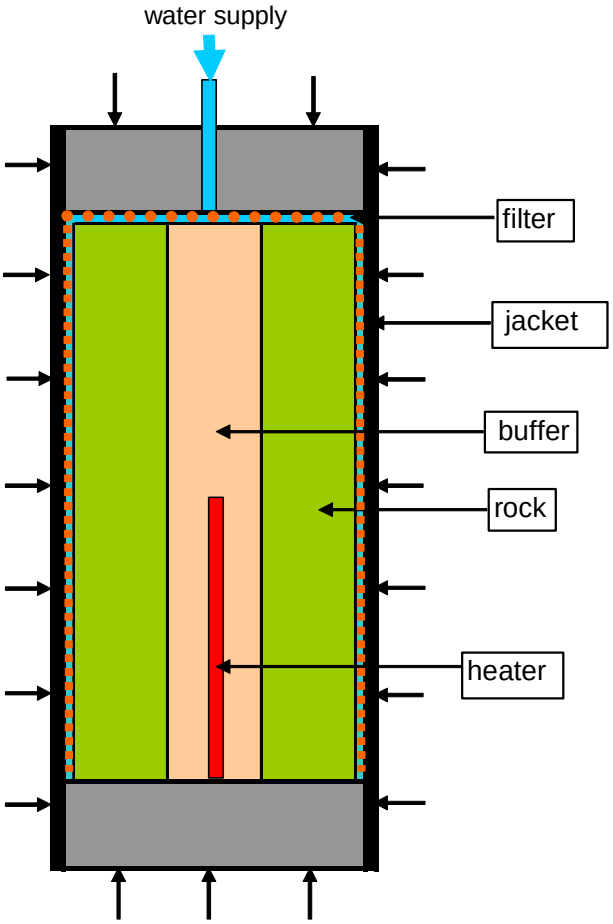

Figure 4.35 General scheme of laboratory heating experiment on rock-buffer-sample

(5) In the last stage, the heater will be shut off and the sample will cool over 30 days.

For the envisaged test, scoping calculations were performed with simplified assumptions of homogeneous and isotropic properties of the materials by solving the following equations: balance of energy, balances of water, air and solid mass, and stress equilibrium. In the calculations, various physical phenomena were taken into account:

(1) heat transport is dominated by conduction (Fourier's law) through the media and by advection of liquid water and vapour flow;

(2) water flow is controlled by advection (Darcy's law), vapour diffusion in air (Fick's law) and phase changes (psychrometric law);

(3) air and vapour are considered to behave as ideal gases, and air flow is controlled by advection (Darcy's law) and solution in liquid water (Henry's law);

(4) the mechanical behaviour of both materials are described by the BBM elasto-plastic model, with the main features of swelling and thermal expansion.

For the calculations, an axisymmetric sample geometry has been adopted. Figure 4.36 shows the model geometry and initial / boundary conditions. The heater is simulated by two stiff edge lines. The Opalinus clay and the Serrata bentonite are adopted for the hollow cylinder and for the buffer, respectively. The parameters of both materials are given in Tables 4.1 and 4.2. It can be expected that the applied conditions to the rock-buffer-system give rise to a series of THM phenomena that interact with each other in a complex way. Along the middle cross section of the heated area, some typical points are selected for the evaluation of the results: buffer near heater (r = 1 cm), buffer near rock (r = 4 cm), rock centre (r = 9 cm) and rock outer boundary (r = 13 cm).

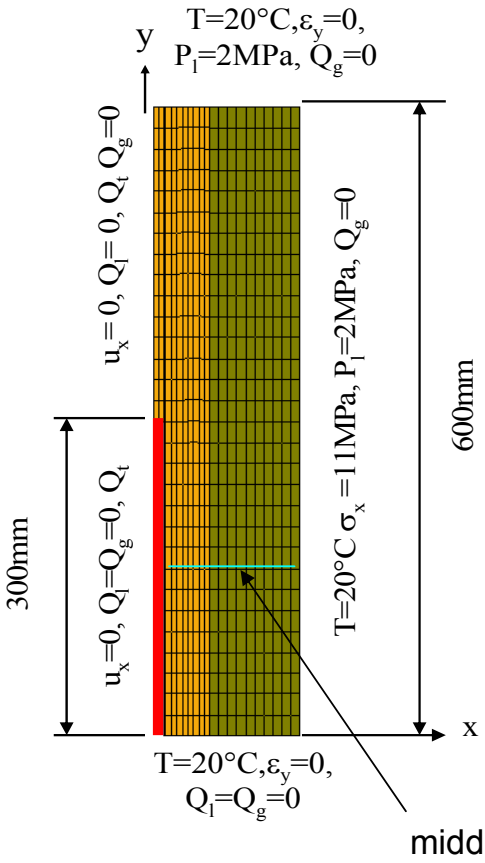

Initial Conditions

Clay rock:	ϕ = 16%,	S_l = 100%,	k = $2 \cdot 10^{-20}$ m²
Bentonite:	ϕ = 42.6%,	S_l = 22%,	k = $6 \cdot 10^{-21}$ m²

T = 20°C, $P_l = P_g$ = 0.1 MPa, $\sigma_1 = \sigma_2 = \sigma_3$ = 1 MPa

Boundary conditions

Stage	Time (days)	Thermal	Hydraulic	Mechanical
1. Compression Hydration	0 → 0.4	T = 20°C	P_l = 2 MPa ΔQ_g = 0	$\sigma_1 = \sigma_2 = \sigma_3$ = 11 MPa
2. Consolidation Hydration	0.4 → 30	=	=	=
3. Heating 1	30 → 60	T_B = 20°C Q_T=3000J/s/m	=	=
4. Heating 2	60 → 90	T_B = 20°C Q_T=5000J/s/m	=	=
5. Cooling	90 → 120	T_B = 20°C Q_T = 0 J/s/m	=	=

Figure 4.36 Model geometry and initial / boundary conditions

Results

Thermal aspect

The temperature distribution reached at the end of the first and second heating phase are illustrated in Figure 4.37. The heat is gradually transferred away from the heater to the regions near the outside boundaries, forming the temperature gradient. The constant heat supply generates a rapid increase in temperature. The elevated temperature becomes constant after a short time, as shown in Figure 4.38, in which the temperature evolution for the selected points is depicted. The heat supply with 3 kJ/s/m gives a rise in temperature on the heater surface to 77 °C and the higher heat flow of 5 kJ/s/m rises the temperature to 111 °C. In consequence of the sudden cooling, the temperature drops quickly down to the initial value of 20 °C in the whole sample, so that the thermal gradient is eliminated. The buffer hydration and the rock dehydration seem to have no significant influences on the temperature development.

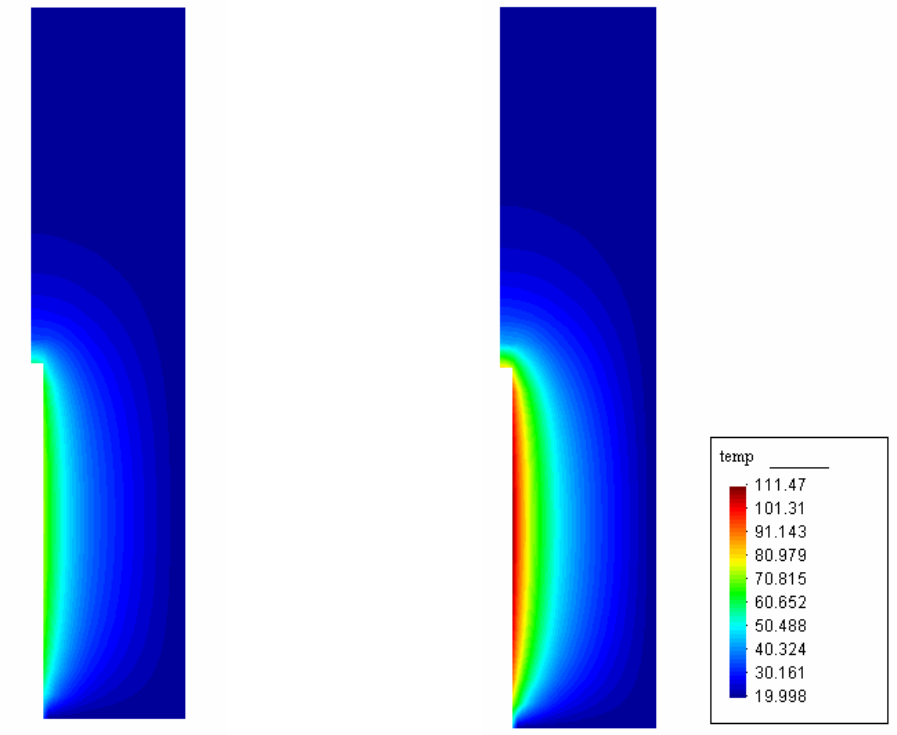

at the end of the 1st heating phase at the end of the 2nd heating phase

Figure 4.37 Distribution of temperature

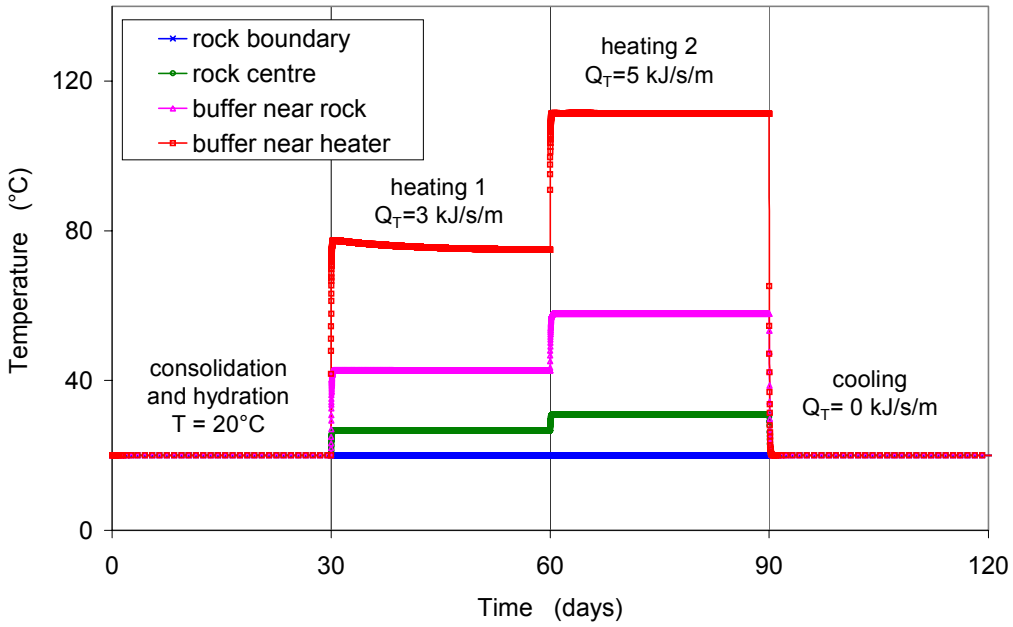

Figure 4.38 Evolution of temperature at selected points

Hydraulic aspect

The distribution of water saturation in the rock-buffer-sample is shown in Figure 4.39 for the initial state (t = 0), the end of the isothermal hydration (t = 30 days) and the end of the first heating phase (t = 60 days), while the evolution of water saturation at the selected points is illustrated in Figure 4.40. By the effect of high suction, the buffer near the rock takes up water quickly from the initially saturated rock. Consequently, the rock near the buffer is desaturated. With continuing water supply, the degree of water saturation in the unsaturated regions is gradually increased. However, a full resaturation of the buffer near the heater can not be achieved during the heating phase, obviously because of the presence of high gas concentration near the heater. After the elimination of the thermal gradient in the cooling phase, the buffer is fully resaturated by the combined effects of vapour condensation and external water supply.

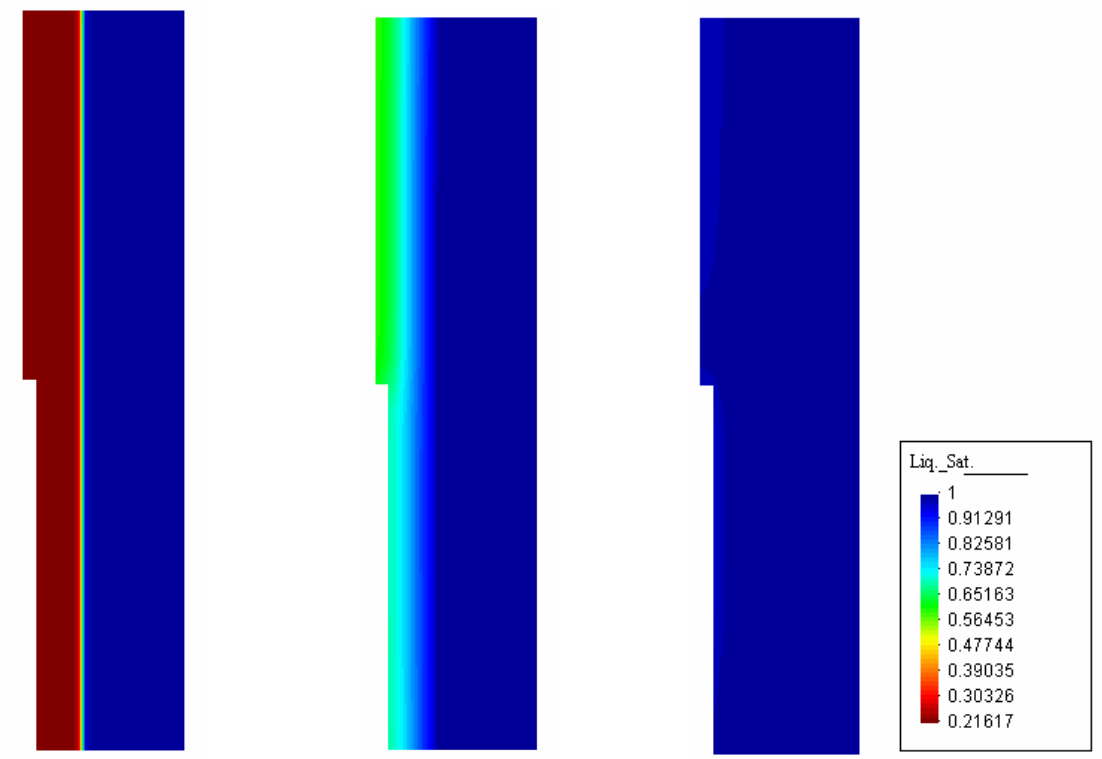

initial saturation after the isothermal hydration after the 1st heating phase

Figure 4.39 Distribution of water saturation

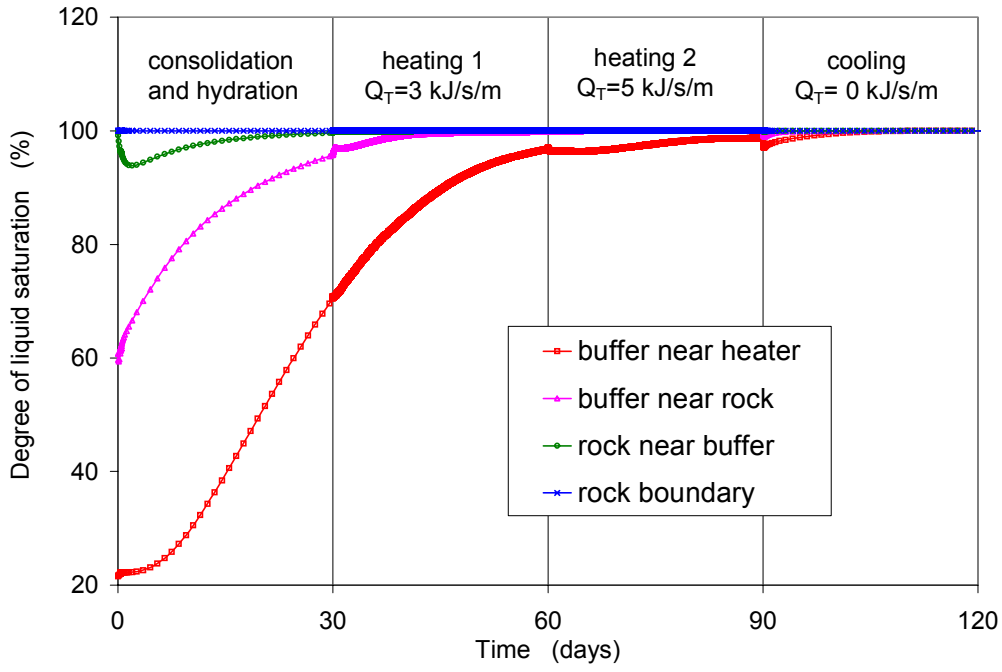

Figure 4.40 Evolution of water saturation at selected points

Figure 4.41 shows the evolution of the pore water pressure at the selected points. The mechanical compression to 11 MPa results in a peak pore water pressure to 3.3 MPa in the central part of the saturated rock, which is then quickly reduced to a negative value of -1.6 MPa by effect of buffer suction. The continuous water injection resaturates the rock and increases the water pressure again. The first heating phase gives rise to a peak water pressure in the saturated region, which then falls rapidly down to the original value, whereas the pore water pressure in the unsaturated buffer evolves from negative to positive values. The thermally-induced peak water pressures in the saturated regions are due to the differences in thermal expansion of liquid, gas and solid. Under the drained conditions, the thermally-induced peak water pressure decreases gradually to a steady state. The sudden cooling induces a rapid contraction of the pore water, and therefore, the pore water pressure falls quickly down. The external water injection increases the pore water pressure again to an equilibrium at the pressure applied on the outside boundaries.

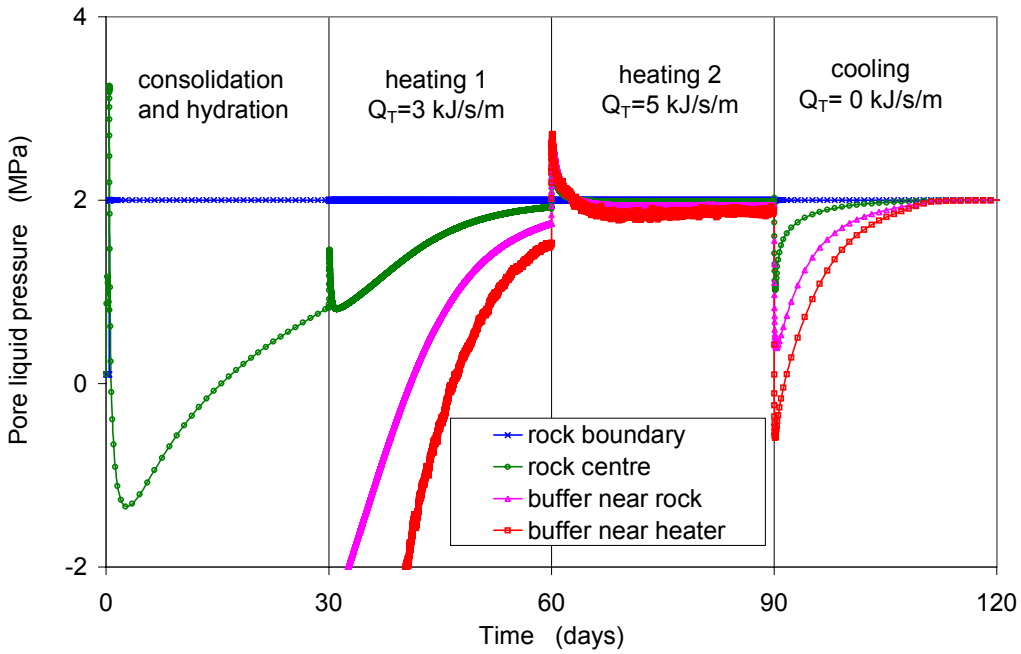

Figure 4.41 Evolution of pore water pressure at selected points

During the test, gas is enclosed in the rock-buffer-system. Therefore, the intrusion of the external water into the unsaturated regions reduces the pores occupied by gas, hereby rising gas pressure. This can be clearly seen from the isothermal hydration phase of the time evolution curves of the pore gas pressures at the selected points in Figure 4.42. The sudden heating causes peak gas pressures by the combined effects

of the thermal expansion potential of the gas itself and the pore compaction caused by the thermal expansions of the pore water and the solid grains. The peak gas pressures decrease to steady state with decreasing pore water pressures. It is to be noted that the peak gas pressure near the heater is higher than the thermally-induced water pressure, but lower than the total stress. The high gas pressure may drive the water flow outwards. If the gas pressure is higher than the total stress, it can be expected that hydrofracturing can occur in the rock-buffer-system. With the gas migration away from the hot region to the cool region, the peak gas pressure decreases gradually. But the gas pressure near the heater is still higher than in other regions. The sudden cooling results in a rapid contraction of the pore gas, hereby reducing the pore gas pressure. After that, the gas pressure is increased again by the water flow into the voids occupied by gas, finally reaching an equilibrium at a pressure of 1.9 MPa which is little lower than the water pressure of 2 MPa.

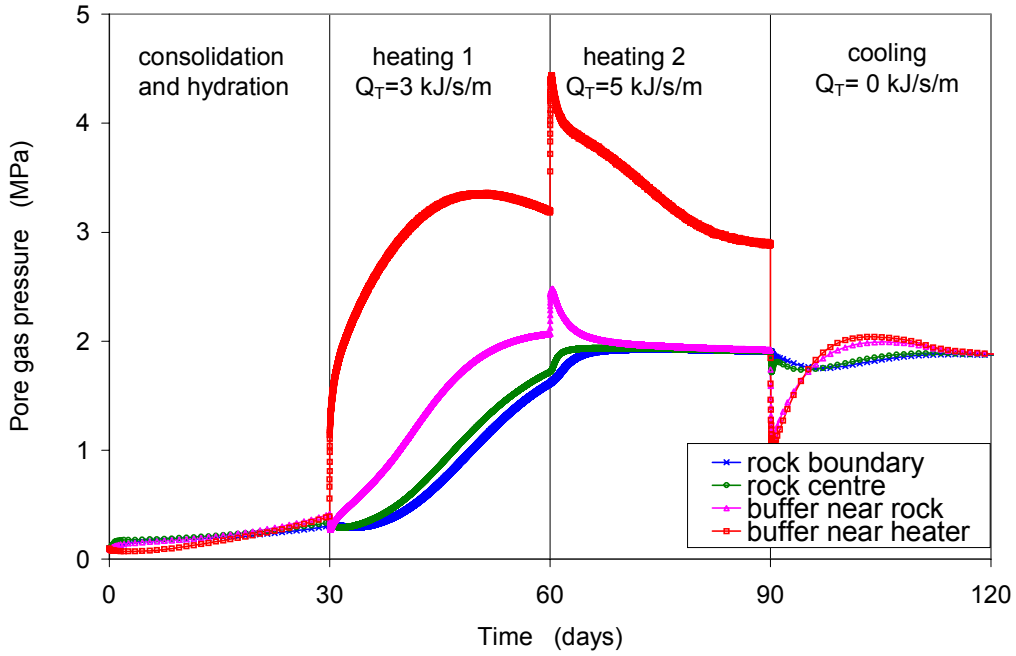

Figure 4.42 Evolution of pore gas pressure at selected points

Mechanical aspect

The mechanical compression causes changes in stress state in the rock-buffer-system. Figure 4.43 shows the distribution of the total stresses at the end of the mechanical loading and the end of the second heating phase, while in Figure 4.44 the time

evolution of the radial stress at the selected points is illustrated. It is obvious that the stresses are highly concentrated on the inner wall of the rock cylinder. With increasing hydration, swelling pressure builds up in the bentonite buffer and reaches the maximum value as full resaturation is achieved. It can clearly be seen that after the sudden compression, the development of the stress state in the rock is controlled by the swelling pressure in the buffer. The deviatoric stress in the rock reduces due to the reaction of the buffer swelling which increases the radial stress in the rock. The sudden heating and cooling generate transient changes in total stresses. However, the long-term stress states reached in the rock and in the buffer seem to be not affected by the heating and cooling phases.

The evolution of the radial displacements of the selected points is shown in Figure 4.45. The mechanical compression results in a displacement increase in the rock and in the buffer. With increasing hydration, the buffer expanses gradually outwards to the rock. The buffer expansion together with the gradual increase in the effective stress in the rock causes a continuous back-deformation of the rock. After reaching the stress equilibrium in the rock-buffer-sample, the rock and the buffer cease to deform. Heating and cooling generate only transient changes in deformation.

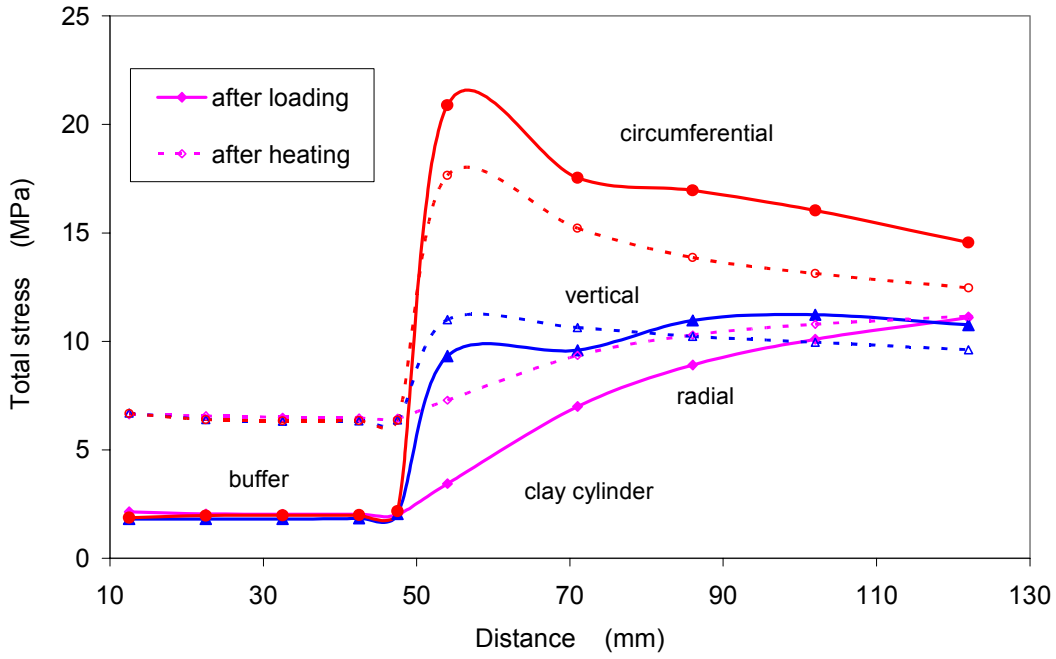

Figure 4.43 Distribution of total stresses along the middle cross section

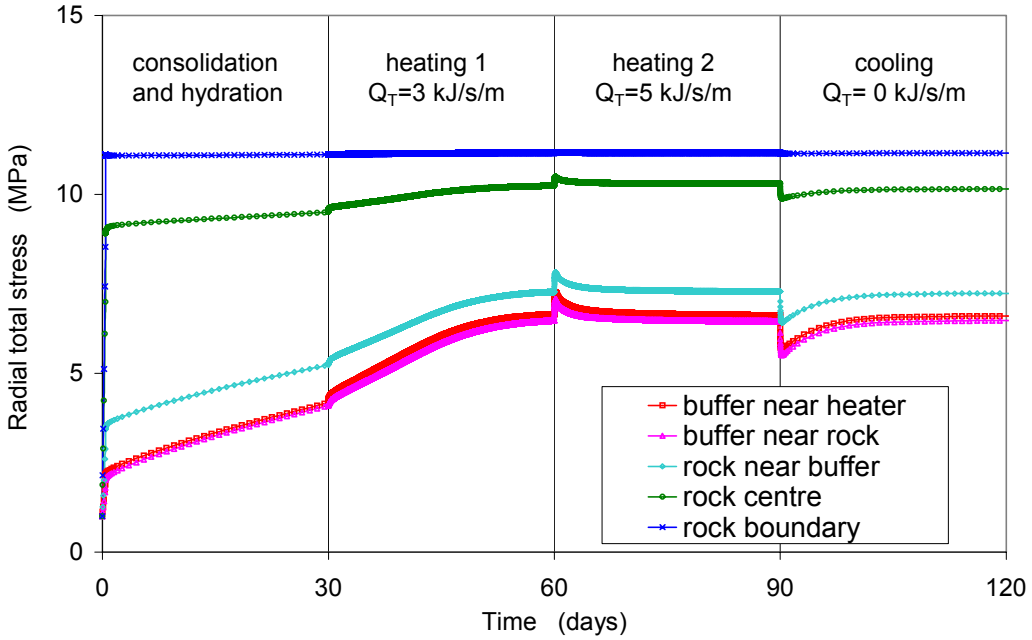

Figure 4.44 Evolution of total radial stress at selected points

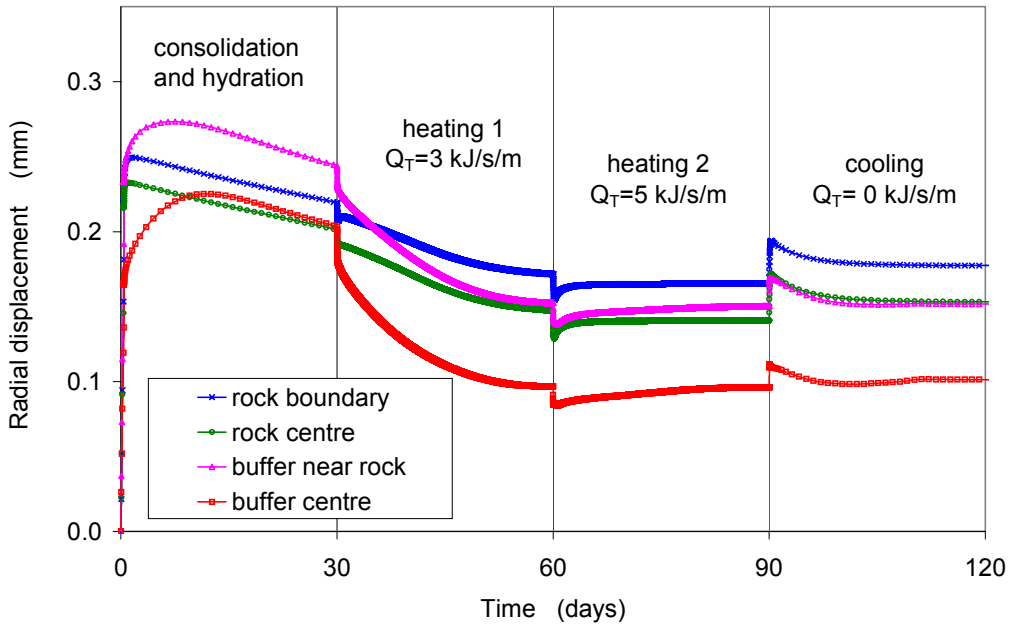

Figure 4.45 Evolution of radial displacement of selected points

Conclusions

The scoping calculations suggest that complex coupled thermal-hydro-mechanical processes will develop in the rock-buffer-system during the test:

- Both rock and buffer behave elastically under the applied confining stress of up to 11 MPa;
- Hydration of the buffer is mainly controlled by suction;
- During the hydration, swelling pressure builds up in the bentonite buffer, which controls the mechanical behaviour of the rock-buffer-system;
- Sudden compaction, heating and cooling produce significant peak water and gas pressures;
- Thermally-induced gas pressure near the heater is higher than the water pressure, but lower than the total stress;
- Sudden heating and cooling generate significant transient changes of the hydro-mechanical behaviour of the rock-buffer-system, however, the thermal effects on the long-term behaviour seem to be insignificant;
- Significant hydro-mechanical interactions between rock and buffer will take place during the experiment.

4.5 Calculations of Perturbations induced by Drift Excavation and Ventilation *in situ*

Due to excavation and ventilation, the hydro-mechanical state of the rock mass around drifts is usually altered. The perturbations in the Opalinus clay were studied by coupled HM modelling of drift excavation and ventilation. The prevailing *in situ* conditions at the Mont Terri URL were taken into account.

Conditions

A 2D plane strain model in a plane normal to the axis of a drift was adopted by a simplified geometry (Figure 4.46). The modelling region extends by 50 m x 50 m. Homogeneous and isotropic properties of the Opalinus clay were assumed.

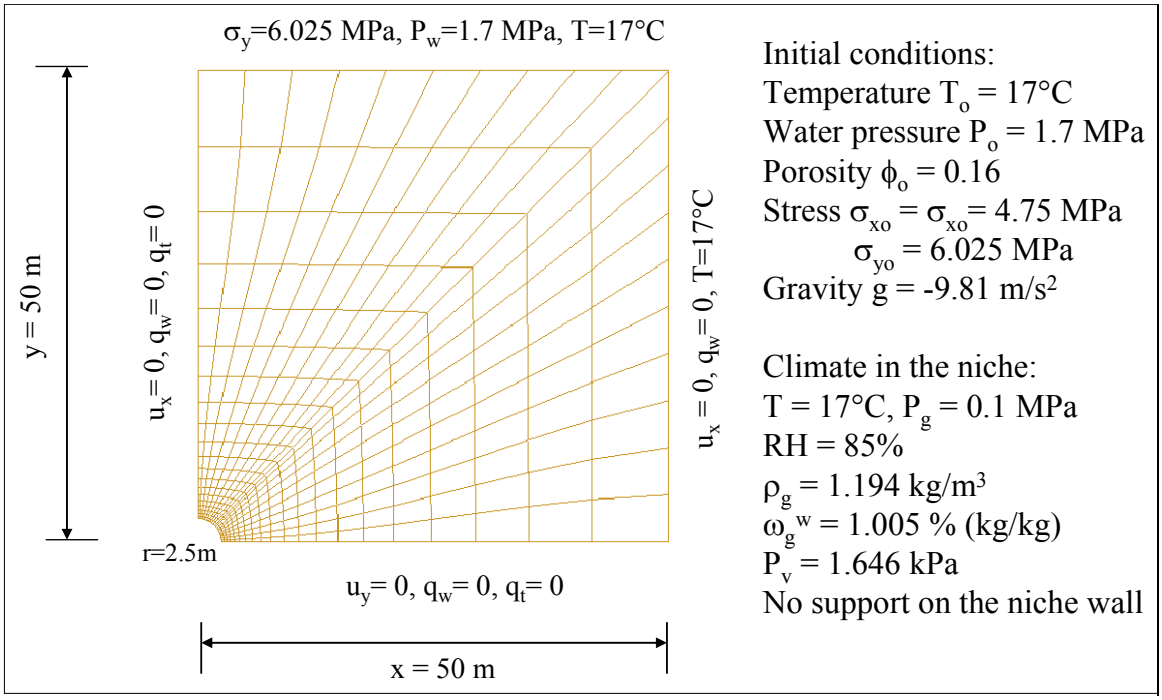

Figure 4.46 Model geometry, discretization, initial and boundary conditions of the rock mass surrounding a drift

Boundary and initial conditions for the modelling are defined in Figure 4.46. The initial temperature in the rock and in the drift is 17 °C for the initial state. A linear increase of the vertical stress with the depth is assumed, but the horizontal stresses are constant with a value of 4.75 MPa. A vertical stress of 6.025 MPa applied on the top boundary and the effect of the gravity result in an initial vertical stress equal to 7.25 MPa at the mean level of the drift (y = 0). A hydrostatic distribution of pore water pressure in the rock is assumed for the initial state. A water pressure of 1.7 MPa supplied to the top boundary results in an increase to 2.2 MPa at the mean level of the drift. Flow of water through the other boundaries is not allowed. The drift excavation is modelled in one step, without support on the drift wall. After that, the drift is ventilated by flowing air with a relative humidity of 85 % on the wall for 6 years. The turbulence coefficient of 10^{-4} m/s is employed for the wall surface. Concerning the problem to be solved, coupled THM calculations were performed. Diffusive vapour flow through the rock mass is taken into account, but no air flow.

Results

Mechanical aspect

After the drift excavation, the stresses concentrate in a zone near the wall. The distributions of total stress along the x - and y - axis are shown in Figure 4.47. At the wall side, the tangential stress reaches about 15 MPa, whereas the tangential stress at the roof reaches about 10 MPa. The variations of the stress state with time are not significant. The final distributions of the horizontal and vertical stresses 6 years after excavation are illustrated in Figure 4.48. The stress state in the far-field about 10 m from the wall remains stable.

Sudden excavation causes sudden convergence of the drift. The radial displacement of the wall reaches 5.5 mm, while the roof drops down by 7.5 mm, as shown in Figure 4.49. The deformations of the far-field steadily increase with time. However, the convergence near the wall ceased in months due to the increase of the stiffness induced by drying. The distribution of the displacements 6 years after the excavation are illustrated in Figure 4.50.

It is interesting to examine the damaged zone surrounding the niche by comparing the stress states in some areas to the yield locus. Figure 4.51 illustrates the results of the examination for the x- and y- axis. The stresses in the near-field within a radius of about 1.3 m attain the yield limit. That means, this zone is damaged, or in other word an EDZ may evolve.

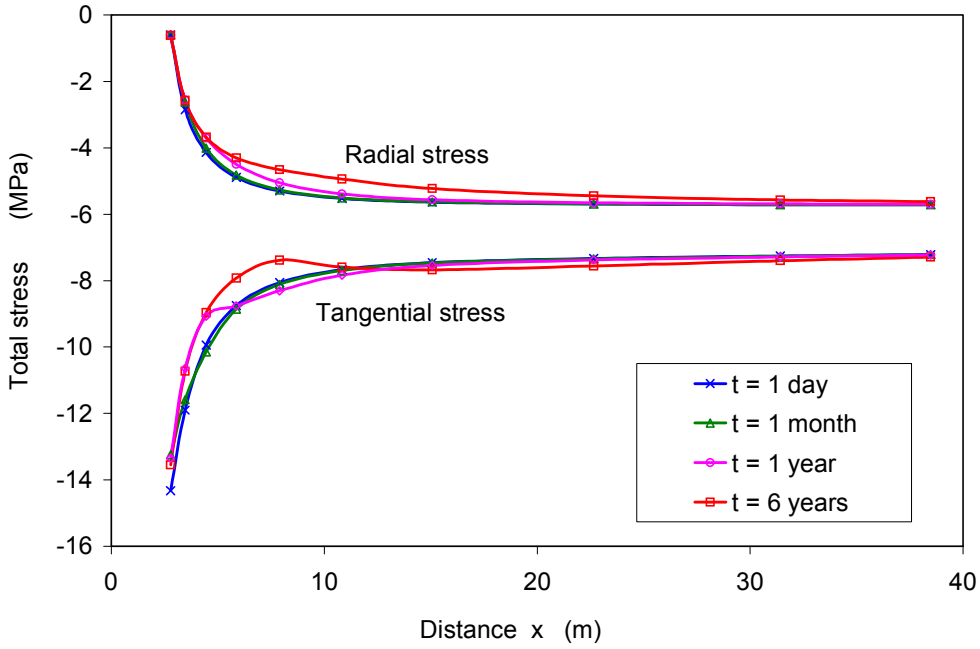

a: stresses along the x - axis

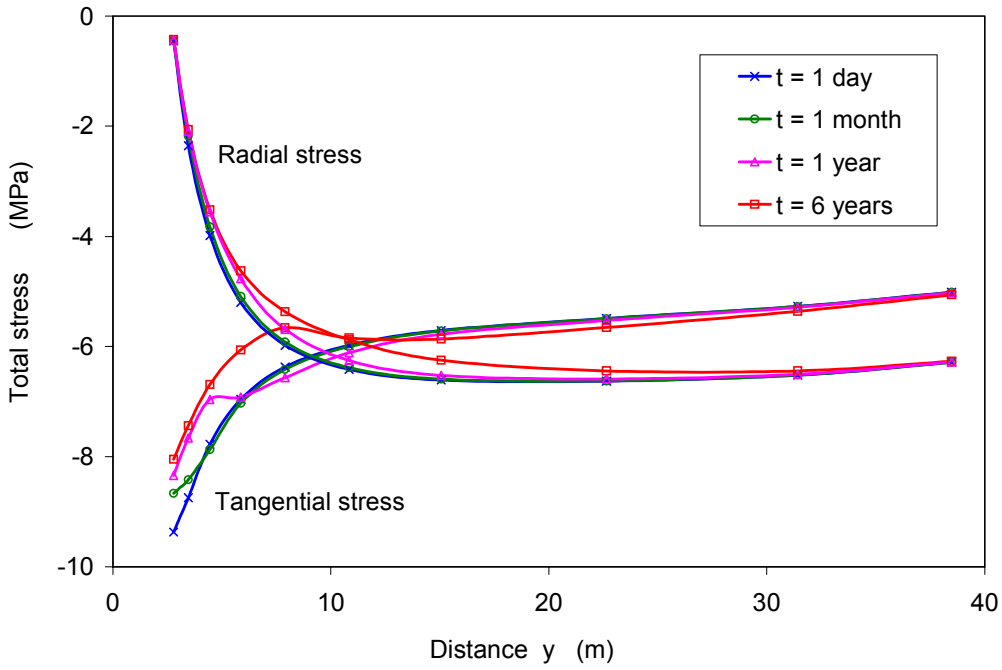

b: stresses along the y - axis

Figure 4.47 Evolution of total stresses along x- and y- axis

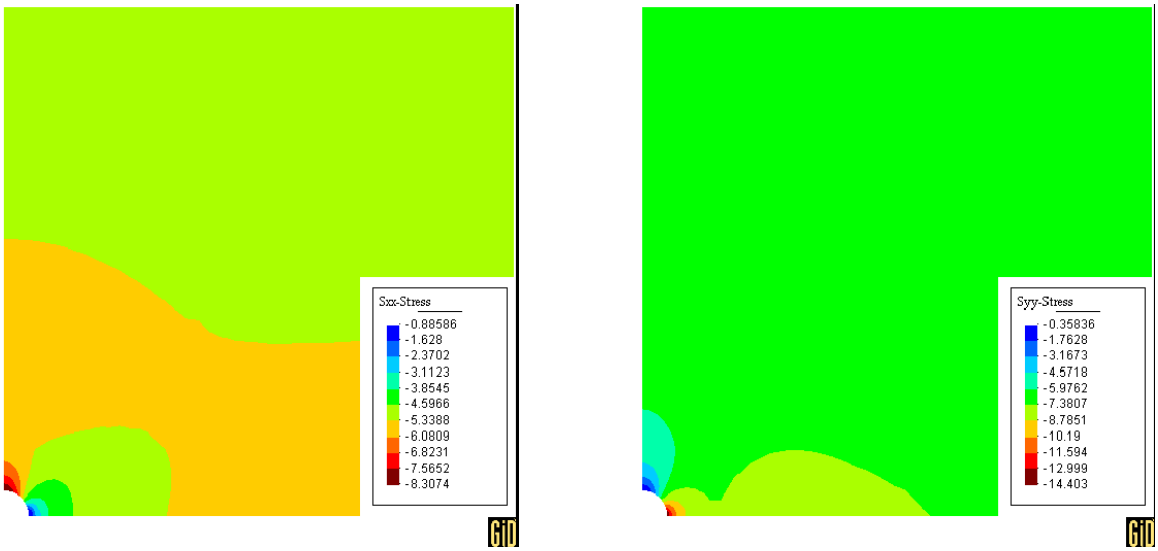

a: horizontal stress b: vertical stress

Figure 4.48 Distributions of total stresses 6 years after excavation

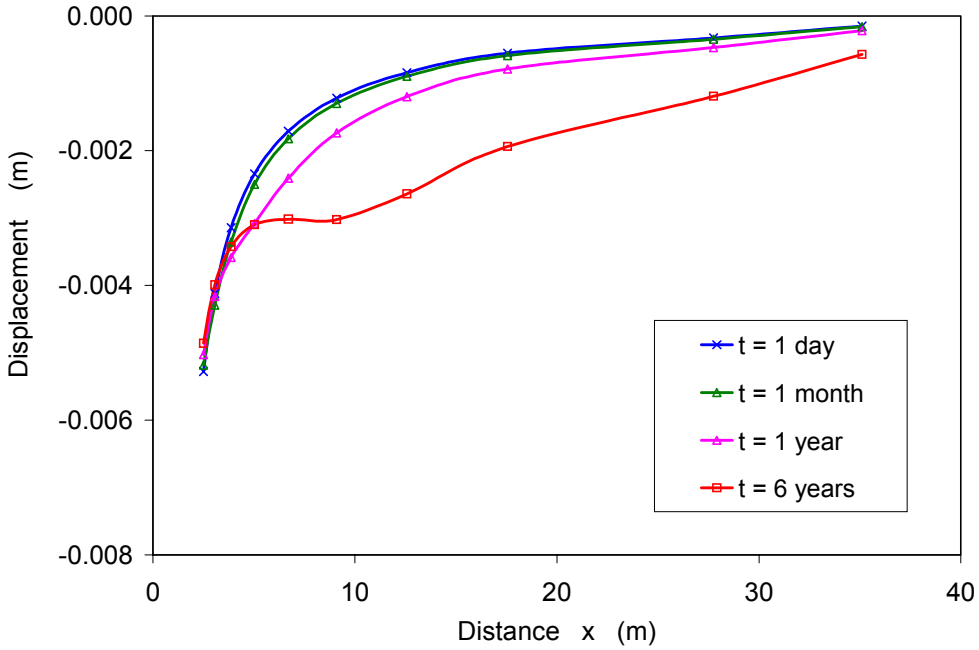

a: displacement along the x - axis

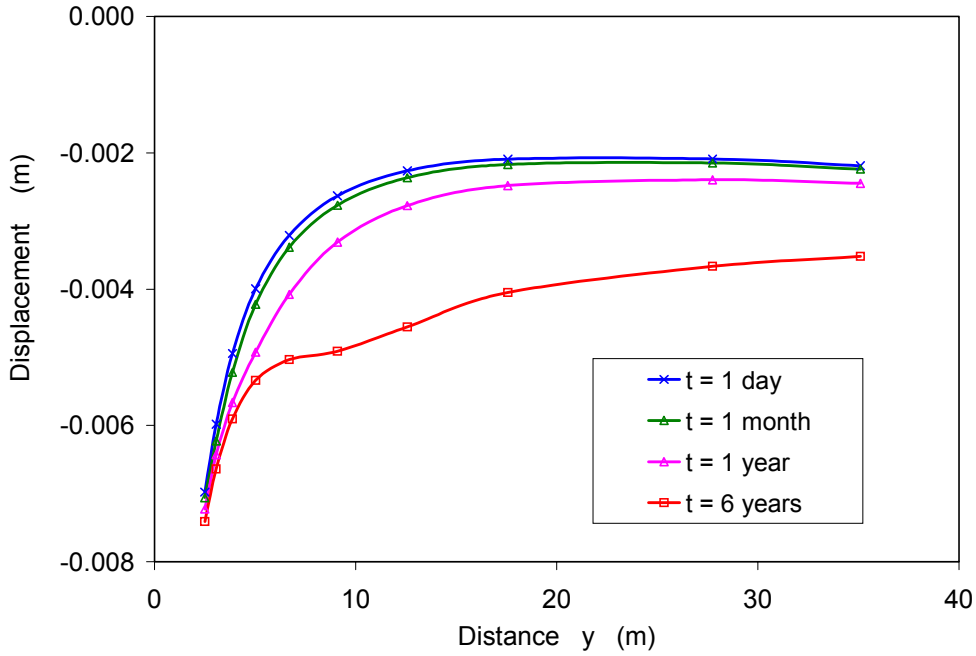

b: displacement along the y - axis

Figure 4.49 Evolution of displacements along x- and y- axis

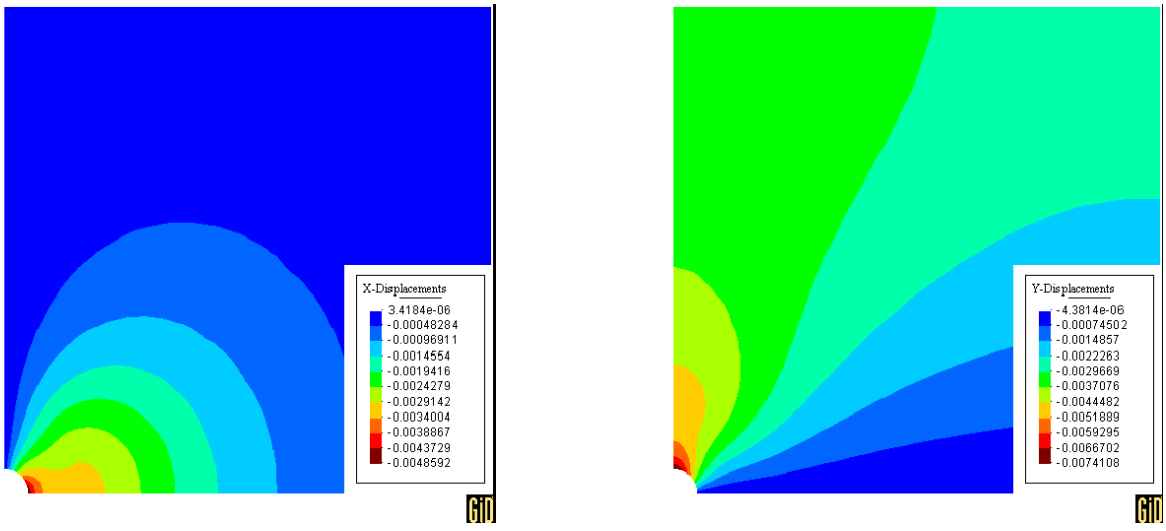

a: horizontal displacement b: vertical displacement

Figure 4.50 Distributions of displacements 6 years after excavation

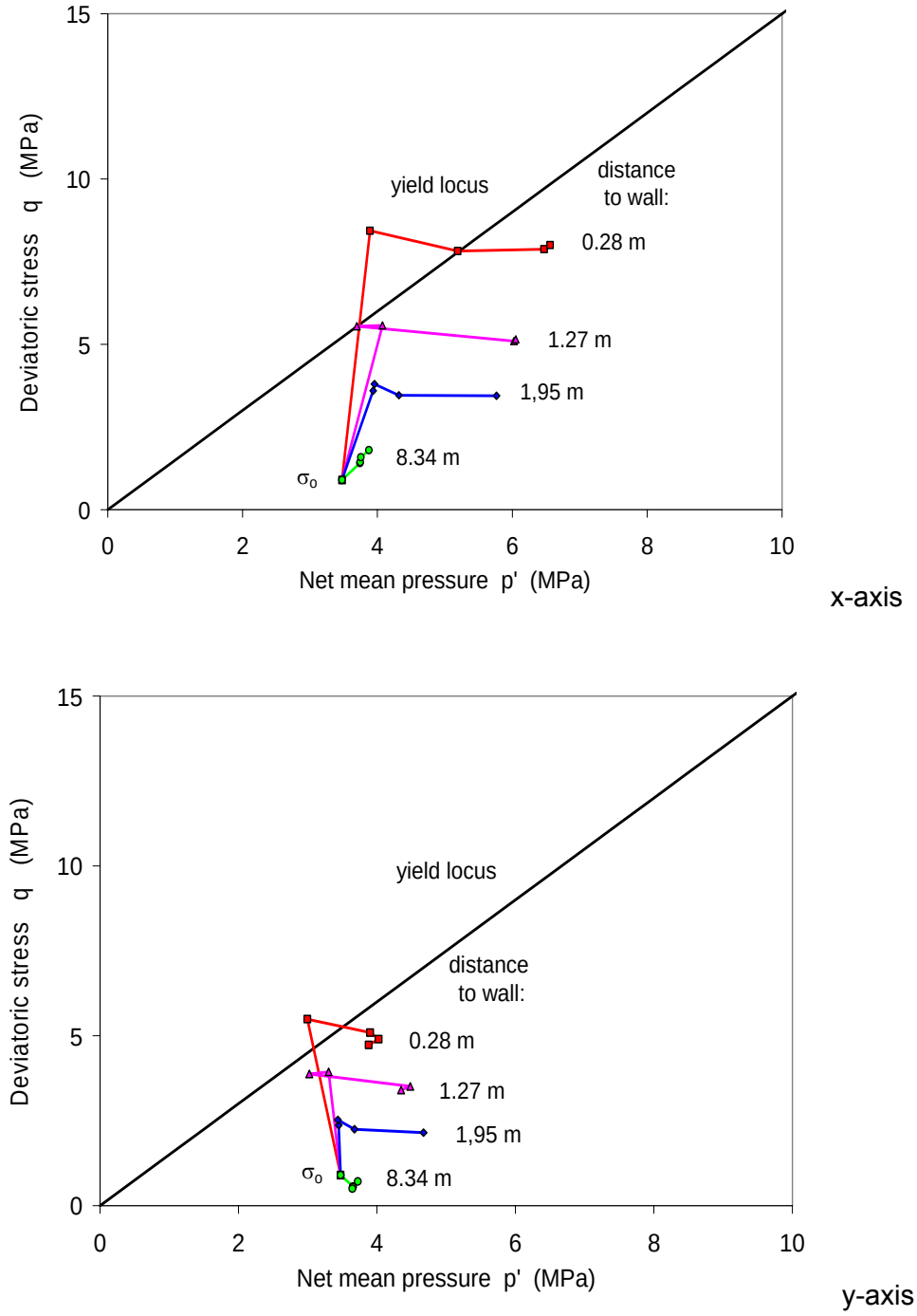

Figure 4.51 Examination of the damaged zone surrounding the niche

For the evaluation of the modelling results, earlier *in situ* observations at the Mont Terri URL /KON 02/ are considered:

- an all over convergence in the order of app. 10 mm (wall displacement in the order of app. 5 mm) was observed in the tunnel immediately after/during creation of the tunnel;

- the extension of the EDZ reaches app. 1 m into the rock;
- the fracture pattern shows dominant tensile cracks.

The calculated displacements of 5.5 to 7.5 mm for the drift wall and the extension of the damage zone within 1.3 m are in a reasonable agreement with these *in situ* observations. However, the development of the EDZ with the evolution of fracturing in the material could not be represented by the BBM elasto-plastic model.

Hydraulic aspect

The hydraulic response of the rock mass to excavation and ventilation of the drift is shown in Figure 4.52. At the drift wall, a sudden increase in pore water pressure up to 3.5 MPa occurs due to the mechanical compression, whereas the reaction of the pore water pressure at the roof is not significant. The initial pore water pressure of about 2.2 MPa in the far-field more than 18 m from the wall remains unchanged. It is very interesting to see that the pore water pressures calculated for 6 years after the excavation agree well with the *in situ* measurements made by Volckaert and Bossart /THU 99/.

During the ventilation with an air relative humidity of 85 %, desaturation takes place from the wall into the rock mass. The near-field within a radius of 5 to 6 m is desaturated (Figure 4.53).

Generally, the calculated results of hydro-mechanical perturbations induced by drift excavation and ventilation agree with the *in situ* observations. However, the used version of CODE-BRIGHT did not include adequate constitutive equations for the description of damage or EDZ evolution in indurated clays. Within the MODEX-REP project, various constitutive models have been developed for the description of the hydro-mechanical behaviour of indurated clays, one of which was proposed by Vaunat et al. /MOD 03/. This model is able to describe the damage evolution in clay rock. It has been implemented in the new version of CODE-BRIGHT and has been used to model the coupled THM processes in the Opalinus clay in the HE-D project /WIL 03/.

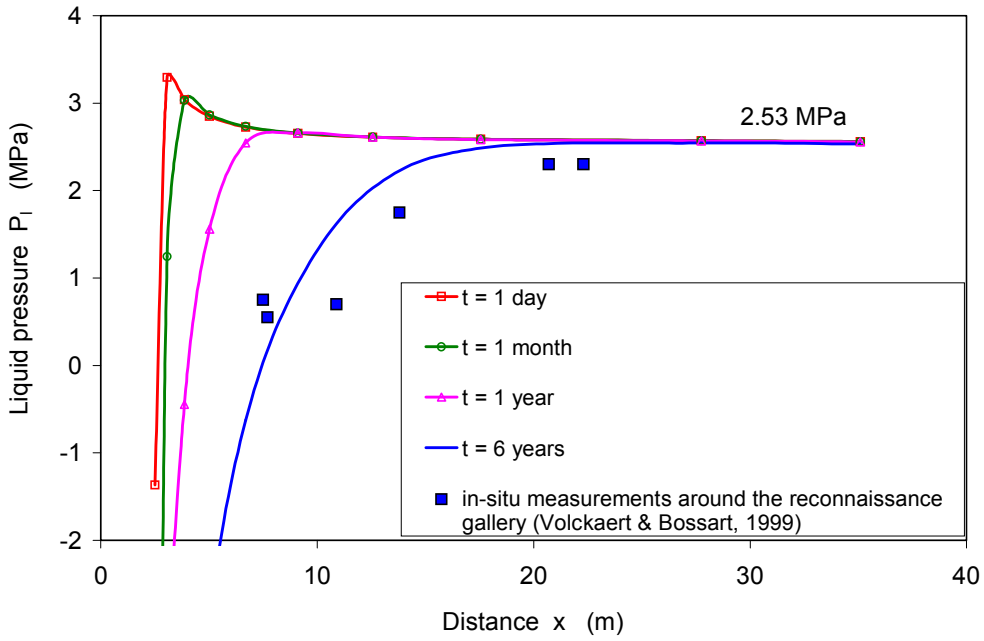

a: pore water pressure along the x - axis

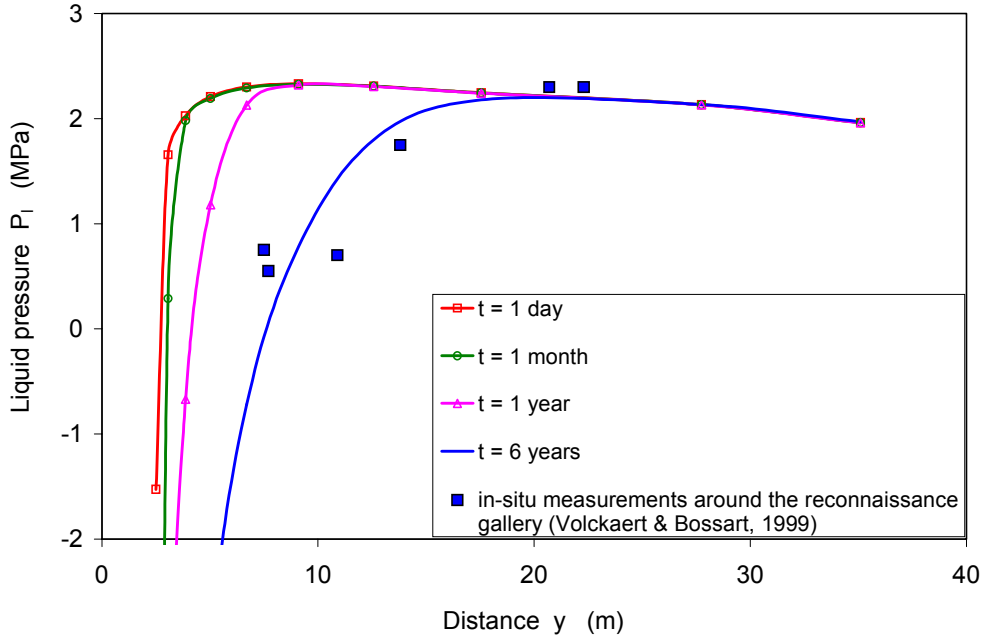

b: pore water pressure along the y - axis

Figure 4.52 Distribution of pore water pressure

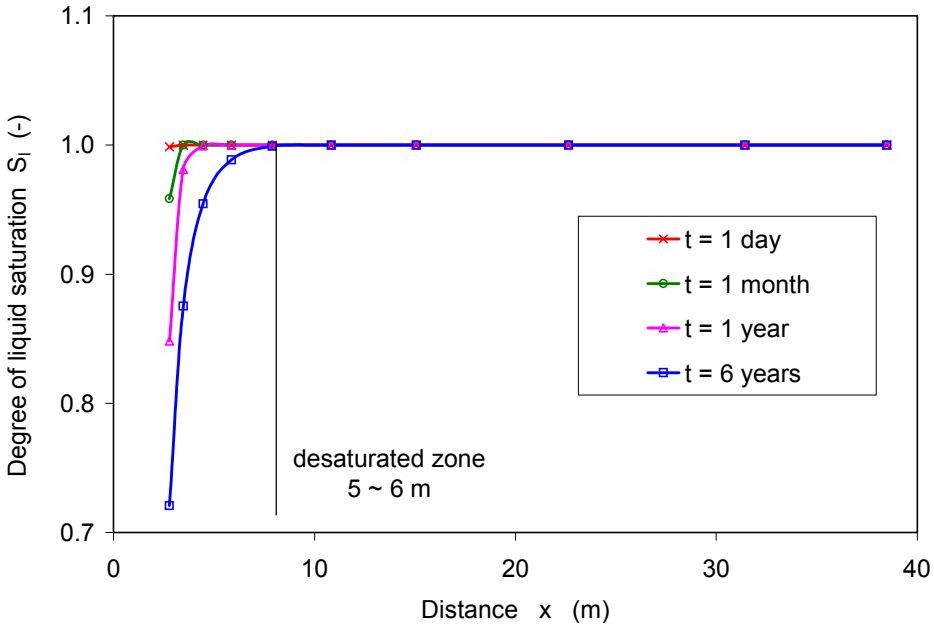

a: water saturation along the x - axis

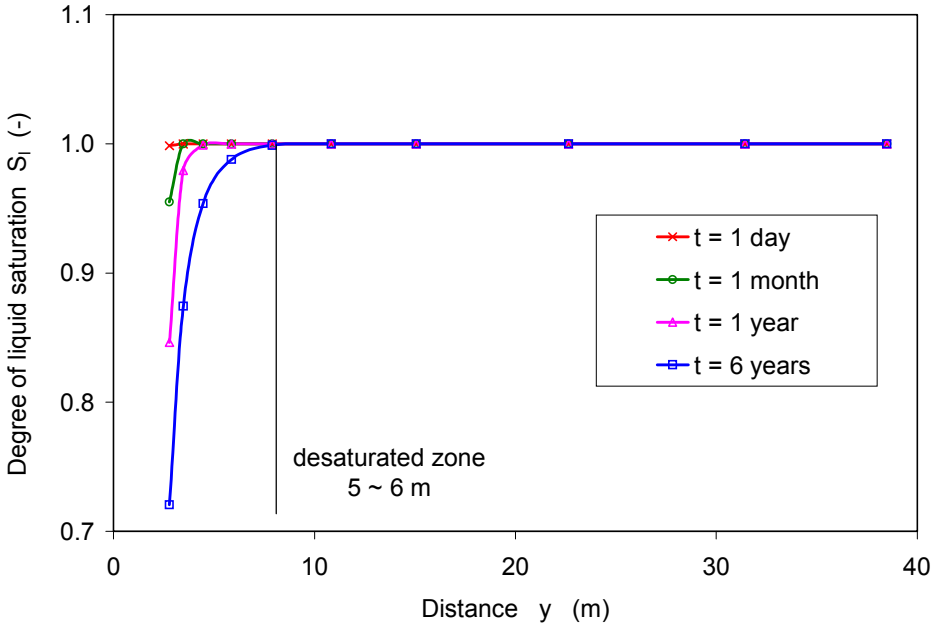

b: water saturation along the y - axis

Figure 4.53 Evolution of water saturation along x- and y- axis

5 Summary

In recent years, research on clay formations to host a repository for radioactive waste has been initiated in Germany. Participation in the Mont Terri projects in Switzerland has been started and participation in the Bure research programme is envisaged on basis of a ANDRA/GRS – cooperation agreement. As a first step, a pre-project was started by GRS in July 2001, under contract number 02 E 9541 with BMWA. In the pre-project, laboratory and modelling programmes were conducted to develop testing methods for investigation of the THMC behaviour of clays and to gain experiences with numerical modelling of coupled THM processes in clays.

5.1 Laboratory Experiments

Geotechnical and geochemical experiments were performed on core samples of the Callovo-Oxfordian argillite and the Opalinus clay to investigate the long-term creep, swelling and shrinkage, coupled hydro-mechanical behaviour and thermal effects. In addition, the diffusion of radionuclides and the extraction of pore water were examined.

Long-term creep

Uniaxial creep tests were conducted under different constant loads of 0.6 to 18 MPa at ambient temperature. Most of the tests lasted over an exceptionally long period of time more than 2.5 years with each step phase lasting between 1 and 18 months. The main results are:

- Even under very low loads of 0.6 to 1.0 MPa, the Callovo-Oxfordian argillite and the Opalinus clay exhibit significant creep strains confirming that there exists no stress threshold for the onset of creep in the indurated clays;
- No cease of creep was observed even over more than 18 months under different load levels;
- High carbonate content and low water content slow down the creep;
- Steady state creep seems to be reached after a transient creep phase over weeks to months at low stresses of up to 5 MPa and over months to years at higher stresses;

- Pure creep strain and creep rate parallel and perpendicular to the bedding are almost the same suggesting that an anisotropy effect may be negligible on the long-term mechanical behaviour.

Swelling and shrinkage

Horseman et al. /HOR 96/ suggested that the conventional isotropic effective stress in saturated plastic and indurated clays is equal to the average disjoining pressure of interpaticle water-films or equal to the swelling pressure. This implies that the water-films are stress-supporting and carry the lithostatic stress. This stress concept was examined by means of specially developed testing methods of uniaxial swelling pressure and strain tests.

On a Callovo-Oxfordian specimen under axially-fixed and laterally-unconstraint conditions, the uniaxial swelling pressure was measured during re- and desaturation by introducing water vapour or dry air into the specimen. The swelling pressure increases with increasing water saturation. At nearly and fully saturated conditions, high swelling pressures of 10 to 12 MPa were observed, which are practically equal to the lithostatic stress at the sampling depth of 455 m (~ 11 MPa). When the degree of water saturation is lower than a threshold value, the swelling pressure disappears.

In the uniaxial swelling strain tests on Callovo-Oxfordian specimens under constant axial load and laterally-unconstraint conditions, the argillite exhibits also significant swelling strains during resaturation even under high axial loads of 15 to 18 MPa. Desaturation results in shrinkage due to the release of the interparticle water-films.

However, a traditional swelling test on a Callovo-Oxfordian specimen immersed in clay water over about 500 days shows a swelling pressure of 1.6 MPa, much lower than that measured in the uniaxial swelling pressure test. The reasons for the difference are not very clear.

Coupled thermo-hydro-mechanical behaviour

Preliminary THM experiments were conducted on three samples of the Callovo-Oxfordian argillite and Opalinus clay in a triaxial apparatus. A general testing procedure was followed by *saturation* under isotropic stress of 5 MPa and water injection pressures of 3 - 4 MPa, by *consolidation* under 12 to 19 MPa isotropic stresses, by

heating up to 150 °C and by *cooling* down to ambient temperature. Very complex coupled thermo-hydro-mechanical phenomena were observed:

- Effects of external stress on the hydraulic behaviour: Under undrained conditions, application of an external stress to the clays results in an increase in pore water pressure. Skempton's coefficient B = 84 % to 97 % were determined, indicating unsaturation of the specimens. Different pressure responses of both separated water reservoirs at the bottom and top of the specimens were observed during the consolidation. This may imply that there are practically no hydraulic pathways through the intact clays for advective water flow. Adsorbed water-films in the clays may act as barriers against advective water flow.

- Effects of external water pressure on the mechanical behaviour: Application of an external water pressure to the clays increases the pore water pressure and hence reduces the effective stress under a constant total stress. This causes a volumetric expansion of the material. In contrast, reduction in pore water pressure results in compaction under drained conditions.

- Thermal effects on the hydro-mechanical behaviour: Because the very low hydraulic conductivity of the clays does not allow the pore water so fast to disperse, heating results in an increase in pore water pressure, which reaches the maximum under fully-saturated and undrained conditions. Under isotropic stresses of 15 to 19 MPa and undrained as well as partly-drained conditions, increasing temperature from 32 to 91 °C and 25 to 120 °C results in an increase of the pore water pressure up to 10 to 12.5 MPa. Thermal expansion was observed during the heating phases from 25 to 60, 90, 120 and 150 °C even under high stresses up to 15 MPa. Under drained conditions, consolidation of the indurated clays occurred during the heating phases due to the release of the thermally-desorbed pore water. In contrast to heating, cooling causes contraction of pore water and reduces the pore water pressure. Correspondingly, the effective stress under a constant external stress is increased, causing consolidation under drained conditions.

Diffusion

A cheap and simple cell was constructed for the investigation of nuclide-diffusion in the Callovo-Oxfordian argillite. The cell as well as findings in the first experiment need to be supplemented by more experiments with a greater variety of samples.

Extraction of pore water

An established method, originally been invented for the leaching of toxic chemical waste has been employed for the leaching of clay. Clearly, an equilibrium between solution and unaltered clay has not been created during the experiments. A much higher number of leaching steps would be necessary. Further problems relating to the analysis of Si and Al were identified. With these problems overcome and cation exchange accounted for it is still believed that geochemical modelling could extend the experimental range of solid/solution ratios in leaching experiments such that real pore water composition could be calculated.

5.2 Numerical Modelling

A large number of THM modelling exercises were performed by use of the THM code CODE-BRIGHT. From literature, available constitutive parameters for different clays such as Serrata bentonite, FoCa bentonite, Boom clay, Opalinus clay and Callovo-Oxfordian argillite were collected.

The modelling exercises performed include scoping calculations of the coupled THM phenomena observed in clays under laboratory conditions, such as swelling pressure and strain, consolidation and collapse, resaturation and desaturation, moisture and air transport in clays by heating and cooling. The modelling results are comparable with the laboratory observations. To support some *in situ* experiments in the Mont Terri URL, GRS has proposed laboratory simulation experiments on large samples of 700 mm length and 270 mm diameter. Tests envisaged to be performed in the laboratory are a ventilation test /VE 02/ and a heating test /HEB 02/. The large-scale simulation tests were predicted by THM modelling. Finally, hydro-mechanical perturbations in the Opalinus clay due to drift excavation and ventilation were calculated. The modelling results are in a good agreement with the *in situ* observations in the Mont Terri URL. Generally, the suitability of the CODE-BRIGHT was validated by the modelling exercises. However, the capability of the code for modelling some „abnormal" phenomena observed on the indurated clays, for instance the stress-supporting capability of interparticle water-films, has not been examined.

5.3 Future Investigations

Data as well as knowledge about the coupled THM behaviour of indurated clays are still limited, especially with regard to the governing mechanisms. The preliminary experimental results reported here are more qualitative. Some conclusions drawn from the tests are to be verified. Some explanations of the observed „abnormal" phenomena are preliminary. Therefore, combined theoretical and laboratory investigations on the coupled THM behaviour of indurated clays are to be continued in the future. For prediction of long-term performance of clays to host high-level and long-lived radioactive wastes more physically-based constitutive models are to be developed.

6 Acknowledgements

The described work was funded by the German Federal Ministry of Economics and Labour (BMWA) under contract No. 02 E 9541. The authors would like to thank for this support. The support from the French Agence Nationale Pour la Gestion de Déchets Radioactifs (ANDRA) for providing the testing material and intensive discussion of the GRS work programme as well as the support from the Geotechnical Engineering Department of the Technical University of Catalonia in Barcelona (UPC) with regard to implementation of the code CODE-BRIGHT are also gratefully acknowledged.

7 References

/ALO 98/ Alonso, E.E.; Lloret, A.; Delahaye, C.H.; Vaunat, J.; Gens, A.; Volckaert, G. (2000): Coupled analysis of a Backfill Hydration Test. International Journal for numerical and analytical methods in geomechanics,Vol.22 (1998),22-27.

/ALO 00/ Alonso, E.E. and Alcoverro, J. (2000): Calculation and testing of the behaviour of unsaturated clay as a barrier in radioactive waste repositories ('Catsius clay' project). Final report, EUR 19141 EN.

/ALO 02/ Alonso, E.E.; Olivella, S.; Delahaye, C.(2002): Gas Migration in Clays. Environmental Geomechanics – Monte Verita 2002, 83-94.

/AND 00/ ANDRA (2000): Experimental programme at the Meuse/Haute-Marne Underground Research Laboratory.- A short view. June 2000, C RP ASRP 2000 – 2006.

/AND 03a/ ANDRA: HLW CLAY REPOSITORY PROJECT – SCIENTIFIC PROGRAMME 2002 – 2005.

/AND 03b/ ANDRA: COMPTE RENDU DES REVUES ET REUNIONS TECHNIQUES EXPERIMENTATIONS SUG, GIS ET REP. Seminaire Geomecanique, April 17-18, 2003.

/BOC 01/ Bock, H. (2001): RA Experiment - Rock mechanics analyses and synthesis: Data Report on Rock Mechanics. Technical Report 2000-02.

/BOC 02/ Bock, H. (2002): RA Experiment - Rock mechanics analyses and synthesis: Data Report on Rock Mechanics. Technical Report 2001-03.

/FLO 02/ Floria, E.; Sanz, F.J.; Garcia-Sineriz, J.L. (2002): Drying test: evaporation rate from core specimens of „Opalinus clay" under controlled environmental conditions, VE-Deliverable 6.

/GAS 00/ Gasc-Barbier, M; Cosenza,P.; Ghoreychi, M.; Chanchole, S.: Laboratory Experiments on Swelling-Shrinkage of Deep Clays under Triaxial Stress. EUROCK 2000 symposium, Aachen 27.-31. March 2000, pp. 705-710.

/GAS 02/ Gasc-Barbier, M; Chanchole, S.; Lecampion, B.; Bérest, P.; Hoteit, N.: Study of the Creep Behaviour of Bure Clayey Rock. In the International Meeting of Clays in Natural and Engineered Barriers for Radioactive Waste Confinement, December 9-12, 2002, Reims, France.

/GEN 95/ Gens, A. (1995): Constitutive laws. In : Gens, A., Jouanna, P., Schrefler, B.A. (Eds.), Modern Issues in Non-Saturated Soils, Springer Verlag, Wien, 129-158.

/GEN 98/ Gens, A.; Garcia-Molina, A.J.; Olivella, S.; Alonso, E.E.; Huertas, F. (1998): Analysis of a Full Scale in situ Test Simulating Repository Conditions. Int. J. Numer. Anal. Meth. Geomech., 22, 515-548 (1998).

/GRS 01/ GRS Proposal on Co-Operation in the Bure Research Programme. ANDRA/GRS meeting on 24 Sept. 2001, Braunschweig.

/HEB 02/ HE Experiment – Rock and bentonite thermo-hydro-mechanical processes in the near field, Test Plan (D1), FIKW-CT-2001-00132.

/HER 02/ Herbert, H.-J.; Moog, H.-C.: Untersuchungen zur Quellung von Bentoniten in hochsalinaren Lösungen. Mai 2002, GRS-179, ISBN3-931995-47-X.

/HOR 96/ Horseman, S.T.; Higgo, J.J.W.; Alexander, J.; Harrington, J.F.: Water, Gas and Solute Movement Through Argillaceous Media. Report CC-96/1, 1996.

/HUE 00/ Huertas, F.; Fuentes-Cantillana, J.L.; Fullien, F.; Rivas, P.; Linares, J.; Farina, P.; Ghoreychi, M.; Jockwer, N.; Kickmaier, W.; Martinez, M.A.; Samper, J.; Alonso, E.; Elorza, F.J. (2000): Full-scale engineered barriers experiment for a deep geological repository for high-level radioactive waste in crystalline host rock (FEBEX project). Final report, EUR 19147 EN.

/ISR 81/ ISRM: Rock Characterization Testing & Monitoring – ISRM Suggested Methods, 1981.

/KAN 99/ Kanno, T.; Fujita, T.; Takeuchi, S.; Ishikawa, H.; Hara, K.; Nakano, M. (1999): Coupled Thermo-Hydro-Mechanical Modelling of Bentonite Buffer Material. Int. J. Numer. Anal. Meth. Geomech., 23, 1999, 1281-1307.

/KON 02/ Konietzky, H. (2002): RA (Rock mechanics analyses and synthesis) Experiment: Modelling of HM coupled behaviour of the EDZ. Technical Note 2001-19.

/KRÖ 03/ Kröhn, K.-P. (2003): Results and interpretation of bentonite resaturation experiments with liquid water and water vapour. ISSMGE International Conference from Experimental Evidence towards Numerical Modelling of Unsaturated Soils, September 18-19, 2003, Bauhaus-Universität Weimar.

/LEB 00/ Lebon, P.; Ghoreychi, M.: French Underground Research Laboratory of Meuse/Haute-Marne: THM Aspects of Argillite Formation. EUROCK2000, Aachen, 27.-31. March 2000.

/LI 98/ Li, X.L.; Collin, F.; Radu, J.P.; Charlier, R. (1998): Thermo-hydro-mechanical coupling in clay barriers. The Geotechnics of Hard Soils – Soft Rocks, Evangelista & Picarelli (eds), 1998 Balkema, Rotterdam, 647-658.

/MOD 03/ MODEX-REP: Constitutive Models of the Meuse/Haute-Marne Argillites. Editors: Modex-Rep project research teams, compiled by Kun Su. MODEX-REP – FIKW-CT2000-00029. Deliverable 2 & 3, February 2003.

/MOH 96/ Mohamed, A.M.O.; Yong, R.N.; Onofrei, C.L.; Kjartanson, B.H. (1996): Coupled Heat and Moisture Flow in Unsaturated Swelling Clay Barriers. Geotechnical Testing Journal, GTJODJ, Vol. 19, No.2, 1996, 155-163.

/OLI 94/ Olivella, S.; Carrera, J.; Gens, A.; Alonso, E.E. (1994): Nonisothermal Multiphase Flow of Brine and Gas Through Saline Media. Transport in Porous Media, 15, 271-293 (1994).

/PEA 99/ Pearson, F. J. (1999): Mont Terri Project, Technical Note 99-31, January 1999, WS-A experiment: artificial waters for use in laboratory and field experiments with Opalinus clay. Status June 1998.

/PEL 99/ Pellegrini, R.; Horseman, S.; Kemp, S.; Rochelle, C.; Boisson, J.-Y.; Lombardi, S.; Bouchet, A.; Parneix, J.-C. (1999): Natural analogues of the thermo-hydro-chemical and thermo-hydro-mechanical response. Final report, EUR 19114 EN.

/RA 01/ RA Experiment – Rock analyses and synthesis: Data report and rock mechanics. TR2000-02, H.Bock – Q+S Consult, May 2001.

/ROD 99/ Rodwell, W.R.; Harris, A.W.; Horseman, S.T.; Lalieux, P.; Müller, W.; Ortiz amaya, L.; Pruess, K.: Gas Migration and Two-Phase Flow through Engineered and Geological Barriers for a Deep Repository for Radioactive Waste. A Joint EC/NEA Status Report, European Commission, 1999, EUR 19122 EN

/SU 99/ Su, K.; Ozanam, O.: Rheological model for the Eastern argillites – Summary of status for the rheological studies (Meuse/Haute-Marne site). C RP AGEM 99-061, 1999.

/SU 03/ Su, K.: Geomechanical Investigation of the Callovo-Oxfordian Argillaceous Formation at the Meuse/Haute-Marne Site of France. Presentation in Clausthal Kolloquium zur Endlagerung 2003.

/THO 98/ Thomas, H.R.; He, Y.; Onofrei, C. (1998): An Examination of the Validation of a Model of the Hydro/Thermo/Mechanical Behaviour of Engineered Clay barriers. Int. J. Numer. Anal. Meth. Geomech., 22, 1998, 49-71.

/THU 99/ Thury, M.; Bossart, P.: Mont Terri Rock Laboratory, Results of the Hydrogeological, Geochemical and Geotechnical experiments Performed in 1996 and 1997. Geologische Berichte Nr. 23, 1999, Bern.

/UPC 02/ CODE-BRIGHT, A 3-D program for thermo-hydro-mechanical analysis in geological media, USER'S GUIDE. 2002.

/VAL 02/ Valés, F.; Bérest, P.; Gharbi, H.: Interaction between creep, Swelling and Pressure-Solution during Indentation Tests. In the International Meeting of Clays in Natural and Engineered Barriers for Radioactive Waste Confinement, December 9-12, 2002, Reims, France.

/VE 02/ VE Experiment - Ventilation Experiment in Opalinus clay, Test Plan, Deliverable 3&6, FIKW-CT2001-00126.

/VOL 96/ Volckaert,G.; Bernier,F.; Alonso,E.; Gens,A.; Samper,J.; Villar,M.; Martin-Martin,P.L.; Cuevas,J.; Campos,R.; Thomas,H.; Imbert,C.; Zingarelli,V. (1996): Thermo-hydraulic-mechanical and geochemical behaviour of the clay barrier in radioactive waste repositories (model development and validation). Final report, EUR 16744 EN.

/VOL 00/ Volckaert,G.; Dereeper,B.; Put,M.; Ortiz,L.; Gens,A.; Vaunat,J.; Villar,M.; Martin,P.L.; Imbert,C.; Lassabatere,T.; Mouche,E.; Cany,F. (2000): A large-scale in situ demonstration test for repository sealing in an argillaceous host rock, Reseal project – Phase I. Final report, EUR 19612 EN.

/WIL 03/ Wileveau, Y.; Rothfuchs, T.: HE-D Experiment: Test Plan. Mont Terri Project, Technical Note 2004-20, September 2003.

/ZHA 02a/ Zhang, C.L., Dittrich, J., Müller, J., Rothfuchs, T.: Experimental Study of the Hydromechanical Behaviour of the Callovo-Oxfordian Argillites – Part of the MODEX-REP Project. December 2002, GRS-187, ISBN3-931995-55-0.

/ZHA 02b/ Zhang, C.L., Rothfuchs, T.: Experimental Study of the Hydro-Mechanical Behaviour of the Callovo-Oxfordian Argillite. In the International Meeting of Clays in Natural and Engineered Barriers for Radioactive Waste Confinement, December 9-12, 2002, Reims, France.

/ZHA 03/ Zhang, C.-L.; Kröhn, K.-P.; Rothfuchs, T. (2003): Applications of CODE-BRIGHT to Thermal-Hydro-Mechanical Experiments on Clays. ISSMGE International Conference from Experimental Evidence towards Numerical Modelling of Unsaturated Soils, September 18-19, 2003, Bauhaus-Universität Weimar.

List of Figures

Figure 1.1 General view of the MHM - Underground Research Laboratory at Bure in France /ANDRA 03/ 1

Figure 2.1 Samples from the Callovo-Oxfordian argillite at the MHM-URL Bure..... 8

Figure 2.2 Samples from the Opalinus clay at the Mont Terri URL 8

Figure 2.3 Uniaxial creep rigs at the GRS geotechnical laboratory 15

Figure 2.4 Creep testing conditions for Callovo-Oxfordian specimens EST05481-01 and EST05671-01 19

Figure 2.5 Creep curves of Callovo-Oxfordian specimens EST05481-01 and EST05671-01 19

Figure 2.6 Creep rates as a function of strain for Callovo-Oxfordian specimens EST05481-01 and EST05671-01 20

Figure 2.7 Testing conditions for Callovo-Oxfordian specimens EST05630-02, EST05582-02/-03 and EST05671-02/-03..... 21

Figure 2.8 Creep curves of Callovo-Oxfordian specimens EST05630-02, EST05582-02/-03 and EST05671-02/-03..... 21

Figure 2.9 Creep rates as a function of strain for Callovo-Oxfordian specimens EST05582-03 and EST05671-02 / -03 22

Figure 2.10 Creep curves of Callovo-Oxfordian specimens EST05684-01 and MSE00837-01..... 23

Figure 2.11 Creep rates as a function of strain for Callovo-Oxfordian specimens EST05684-01 and MSE00837-01 23

Figure 2.12 Creep curves of Opalinus specimens BVE1-01/-02 taken from the VE ventilation test field in the Mont Terri URL..... 25

Figure 2.13 Creep curves of Opalinus specimens HEB26-01/-02 taken from the HEB heating test field in the Mont Terri URL 25

Figure 2.14 Schematic inner structure of a indurated clay 27

Figure 2.15 GRS swelling cell /HER 02/ 30

Figure 2.16 Swelling pressure of Callovo-Oxfordian specimen EST05630-04 measured in GRS swelling cell 31

Figure 2.17 Schematic assembly of uniaxial swelling test 33

Figure 2.18 Measurements of temperature, relative humidity and axial stress during the uniaxial swelling test EST05547-07 34

Figure 2.19 Uniaxial swelling, shrinkage and creep of Callovo-Oxfordian specimens EST05582-02 and EST05630-02 36

Figure 2.20 Schematic setup and photos of GRS oedometer cell 38

Figure 2.21 Schematic and photo of the TDZM triaxial apparatus at the GRS laboratory 40

Figure 2.22 Thermo-hydro-mechanical loading conditions on a clay specimen 41

Figure 2.23 Results of the HM test on Callovo-Oxfordian specimen EST05684-02 43

Figure 2.24 Results of the HM test on Callovo-Oxfordian specimen EST05490-01 46

Figure 2.25 Results of the HM test on Opalinus clay specimen BVE1-03 48

Figure 2.26 Results of the THM test on Callovo-Oxfordian specimen EST05490-01 50

Figure 2.27 Results of the THM test on Opalinus clay specimen BVE1-03 53

Figure 3.1 Diffusion cell 58

Figure 3.2 Diffusion cell disassembled 59

Figure 3.3 Flux of spikers through Bure clay 61

Figure 3.4 Principal sketch of a cascade reaction chamber 63

Figure 3.5 Principal sketch of a cascade leaching experiment 64

Figure 3.6 Evolution of concentrations for Mg, Ca, and SO_4 65

Figure 3.7 Evolution of concentrations for Na during both experiments 66

Figure 3.8 Evolution of concentrations for K during both experiments 67

Figure 3.9 Evolution of pH during both experiments 68

Figure 4.1 Thermal conductivity of clays as a function of liquid saturation 81

Figure 4.2 Retention curves of clays 81

Figure 4.3 Intrinsic permeability of clays as a function of porosity 82

Figure 4.4 Relative permeability of clays as a function of liquid saturation 82

Figure 4.5 Yield surface of the BBM model for unsaturated soils 83

Figure 4.6 Volumetric response of unsaturated soils to wetting and loading 84

Figure 4.7 Comparison of yield curves of different clays 85

Figure 4.8 Consolidation behaviour of clays in saturated conditions 86

Figure 4.9 Swelling deformations of different clays 86

Figure 4.10 Evolution of water saturation during wetting 88

Figure 4.11 Porosity variation during wetting 89

Figure 4.12 Evolution of swelling pressure during wetting 89

Figure 4.13 Swelling deformation during wetting 90

Figure 4.14 Swelling pressures during wetting 91

Figure 4.15 Evolution of stresses during compaction and wetting of bentonite 92

Figure 4.16 Evolution of water saturation during compaction and wetting of bentonite 92

Figure 4.17 Porosity evolution during compaction and wetting of bentonite 93

Figure 4.18 Consolidation behaviour during loading and wetting of bentonite 93

Figure 4.19 Comparison of water saturation measured on MX-80 bentonite and calculated for Serrata bentonite 95

Figure 4.20 Comparison of porosity measured on MX-80 bentonite and calculated for Serrata bentonite 95

Figure 4.21 Comparison of water saturation in Opalinus clay samples observed in a drying test conducted by AITEMIN /VE 02/ and data calculated by GRS 96

Figure 4.22 Thermo-hydraulic cell used in CIEMAT heating tests /VOL 96/ 97

Figure 4.23 Distribution of temperature in the specimen after 200 hours heating 99

Figure 4.24 Distribution of water saturation in the specimen after 200 hours heating 99

Figure 4.25 Distribution of porosity in the specimen after 200 hours heating 99

Figure 4.26 Evolution of temperature during heating of bentonite 101

Figure 4.27 Evolution of pore water pressure during heating of bentonite 101

Figure 4.28 Evolution of lateral stress during heating of bentonite 102

Figure 4.29 Evolution of porosity during heating of bentonite 102

Figure 4.30 Scheme of the proposed large-scale ventilation test 105

Figure 4.31 Stress and porosity distribution in the hollow sample after loading 106

Figure 4.32 Evolution of porosity in the hollow sample 106

Figure 4.33 Evolution of the borehole convergence 107

Figure 4.34 Desaturation and resaturation of the hollow sample 107

Figure 4.35 General scheme of laboratory heating experiment on rock-buffer-sample 109

Figure 4.36 Model geometry and initial / boundary conditions 110

Figure 4.37 Distribution of temperature 111

Figure 4.38 Evolution of temperature at selected points 112

Figure 4.39 Distribution of water saturation 113

Figure 4.40 Evolution of water saturation at selected points 113

Figure 4.41 Evolution of pore water pressure at selected points 114

Figure 4.42 Evolution of pore gas pressure at selected points 115

Figure 4.43 Distribution of total stresses along the middle cross section 116

Figure 4.44 Evolution of total radial stress at selected points 117

Figure 4.45 Evolution of radial displacement of selected points 117

Figure 4.46 Model geometry, discretization, initial and boundary conditions of the rock mass surrounding a drift 119

Figure 4.47 Evolution of total stresses along x- and y- axis 121

Figure 4.48 Distributions of total stresses 6 years after excavation 122

Figure 4.49 Evolution of displacements along x- and y- axis..... 123

Figure 4.50 Distributions of displacements 6 years after excavation..... 123

Figure 4.51 Examination of the damaged zone surrounding the niche 124

Figure 4.52 Distribution of pore water pressure..... 126

Figure 4.53 Evolution of water saturation along x- and y- axis 127

8 List of Tables

Table 2.1a Characteristic data of samples from the Callovo-Oxfordian argillite at the MHM-URL Bure 12

Table 2.1b Characteristic data of samples from the Opalinus clay at the Mont Terri URL 13

Table 2.2 Overview of uniaxial creep tests conducted on the Callovo-Oxfordian argillite and the Opalinus clay 16

Table 4.1 Physical properties of some clays 79

Table 4.2 Constitutive parameters for some clays 80

Gesellschaft für Anlagen- und Reaktorsicherheit (GRS) mbH

Schwertnergasse 1
50667 Köln
Telefon +49 221 2068-0
Telefax +49 221 2068-888

Forschungsinstitute
85748 Garching b. München
Telefon +49 89 32004-0
Telefax +49 89 32004-300

Kurfürstendamm 200
10719 Berlin
Telefon +49 30 88589-0
Telefax +49 30 88589-111

Theodor-Heuss-Straße 4
38122 Braunschweig
Telefon +49 531 8012-0
Telefax +49 531 8012-200

www.grs.de

ISBN 3-931995-69-0